AFRL-AFOSR-VA-TR-2023

Effects of non-Kolmogorov turbulence and aerosols on long-range, optical propagation through the atmosphere

Muschinski, Andreas
NORTHWEST RESEARCH ASSOCIATES INC.
4118 148 AVE NE
REDMOND, WA, 98052
US

02/14/2023
Final Technical Report

Air Force Research Laboratory
Air Force Office of Scientific Research
Arlington, Virginia 22203
Air Force Materiel Command

REPORT DOCUMENTATION PAGE

PLEASE DO NOT RETURN YOUR FORM TO THE ABOVE ORGANIZATION.

1. REPORT DATE	2. REPORT TYPE	3. DATES COVERED	
20230214	Final	START DATE 20170930	END DATE 20220929

4. TITLE AND SUBTITLE
Effects of non-Kolmogorov turbulence and aerosols on long-range, optical propagation through the atmosphere

5a. CONTRACT NUMBER	5b. GRANT NUMBER	5c. PROGRAM ELEMENT NUMBER
FA9550-17-C-0021		61102F
5d. PROJECT NUMBER	**5e. TASK NUMBER**	**5f. WORK UNIT NUMBER**

6. AUTHOR(S)
Andreas Muschinski

7. PERFORMING ORGANIZATION NAME(S) AND ADDRESS(ES)
NORTHWEST RESEARCH ASSOCIATES INC.
4118 148 AVE NE
REDMOND, WA 98052
US

8. PERFORMING ORGANIZATION REPORT NUMBER

9. SPONSORING/MONITORING AGENCY NAME(S) AND ADDRESS(ES)	10. SPONSOR/MONITOR'S ACRONYM(S)	11. SPONSOR/MONITOR'S REPORT NUMBER(S)
Air Force Office of Scientific Research 875 N. Randolph St. Room 3112 Arlington, VA 22203	AFRL/AFOSR RTB1	AFRL-AFOSR-VA-TR-2023-0270

12. DISTRIBUTION/AVAILABILITY STATEMENT
A Distribution Unlimited: PB Public Release

13. SUPPLEMENTARY NOTES

14. ABSTRACT
Optical propagation through the turbulent atmosphere is characterized by turbulent fluctuations of the phase, the propagation direction, and the intensity of the optical wave, collectively referred to as “optical turbulence”. The modern physics of optical turbulence was pioneered in the 1950s and 1960s and it continues to serve as the scientific backbone for various technologies, such as optical remote sensing, free-space optical communication, optical imaging of terrestrial and extraterres-trial objects and adaptive optics, as well as target-acquisition, beam-control and directed-energy technologies. The objective of this project was to study various controversial aspects of optical tur-bulence by means of observations, theoretical analysis, and computer simulations. In several field experiments, we deployed digital cameras attached to portable telescopes, a frequency-comb laser system, ultrasonic anemometer-thermometers (“sonics”), and fine-wire thermometers. Our sonic and fine-wire measurements in the atmospheric surface layer corroborated the validity and use-fulness of the Monin-Obukhov similarity theory of surface-layer turbulence, the Obukhov-Corrsin similarity theory (“Kolmogorov turbulence”), and the Hill-Frehlich model of the “Hill bump” in the temperature spectrum of fully developed turbulence. While we have seen no evidence of “non-Kolmogorov turbulence” in the atmospheric surface layer, evidence of non-Gaussian temperature increments has been ubiquitous. To what extent non-Gaussianity of temperature increments trans-lates to non-Gaussianity of phase increments depends on the number of dominating large eddies along the propagation path. We have conducted computer simulations based on geometrical optics and wave optics in order to study the relative merits of the geometrical-optics method, the Rytov method, and the method of turbulent phase screens for the prediction of scintillation statistics and angle-of-arrival statistics for a wide variety of Rytov variances, ranging from weak scattering well into the strong-scattering regime.

15. SUBJECT TERMS

16. SECURITY CLASSIFICATION OF:			17. LIMITATION OF ABSTRACT	18. NUMBER OF PAGES
a. REPORT U	b. ABSTRACT U	c. THIS PAGE U	UU	67

19a. NAME OF RESPONSIBLE PERSON	19b. PHONE NUMBER *(Include area code)*
MICHAEL YAKES	00000000

Award Number: FA9550-17-C-0021

Report Type: Final

Reporting Period: October 1, 2017 through September 30, 2022

Distribution Statement: Distribution A – Approved For Public Release

Program Officer Name: Dr. Michael Yakes

Principal Investigator Name: Dr. Andreas Muschinski

Project Title: Effects of non-Kolmogorov turbulence and aerosols on long-range, optical propagation through the atmosphere

Abstract: Optical propagation through the turbulent atmosphere is characterized by turbulent fluctuations of the phase, the propagation direction, and the intensity of the optical wave, collectively referred to as ``optical turbulence''. The modern physics of optical turbulence was pioneered in the 1950s and 1960s and it continues to serve as the scientific backbone for various technologies, such as optical remote sensing, free-space optical communication, optical imaging of terrestrial and extraterrestrial objects and adaptive optics, as well as target-acquisition, beam-control and directed-energy technologies. The objective of this project was to study various controversial aspects of optical turbulence by means of observations, theoretical analysis, and computer simulations. In several field experiments, we deployed digital cameras attached to portable telescopes, a frequency-comb laser system, ultrasonic anemometer-thermometers (``sonics''), and fine-wire thermometers. Our sonic and fine-wire measurements in the atmospheric surface layer corroborated the validity and usefulness of the Monin-Obukhov similarity theory of surface-layer turbulence, the Obukhov-Corrsin similarity theory (``Kolmogorov turbulence''), and the Hill-Frehlich model of the ``Hill bump'' in the temperature spectrum of fully developed turbulence. While we have seen no evidence of ``non-Kolmogorov turbulence'' in the atmospheric surface layer, evidence of non-Gaussian temperature increments has been ubiquitous. To what extent non-Gaussianity of temperature increments translates to non-Gaussianity of phase increments depends on the number of dominating large eddies along the propagation path. We have conducted computer simulations based on geometrical optics and wave optics in order to study the relative merits of the geometrical-optics method, the Rytov method, and the method of turbulent phase screens for the prediction of scintillation statistics and angle-of-arrival statistics for a wide variety of Rytov variances, ranging from weak scattering well into the strong-scattering regime.

Section 1

Participants NWRA

Andreas Muschinski, Senior Research Scientist
60 months
Management of NRWA team and Principal Investigator

Eric Wagner, Senior Support Engineer
24 months
Design and field testing of fine-wire sensors

Charles Martin, Senior Research Engineer
12 months
Design and integration of data acquisition systems

Carter Mak, undergraduate engineering student
36 months
Field experiment and data analysis support

Nathan Kuczun, undergraduate engineering student
36 months
Field experiment and data analysis support

Ryan Schatzle, undergraduate physics student
24 months
Field experiment and data analysis support

Maxwell Anderson, undergraduate engineering student
24 months
Field experiment and data analysis support

Marcus Schaller, undergraduate physics student
12 months
Field experiment and data analysis support

Lisa Muschinski, undergraduate psychology student
12 months
Field experiment and graphics support

Peter Muschinski, high school student
12 months
Field experiment and data analysis support

Participants NMSU

David Voelz, Professor of Electrical Engineering
60 months
Management of NMSU team and lead for simulations

Erandi Wijerathna, postdoctoral researcher
54 months
Technical lead for simulations

David F. Tofsted, contractor
6 months
Turbulence theory and analysis

Andrea Baca, graduate student
4 months
Field experiment support

Other Partners or Collaborators NWRA

Gregory Rieker, Associate Professor of Mechanical Engineering
University of Colorado Boulder
Collaborator on field experiment

Emily Caldwell, graduate engineering student
University of Colorado Boulder
Field experiment and data analysis support

Laura Sinclair, Staff scientist
National Institute of Standards and Technology (NIST) Boulder
Collaborator on field experiment

William Swann, Staff scientist
National Institute of Standards and Technology (NIST) Boulder
Collaborator on field experiment

Other Partners or Collaborators NMSU

Robert Hull, Technical staff
New Mexico State University
Field experiment support

Hanyu Zhan, postdoctoral researcher
New Mexico State University
Collaborator on simulations

Jack McCrae
Air Force Institute of Technology (AFIT)
Turbulence theory and field experiment consultation

Steven Fiorino
Air Force Institute of Technology (AFIT)
Field experiment consultation

Journal Articles

Emily D. Caldwell, William C. Swann, Jennifer L. Ellis, Martha I. Bodine, Carter Mak, Nathan Kuczun, Nathan R. Newbury, Laura C. Sinclair, Andreas Muschinski, and Gregory B. Rieker. "Optical timing jitter due to atmospheric turbulence: comparison of frequency comb measurements to predictions from micrometeorological sensors." *Optics Express* 28, no. 18 (2020): 26661-26675. https://doi.org/10.1364/OE.400434

Andreas Muschinski. "Phase-factor spectra of turbulent phase screens." JOSA A 38, no. 9 (2021): 1339-1348. https://doi.org/10.1364/JOSAA.429928

Andreas Muschinski and Eric L. Wagner. "First field measurements of optical turbulence near the ground with a newly developed fine-wire thermometer." Waves in Complex and Random Media 33 (2023): in press, to appear as part of the Special Issue in honour of V. I. Tatarskii (1929-2020)

David G. Voelz, Erandi Wijerathna, Andreas Muschinski, Xifeng Xiao, "Computer simulations of optical turbulence in the weak- and strong-scattering regime: angle-of-arrival fluctuations obtained from ray optics and wave optics," Opt. Eng. 57(10) 104102 (5 October 2018) https://doi.org/10.1117/1.OE.57.10.104102

Erandi Wijerathna, Hanyu Zhan, David Voelz and Andreas Muschinski, "Low-wavenumber compensation with Zernike tilt for non-Kolmogorov turbulence phase screens," accepted for publication in Appl. Opt., December 2022. https://doi.org/10.1364/AO.475825

Hanyu Zhan, Erandi Wijerathna, and David Voelz, "Is the formulation of the Fried parameter accurate in the strong turbulent scattering regime?," OSA Continuum 3, 2653-2659 (2020) https://doi.org/10.1364/OSAC.404983

Hanyu Zhan and David G. Voelz, "Modeling solar eclipse shadow bands using wave optics simulation through distributed turbulence," Appl. Opt. 60, 8426-8434 (2021) https://doi.org/10.1364/AO.431996

Conference Proceedings

Emily D. Hannah, William C. Swann, Jennifer L. Ellis, Martha I. Bodine, Carter Mak, Nathan Kuczun, Nathan R. Newbury, Laura C. Sinclair, Andreas Muschinski, and Gregory B. Rieker. "Retrieval of the Refractive Index Structure Parameter from Frequency Comb Timing Jitter Data." In *Propagation Through and Characterization of Atmospheric and Oceanic Phenomena*, pp. PTu4F-5. Optical Society of America, 2020. https://doi.org/10.1364/PCAOP.2020.PTu4F.5

Emily D. Hannah, William C. Swann, Jennifer L. Ellis, Martha I. Bodine, Carter Mak, Nathan Kuczun, Nathan R. Newbury, Laura C. Sinclair, Andreas Muschinski, and Gregory B. Rieker. "Impact of Atmospheric Turbulence on Frequency Comb Optical Timing Jitter." In *Conference on Lasers and Electro-Optics (CLEO2020)*, pp. 1-2. IEEE, 2020.

Andreas Muschinski. "Non-Kolmogorov turbulence." In *Propagation Through and Characterization of Atmospheric and Oceanic Phenomena*, pp. PW2D-1. Optical Society of America, 2017. https://doi.org/10.1364/PCAOP.2017.PW2D.1

Andreas Muschinski. "Non-classical models of optical turbulence." Invited oral Presentation. In Unconventional Imaging and Adaptive Optics 2022, vol. 12239, p. 1223902. SPIE, 2022. https://doi.org/10.1117/12.2633193

Andreas Muschinski and Stephen M. de Bruyn Kops. "Phase Screens of Optical Turbulence Generated by Means of Direct Numerical Simulation of First Principles of Fluid Mechanics." In *Propagation Through and Characterization of Atmospheric and Oceanic Phenomena*, pp. PTu5F-4. Optica Publishing Group, 2018. https://doi.org/10.1364/PCAOP.2018.PTu5F.4

Andreas Muschinski and David G. Voelz, "Probability densities of atmospheric optical scintillation observed with large apertures," in Imaging and Applied Optics 2019 (COSI, IS, MATH, pcAOP), OSA Technical Digest (Optica Publishing Group, 2019), paper PTh3C.3. https://doi.org/10.1364/PCAOP.2019.PTh3C.3

David Voelz, Hanyu Zhan, and Erandi Wijerathna, "Wave and Ray Optics Simulations of Short Exposure Incoherent Imaging in Atmospheric Turbulence," in Imaging and Applied Optics 2018 (3D, AO, AIO, COSI, DH, IS, LACSEA, LS&C, MATH, pcAOP), OSA Technical Digest (Optica Publishing Group, 2018), paper PTu2I.2. https://doi.org/10.1364/PCAOP.2018.PTu2I.2

Erandi Wijerathna, David Voelz, and Hanyu Zhan, "Discrepancies between Simulation and Theory Results for Plane Wave Scintillation in Atmospheric Turbulence," in Imaging and Applied Optics 2018 (3D, AO, AIO, COSI, DH, IS, LACSEA, LS&C, MATH, pcAOP), OSA Technical Digest (Optica Publishing Group, 2018), paper PTu2I.4. https://doi.org/10.1364/PCAOP.2018.PTu2I.4

Hanyu Zhan and David Voelz, "Wave optics modeling of solar eclipse shadow bands," 2019 IEEE Aerospace Conference, 2019, pp. 1-6, doi: 10.1109/AERO.2019.8741706. DOI: 10.1109/AERO.2019.8741706

Erandi Wijerathna, David Voelz, Andreas Muschinski, and Hanyu Zhan, "Spherical Wave Scintillation in Atmospheric Turbulence: A Comparison of Analytical Models and Simulation Results," in Imaging and Applied Optics 2019 (COSI, IS, MATH, pcAOP), OSA Technical Digest (Optica Publishing Group, 2019), paper PM1C.4. https://doi.org/10.1364/PCAOP.2019.PM1C.4

Hanyu Zhan, Erandi Wijerathna, and David Voelz, "Wave Optics Simulation Studies of the Fried Parameter for Weak to Strong Atmospheric Turbulent Fluctuations," in Imaging and Applied Optics 2019 (COSI, IS, MATH, pcAOP), OSA Technical Digest (Optica Publishing Group, 2019), paper PM1C.3. https://doi.org/10.1364/PCAOP.2019.PM1C.3

Erandi Wijerathna, Hanyu Zhan, and David Voelz, "Spherical Wave Source Models and Simulation through von Karman Turbulence," in Optical Sensors and Sensing Congress, OSA Technical Digest (Optica Publishing Group, 2020), paper PM3D.3.

https://doi.org/10.1364/PCAOP.2020.PM3D.3

Hanyu Zhan, Erandi Wijerathna, David Voelz, and Andreas Muschinski, "Short-exposure image resolution: Tilt definition study," in OSA Imaging and Applied Optics Congress 2021 (3D, COSI, DH, ISA, pcAOP), H. Hua, B. Javidi, M. Martinez-Corral, O. Matoba, A. Stern, S. Thibault, T. Alieva, J. Ke, F. Willomitzer, F. Okten, P. Silveira, P. Banerjee, E. Stoykova, D. Chu, J. Park, F. Imai, C. Joo, M. Digman, D. Gardner, S. Gladysz, D. LeMaster, S. Basu, and O. Korotkova, eds., OSA Technical Digest (Optica Publishing Group, 2021), paper PTu4C.3.
https://doi.org/10.1364/PCAOP.2021.PTu4C.3

Other

Erandi A. Wijerathna, Numerical Wave Optics Simulations through Atmospheric Turbulence: Simulation Method Improvements and a Comparative Study of Optical Scintillation, PhD Dissertation, New Mexico State University, Elec. and Comp. Engr., ProQuest Dissertations Publishing, 2021. 28417316.

David Voelz, “Design techniques for wave optics simulation of propagation through atmospheric turbulence,” Invited Oral presentation, OSA Propagation Through and Characterization of Atmospheric and Oceanic Phenomena, 2021.

Section 2

Award number: FA9550-17-C-0021
Final Report
Performance Period: October 1, 2017 through September 30, 2022
Sponsor: AFOSR Physics of Sensing program (PO Dr. Michael K. Yakes)
Project Title: Effects of non-Kolmogorov turbulence and aerosols on long-range, optical propagation through the atmosphere
Authors: Andreas Muschinski and David Voelz
Awardee Organization: NorthWest Research Associates (NWRA), Boulder, CO
Date: January 13, 2023

Abstract:
Optical propagation through the turbulent atmosphere is characterized by turbulent fluctuations of the phase, the propagation direction, and the intensity of the optical wave, collectively referred to as "optical turbulence". The modern physics of optical turbulence was pioneered in the 1950s and 1960s and it continues to serve as the scientific backbone for various technologies, such as optical remote sensing, free-space optical communication, optical imaging of terrestrial and extraterrestrial objects and adaptive optics, as well as target-acquisition, beam-control and directed-energy technologies. The objective of this project was to study various controversial aspects of optical turbulence by means of observations, theoretical analysis, and computer simulations. In several field experiments, we deployed digital cameras attached to portable telescopes, a frequency-comb laser system, ultrasonic anemometer-thermometers ("sonics"), and fine-wire thermometers. Our sonic and fine-wire measurements in the atmospheric surface layer corroborated the validity and usefulness of the Monin-Obukhov similarity theory of surface-layer turbulence, the Obukhov-Corrsin similarity theory ("Kolmogorov turbulence"), and the Hill-Frehlich model of the "Hill bump" in the temperature spectrum of fully developed turbulence. While we have seen no evidence of "non-Kolmogorov turbulence" in the atmospheric surface layer, evidence of non-Gaussian temperature increments has been ubiquitous. To what extent non-Gaussianity of temperature increments translates to non-Gaussianity of phase increments depends on the number of dominating large eddies along the propagation path. We have conducted computer simulations based on geometrical optics and wave optics in order to study the relative merits of the geometrical-optics method, the Rytov method, and the method of turbulent phase screens for the prediction of scintillation statistics and angle-of-arrival statistics for a wide variety of Rytov variances, ranging from weak scattering well into the strong-scattering regime.

1 Background and objectives

The modern physics of wave propagation (radio-frequency, optical, and acoustic) through the turbulent atmosphere was pioneered by Tatarskii and coworkers in the 1950s and 1960s (Tatarskii, 1961, 1971). Tatarskii's main accomplishment was to integrate (1) methods to solve the scalar Helmholtz equation (Helmholtz, 1859) for electromagnetic and acoustic waves propagating through random media; (2) the theory of random fields and stochastic processes (Yaglom, 1952, 1962); and (3) the Obukhov-Corrsin theory of turbulent temperature fluctuations (Obukhov, 1949; Corrsin, 1951) into a unifying and versatile framework that enables one to derive relationships between various statistics of optical observables for a wide range of propagation scenarios. During the last 60 years, Tatarskii's methodology has been applied and expanded by several generations of scientists and engineers, as documented in a long list of monographs, textbooks, collections (Uscinski, 1977;

Ishimaru, 1978; Strohbehn, 1978; Uscinski, 1986; Andreas, 1990; Wheelon, 2001, 2003; Andrews and Phillips, 2005; Korotkova, 2014, 2022), and review articles (Strohbehn, 1968; Roddier, 1981; Beland, 1993).

While Tatarskii used mainly the geometrical-optics method (i.e., ray-tracing and eikonal-fluctuation theory) and perturbation theory (based on the Born approximation or the Rytov approximation) for solving the Helmholtz equation, Goodman's "Fourier optics" (Goodman, 1968, 2015, 2017, 2020) suggests a "systems engineering approach" to optical propagation and imaging through turbulent media. Conceptual centerpieces of Fourier optics are turbulent phase screens, linear, shift-invariant systems, and the Huygens-Fresnel principle in the form of the Fresnel diffraction integral. Goodman's approach has been widely used in imaging physics, adaptive optics, and computational optics (Roddier, 1999; Roggemann and Welsh, 1996; Sasiela, 2007; Schmidt, 2010; Voelz, 2011).

The objective of this project was to investigate the validity of various controversial assumptions and models of turbulence *pe se* and optical propagation through the turbulent atmosphere by means of field observations, theoretical analysis, and computer simulations.

2 Accomplishments

This section consists of two subsections, 2.1 ("Field observations and theoretical studies") and 2.2 ("Computer simulations"). For formatting reasons, subsection 2.2 is attached as a stand-alone document after the Bibliography of subsection 2.1.

2.1 Field observations and theoretical studies

2.1.1 Overview of field observations

We conducted several field experiments which employed high-resolution imaging systems and in-situ sensors. In addition to carrying out new field experiments from 2017 through 2022 (the project's performance period), we quality-controlled and re-processed field data that we had collected in earlier field campaigns (e.g., Cheon et al., 2007; Tichkule and Muschinski, 2012, 2014; Newman et al., 2016).

The field experiments conducted from 2017 though 2022 include the collection of image sequences involving long propagation paths between Hawaiian islands (Maui, July, 2019), across the Grand Canyon (South Rim, August, 2019), and across the southern part of White Sands Missile Range (White Sands, NM, Ocober, 2022), and involving a short propagation path (140 m) at the Table Mountain Test Facility (TMTF) between Boulder, CO and Lyons, CO (Caldwell et al., 2020). As in the previous experiments conducted at the now abandoned Boulder Atmospheric Observatory (Cheon et al., 2007; Tichkule and Muschinski, 2012, 2014; Newman et al., 2016), in the 2019 TMFT experiment we used ultrasonic anemometer-thermometers ("sonics") and quartz-crystal microbarometers as supporting in-situ sensors for measuring and retrieving mean values, mean vertical gradients, and turbulent fluctuations of the air temperature, air density, optical refractive index, and the three wind velocity components. Moreover, the 2019 TMFT employed, in addition to our imaging system, a unique frequency-comb laser system developed and operated by the National Institute of Standards and Technology (NIST) and the University of Colorado Boulder.

On February 1, 2019, we collected a total of 90,000 images of three stars (Polaris, Rigel, and Sirius), analyzed the speckle statistics (Muschinski and Voelz, 2019) and compared the observations with computer simulations; see Sections 2.1.3 and 2.2.7.

While the sonic and microbarometer measurements provide high-quality turbulence measurements at length and time scales down into the inertial subrange of atmospheric turbulence near the ground (i.e., down to tens of centimeters and hundreds of milliseconds), they are not capable of resolving the inner scale of turbulence, which in the atmospheric surface layer is typically on the order of 1 cm. While it has been known for many decades that inner-scale effects are important for the observation, modeling, and prediction of optical turbulence (Tatarskii, 1961), the question of how to correctly model the temperature spectrum in the transition range between the inertial-convective subrange and the viscous-diffusive subrange (Hill, 1978) has remained controversial (Muschinski and de Bruyn Kops, 2015; Muschinski, 2015). In order to enhance our observational capabilities, we have developed and field-tested a new fine-wire resistance thermometer system, which resolves air temperature fluctuations down to 1 mK at length scales of down to 1 mm and at a time scales down to less than 1 ms (Muschinski and Wagner, 2023).

During the first week of October, 2022, we conducted a long-range optical propagation experiment (path length 84 km) across White Sands Missile Range near Las Cruces, NM.

2.1.2 Temperature and refractive-index spectra retrieved from ultrasonic thermometer measurements

An example of optical-turbulence measurements collected at one of our field sites is described in the following.

Fig. 1 shows time series of air temperature and wind speed observed during the 24-h period from 0000 UTC through 2400 UTC on 21 Sep 2018. The data were collected with an ultrasonic anemometer-thermometer ("sonic") mounted 4 m above ground level on a portable 20-ft tower located in complex terrain in the foothills of the Rocky Mountains ca. 5 km west of Boulder, CO at an elevation of 2000 m MSL. The sonic's sampling rate was 32 samples per second.

Sep 21, 2018 was a typical Colorado late summer day, with radiative cooling during the night (the minimum temperature was 6.5 deg C) and a convective boundary layer at daytime, with a temperature maximum of 23.1 deg C in the early afternoon (around 2100 UTC or 1400 MST). The mean wind speed was about 1 $\mathrm{m\,s^{-1}}$ during the first half of the night and at daytime, and less than 1 $\mathrm{m\,s^{-1}}$ during the second half of the night. The instantaneous wind speed reached values of up to about 5 $\mathrm{m\,s^{-1}}$. The pressure during this 24-h period varied between 797.7 hPa and 808.5 hPa.

Fig. 2 shows two time series of the optical refractive index, calculated for the optical wavelengths λ = 480 nm (blue light) and λ = 700 nm (red light). The refractive-index time series were calculated from the temperature measurements shown in Fig. 1 and from collocated pressure measurements by means of the relationship

$$n = 1 + a\left(1 + \frac{b}{\lambda^2}\right)\frac{p}{T}, \tag{1}$$

(Clifford, 1978, p. 10, eq. 2.1), where n is the optical refractive index, p is the pressure, T is the absolute temperature, and $a = 7.76\,\mathrm{K\,Pa^{-1}}$ and $b = 7.52 \times 10^{-15}\,\mathrm{m^2}$ are constants. In contrast to the radio-frequency refractive index (e.g., Bean and Dutton, 1966), which is independent of the electromagnetic wavelength but depends sensitively on the humidity, the optical refractive index is a function of the wavelength (dispersion) but varies only very slightly with humidity.

During the 24-h period, n varied between 1.000217 and 1.000231 for blue light (λ = 480 nm) and between 1.000214 and 1.000227 for red light (λ = 700 nm).

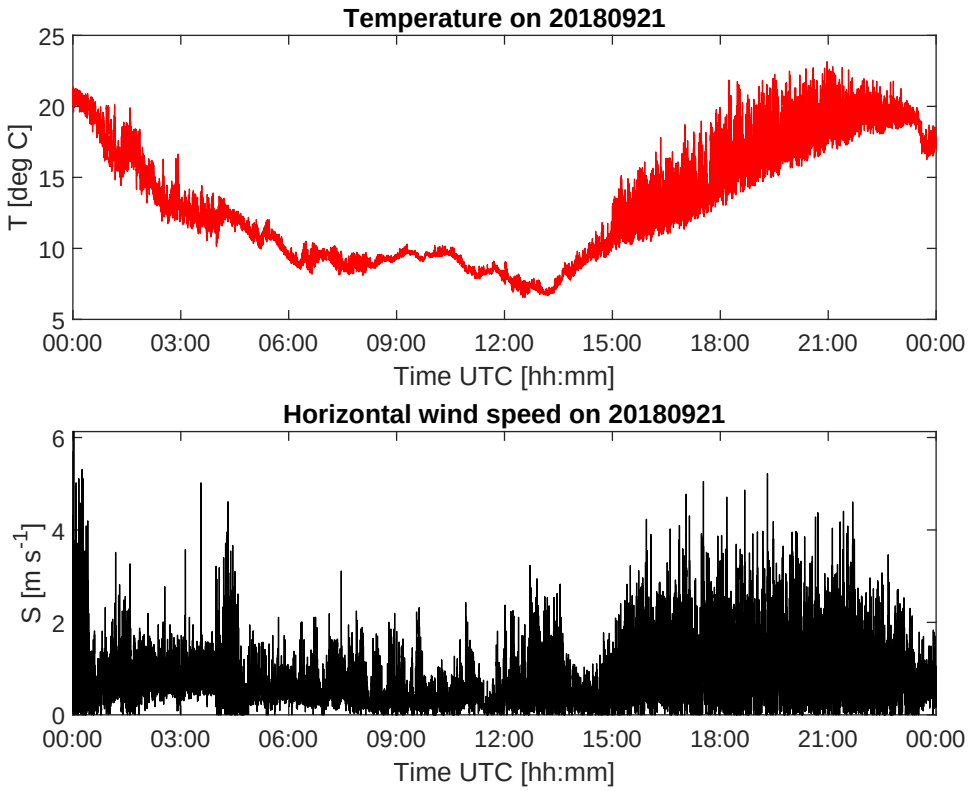

Figure 1: *Time series of air temperature and of wind speed observed with an ultrasonic anemometer-thermometer mounted 4 m above ground level on a portable 20-ft tower. The data were collected on 21 Sep, 2018 in complex terrain in the foothills of the Rocky Mountains ca. 5 km west of Boulder, CO at an elevation of 2000 m MSL.*

Fig. 3 shows the frequency spectrum of the refractive-index fluctuations calculated for blue light ($\lambda = 480$ nm) from the temperature and pressure values observed during the 1-h long mid-morning period beginning at 1600 UTC (0900 MST). We calculated the spectrum in two steps. First, we estimated an averaged modified periodogram (Welch, 1967) by averaging nine modified periodograms, each of length 12 min (1/5 h) and windowed with a Blackman window. We chose the overlapping of subsequent windows to be 50%. In a second step, we applied frequency-domain averaging to the Welch-averaged spectrum, where the width of the frequency bins was constant on a logarithmic scale, such that the three frequency decades below the Nyquist frequency (16 Hz) each contained 20 frequency bins. This procedure reduced the uncertainty of the individual spectral estimates to the extent that the $f^{-5/3}$ asymptote could be clearly identified and clearly distinguished from the $f^{-8/3}$ asymptote.

The observed spectrum shown in Fig. 3 follows closely the classical $f^{-5/3}$ power law in the frequency range from 0.1 Hz to 3 Hz and follows a $f^{-8/3}$ power law between about 3 Hz and 10 Hz. The $f^{-8/3}$ law is a result of spatial filtering due to the finite size of the the sonic. The mean value of the 3D instantaneous wind speed during the 1-h period was $S = 1.20\ \mathrm{m\,s^{-1}}$, and the magnitude of the mean 3D wind vector was $U = 0.97\ \mathrm{m\,s^{-1}}$. The onset of spatial filtering occurs at $f = 3$ Hz, which corresponds to a streamwise wave number of $\kappa = 2\pi f/U$ and to an eddy diameter of $D = \pi/\kappa$ (Heisenberg, 1948, p. 635), which for $f = 3$ Hz gives $D = U/2f = 17$ cm, which is close to the diameter of the sonic's sampling volume. This result is consistent with the assumption (given a

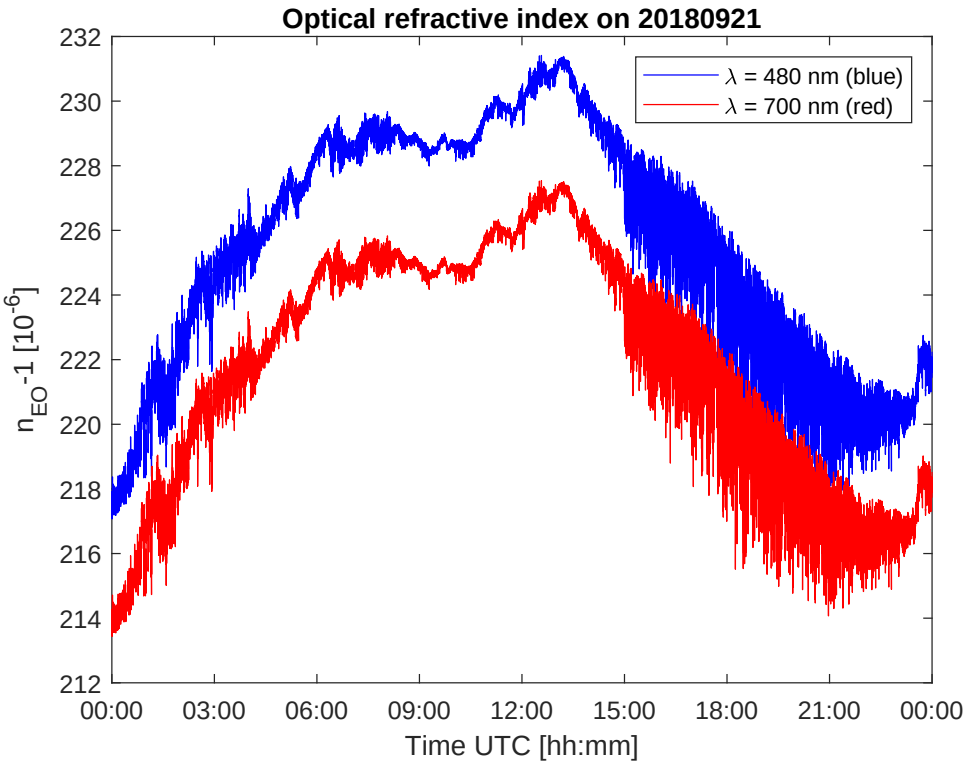

Figure 2: *Time series of the optical refractive index calculated from the temperature measurements shown in Fig. 1 and from collocated pressure measurements. The refractive index was calculated for two different optical wavelengths, $\lambda = 480$ nm and $\lambda = 700$ nm.*

mean wind speed of 1 $\mathrm{m\,s^{-1}}$) that for frequencies small compared to 3 Hz, the sonic's finite size is negligible and the sonic may be treated like a point sensor. Obviously, it is important to account for this spatial filtering effect when extracting estimates of the refractive-index structure parameter, C_n^2, or other structure parameters from sonic measurements.

From the $f^{-5/3}$ asymptote, C_n^2 can be retrieved by means of the relationship

$$C_n^2 = 13.67\, S_{nn}(f) f^{5/3} U^{-2/3} \tag{2}$$

(Muschinski et al., 2001, p. 235, eq. 10), which for the observed spectrum in Fig. 3 gives $C_n^2 = 9 \times 10^{-15}\,\mathrm{m}^{-2/3}$.

2.1.3 Stellar scintillation

In the evening of February 1, 2019, we conducted a field experiment in the foothills of the Rocky Mountains at an elevation of 2000 m MSL, ca. 5 miles west of Boulder, CO. The goal of the experiment was to collect an empirical database of stellar scintillation. The observations were performed under unusually clear skies in a moonless evening, and there was almost no wind at ground level.

We used a 14-inch, Schmidt-Cassegrain telescope equipped with a digital camera. The camera collected image sequences of, respectively, Polaris, Rigel, and Sirius. The frame rate was 60 frames per second, the bit depth was 12 bits (i.e., photon counts ranged from 0 to 4095), and the exposure

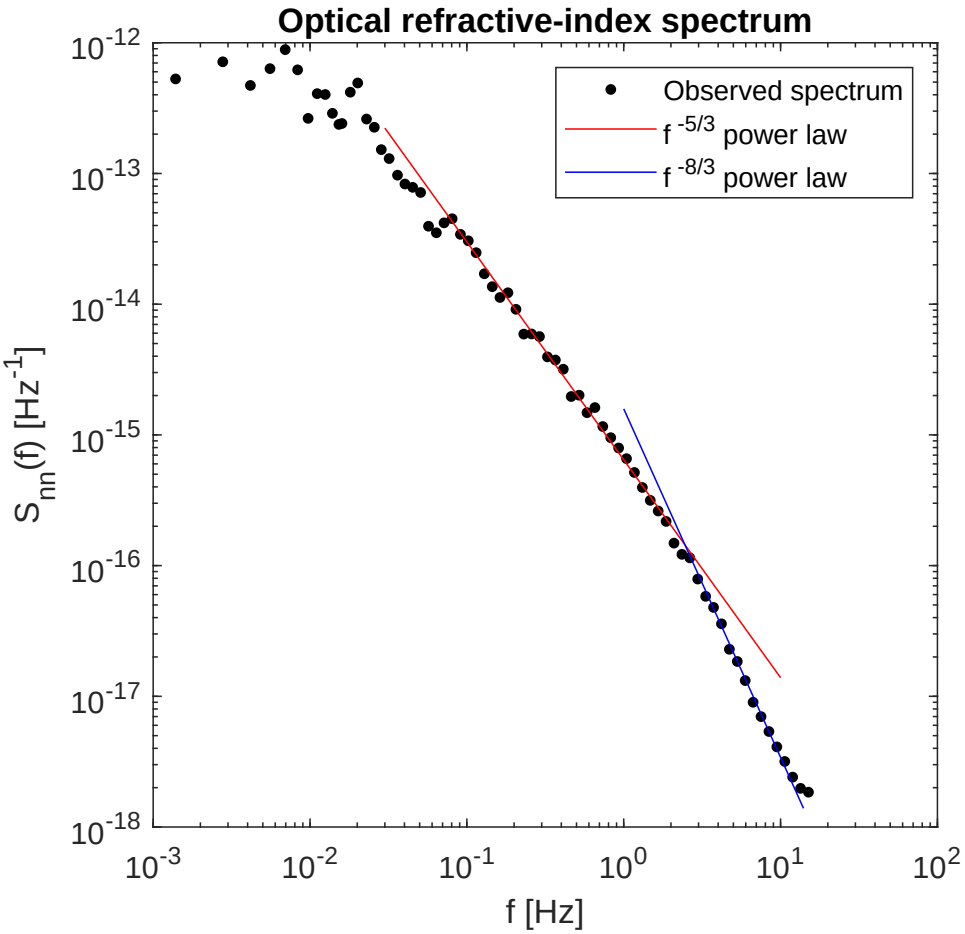

Figure 3: *Frequency spectrum of the refractive-index fluctuations for the 1-h period from 1600 UTC through 1700 UTC.*

time was a few milliseconds. We collected 54,000 frames of Polaris (observation period 15 min, exposure time 4.93 ms), 18,000 frames of Rigel (observation period 5 min, exposure time 6.03 ms), and 18,000 frames of Sirius (observation period 5 min, exposure time 2.19 ms). The telescope was in focus during the observations of Polaris, and it was deliberately set slightly out of focus (in order to study effects of a non-zero displacement between focal plane and observation plane) for the observations of Rigel and Sirius.

Fig. 4 shows a 100 × 100 pixel section of image #14,001 of the 18,000 images of Rigel. (The full images contain 640 × 480 pixels.) The physical size of a pixel on the photo sensor is $d = 7.5$ μm. That is, the image shown in Fig. 4 was captured within a square of side length 0.75 mm in the observation plane. Given a focal length of $F = 3.6$ m, the pixel size of $d = 7.5$ μm translates into an angular resolution of $d/F = 2.08$ μrad per pixel. As can be seen in Fig. 4, the size of the speckles in the observation plane was about 10 pixels.

Fig. 5 shows photon-count profiles of rows #20, 40, 60, and 80 of the image shown in Fig. 4. The width of the maxima and minima of the photon-count profiles is of order 10 pixels, consistent with the speckle size estimated from Fig. 4.

A speckle size D_s in the pupil plane means that the effective aperture size is D_s, such that the

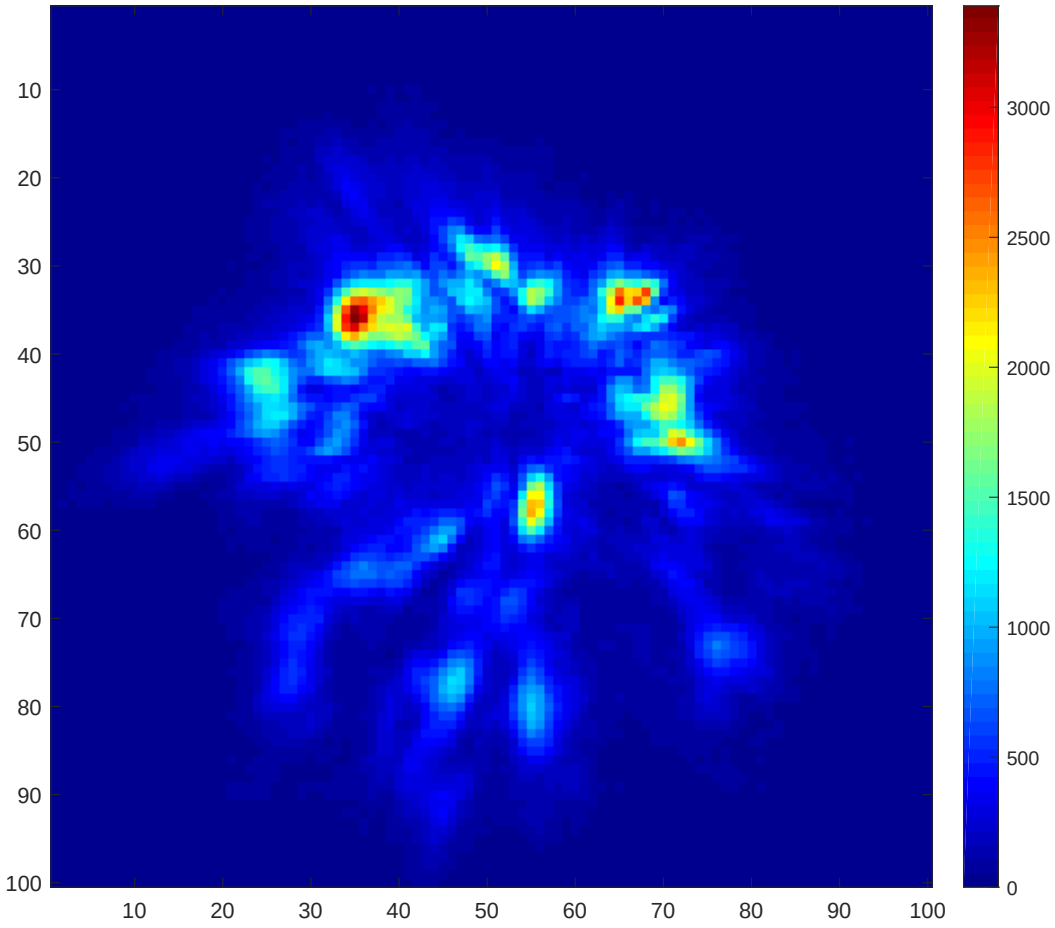

Figure 4: *Image #14,001 of a sequence of 18,000 images of Rigel collected in the evening of February 1, 2019 in the foothills of the Rocky Mountains ca. 5 miles west of Boulder, CO.*

angular resolution (the diameter of the "seeing disk") is 2.44 λ/D_s instead of the diffraction-limited angular resolution 2.44 λ/D (where D is the aperture diameter). Equating 2.44 λ/D_s with 20 μrad (corresponding to 10 pixels) gives an order-of-magnitude estimate of $D_s = 6$ cm, that is, about 1/6 of the aperture diameter of 36 cm. Therefore, there are of order $(D/D_s)^2 = 36$ independent "seeing cells" across the aperture.

Fig. 6 shows one-dimensional, horizontal and vertical wave-number spectra estimated from sequences of 3000 individual images of Polaris, Rigel, and Sirius, respectively. Prior to the spectral analysis, the images were cropped to a size of 480 $\times$ 480 pixels, resulting into a non-dimensional Nyquist wave number of $k = 240$. All six spectra are essentially flat at low wave numbers. The vertical and horizontal spectra of both Rigel and Sirius follow approximately a $k^{-8/3}$ power law for intermediate wave numbers (approximately $15 < k < 100$), and the vertical spectra of both Rigel and Sirus follow very precisely a $k^{-14/3}$ power law at higher wave numbers. In contrast to the vertical spectra, all three horizontal spectra (Polaris, Rigel, and Sirius) flatten out at high wave

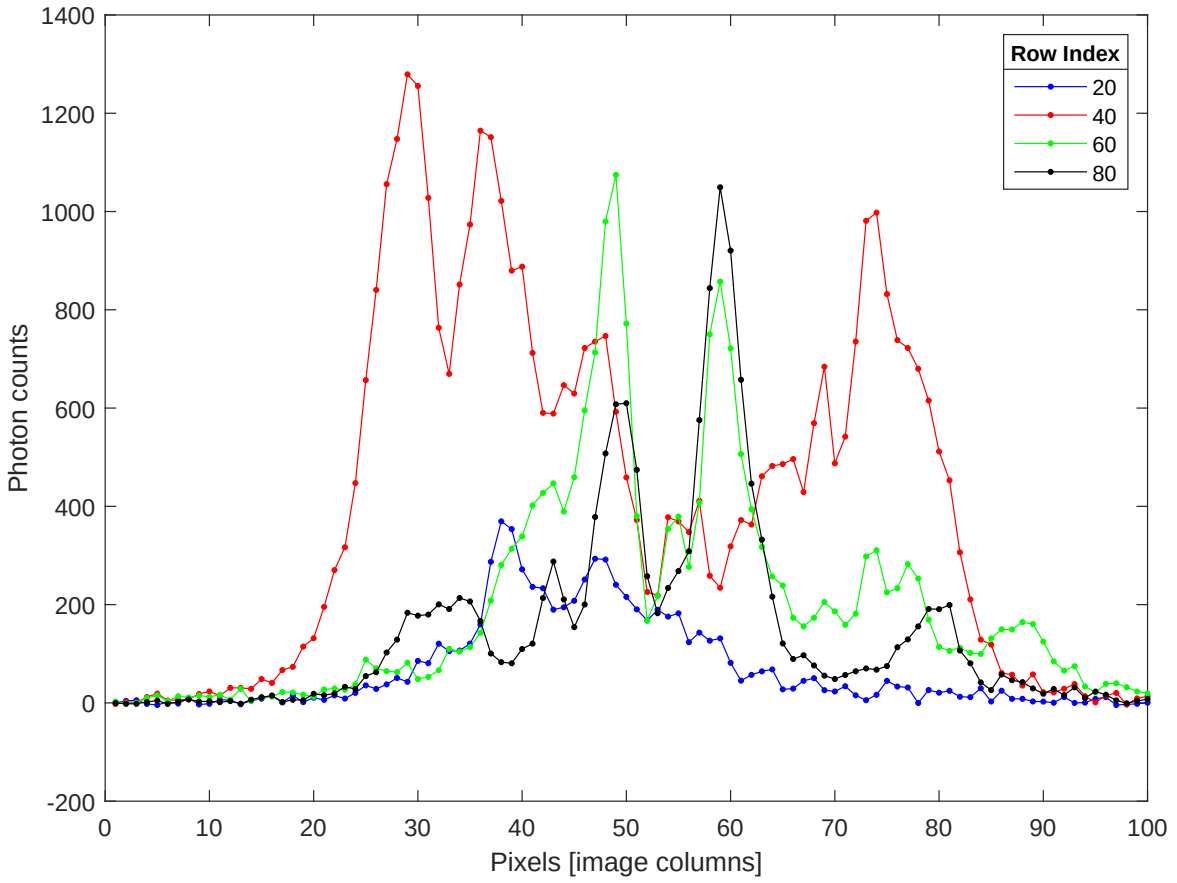

Figure 5: *Four horizontal photon-count profiles extracted from the image shown in Fig. 4.*

numbers. The spikes that appear in all six spectra at the same regularly spaced wave numbers in the high-wave number range are probably artifacts caused by some spatial periodicity in the photo sensor's gain and/or bias.

Fig. 7 shows histograms of the intensities (i.e., photon counts) of Polaris, Rigel, and Sirius observed with small subsets of the entire $640 \times 480 = 307{,}200$ photo sites ("pixels") of the camera. For photon counts per pixel exceeding about 200, all three histograms are consistent with a negatively exponential probability density, as predicted under the assumption that the complex optical amplitude in the image plane is a circular Gaussian process (Roddier, 1981, section 5.3 on pp. 318f.):

$$p_I(I) = \frac{1}{\langle I \rangle} \exp\left(-\frac{I}{\langle I \rangle}\right) \tag{3}$$

for $I \geq 0$ and $p_I(I) = 0$ for $I < 0$.

It is important to clearly distinguish between scintillation in the pupil plane (where the starlight enters the telescope) and scintillation in the observation plane. The observation plane coincides with the focal plane if the telescope is in focus, and it is displaced from the focal plane if the telescope is out of focus. A scintillation index of 1 (consistent with a circularly Gaussian process) in the

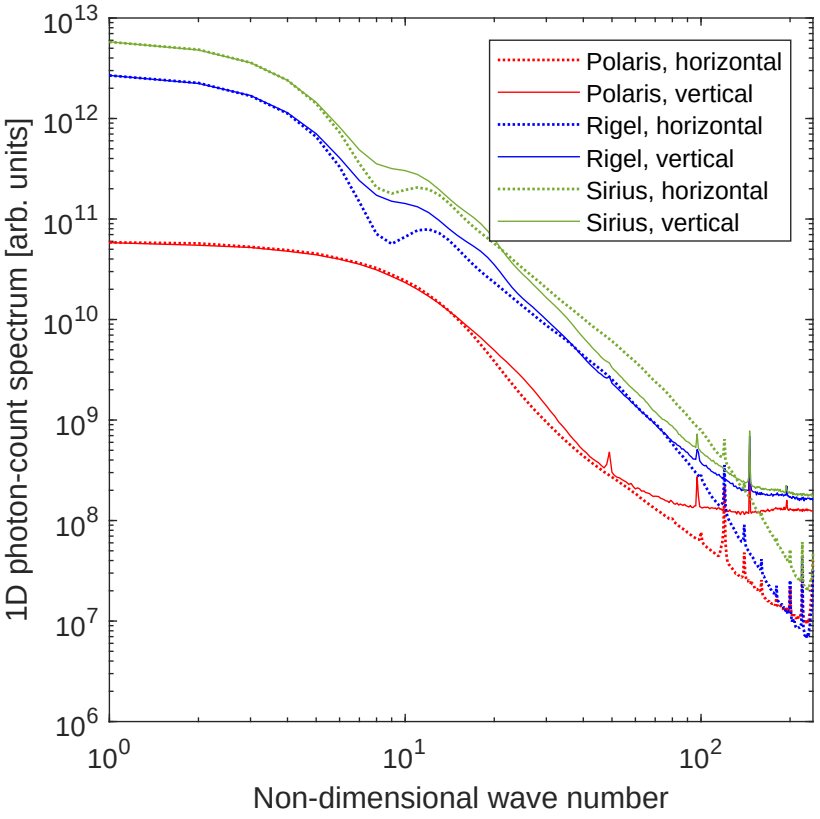

Figure 6: *One-dimensional, spatial photon-count spectra estimated from 3 individual images of Polaris, Rigel, and Sirius. The images were collected in the evening of February 1, 2019 in the foothills of the Rocky Mountains ca. 5 miles west of Boulder, CO.*

observation plane does not necessarily imply that the scintillation index that would be observed with a point detector in the pupil plane would also be 1.

Now, we consider the scintillation index σ_a^2 of the total irradiance entering the aperture ("photons in a bucket"). The law of large numbers predicts that σ_a^2 is of order $1/N$, where N is the number of "seeing cells" within the aperture. Because the seeing cell size is on the order of Fried's phase coherence length, r_0, this gives

$$\sigma_a^2 \propto \left(\frac{r_0}{D}\right)^2. \tag{4}$$

It is known that r_0 is proportional to $(\cos\vartheta)^{3/5}$, where ϑ is the star's zenith angle, assuming that the vertical integral of C_n^2 is horizontally homogeneous across the volume that contains the lines-of-sight to the different stars being observed. Therefore, in the case of horizontal homogeneity of C_n^2 we expect

$$\sigma_a^2 \propto (\cos\vartheta)^{6/5}, \tag{5}$$

which implies that both r_0 and σ_a^2 decrease with increasing zenith angle.

Fig. 8 shows the observed time series of σ_a^2 for Polaris, Rigel, and Sirius. We observed $\sigma_a^2 = 0.0096$ for Polaris and Rigel, and $\sigma_a^2 = 0.021$ for Sirius, such that $r_0 \sim D/10$ for Polaris and Rigel, and

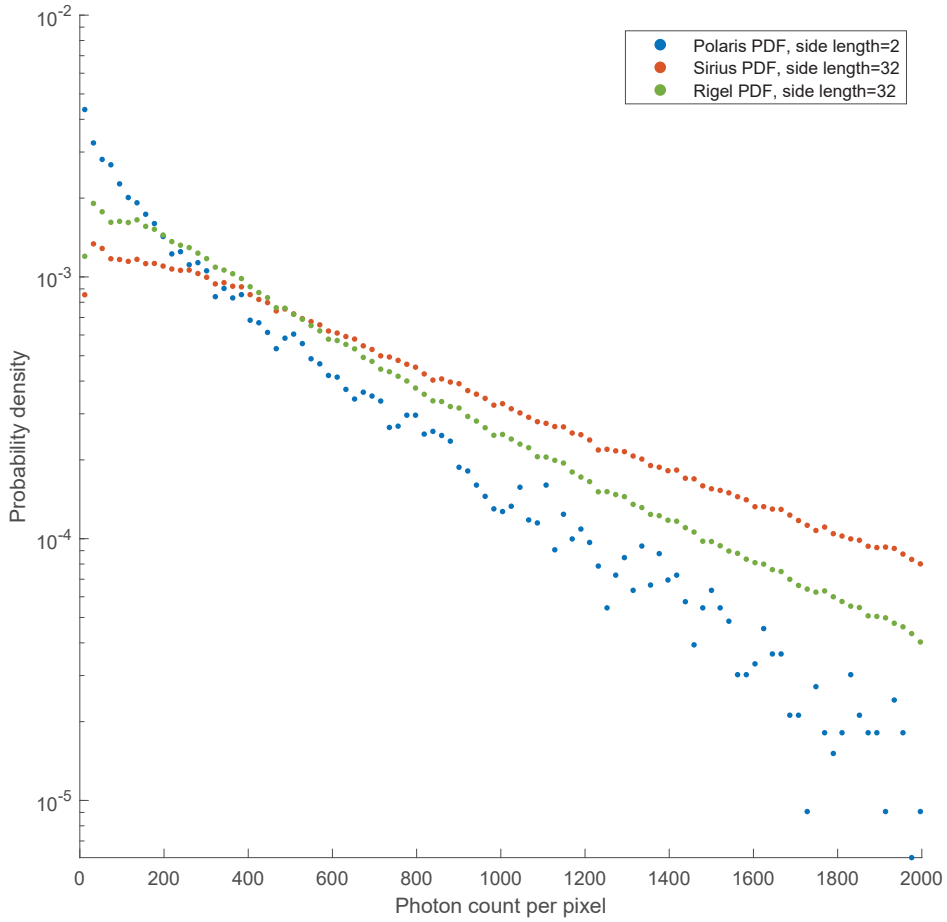

Figure 7: *Histograms of single-pixel photon counts extracted from image sequences of Polaris, Rigel, and Sirius. The measurements were collected in the evening of February 1, 2019 in the foothills of the Rocky Mountains ca. 5 miles west of Boulder, CO.*

$r_0 \sim D/7$ for Sirius. For $D = 36$ cm, this gives $r_0 \sim 3.6\,\mathrm{cm}$ for Polaris and Rigel, and $r_0 \sim 5.1\,\mathrm{cm}$ for Sirius. Polaris was at $\theta = 50^\mathrm{o}$ because Boulder, CO is at 40 degrees latitude. At the time of the observation, Rigel's zenith angle was very close to Polaris's, which is consistent with our observation that σ_a^2 was approximately the same for Polaris and Rigel. The zenith angle of Sirius, however, was significantly larger, which implies that r_0 for Sirius was smaller than r_0 for Polaris and Rigel. This is contrary to our observations. While the retrieved order of magnitude of r_0 (several centimeters) is in agreement with the pupil-plane speckle size retrieved from the out-of-focus images (see above), it is unclear why our observed σ_a^2 for Sirius was larger (not smaller) than that for Rigel and Polaris. One possible explanation is that at low elevation angles (large zenith angles), one or more of the underlying assumptions for estimating the Fried length (paraxial approximation, geometrical optics, monochromaticity, negligibility of optical dispersion, horizontal homogeneity of C_n^2, negligibility of "non-Kolmogorov turbulence", absence of high clouds, negligibility of temporal blurring) may be invalid.

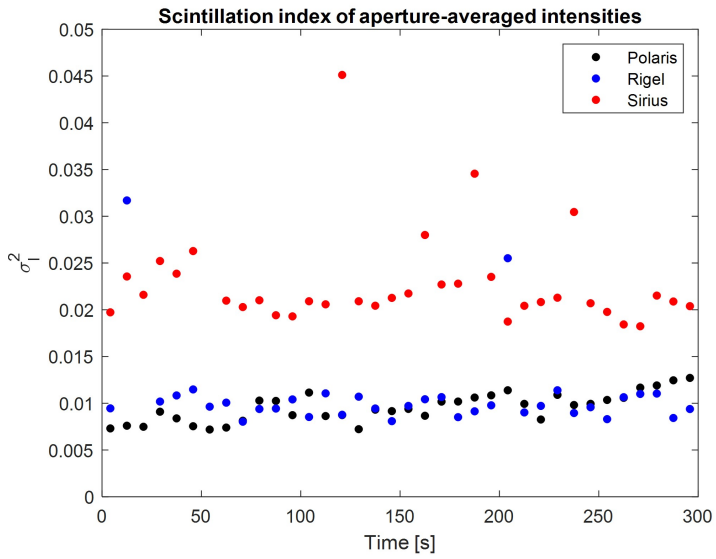

Figure 8: *Time series of 5-s estimates of the scintillation indices of the aperture-integrated irradiances ("photons in a bucket") of Polaris, Rigel, and Sirius. The images were collected in the evening of February 1, 2019 in the foothills of the Rocky Mountains ca. 5 miles west of Boulder, CO. The scintillation indices were retrieved from 18,000 individual images of each of the three stars.*

2.1.4 The June 2019 Table Mountain Experiment

From May 30 through June 7, 2019, we conducted, in collaboration with researchers from the National Institute of Standards and Technology (NIST) and the University of Colorado (CU) Boulder, a field experiment at the Table Mountain Test Facility located several miles north of Boulder, CO. The NWRA team deployed two measurement systems: first, a portable 20-ft tower instrumented with four ultrasonic anemometer-thermometers ("sonics") and one quartz-crystal barometer; second, an optical imaging system consisting of a 14-inch Meade telescope equipped with a digital camera streaming images into a laptop PC, and a checkerboard target 140 m away. NIST/CU provided a one-of-a-kind frequency-comb laser system, which is capable of measuring absolute time-of-flight with femto-second precision. We operated the two optical systems along two 140-m paths propagation path laterally spaced by about 0.5 m. That is, we interrogated practically the same optical path. The meteorological tower was deployed within about 1 m of the propagation paths.

In Caldwell et al. (2020), we show that the refractive-index structure parameter, C_n^2, retrieved from the sonic and barometer measurements agrees well with C_n^2 retrieved from the absolute phase measurements collected with the frequency-comb laser system.

In the remainder of this subsection, we present results of our analysis of 47 full days of sonic turbulence measurements on the basis of the Monin-Obukhov similarity theory.

Fig. 9 shows time series of 1-min estimates of three micrometeorological observables: the air temperature T (upper panel); the kinematic heat flux, $Q = \langle w'T' \rangle$, where w is the vertical wind velocity and a prime stands for "fluctuation of" (middle panel); and the temperature structure parameter, C_T^2 (bottom panel). The time series shown in Fig. 9 cover the 48-h period beginning at 1800

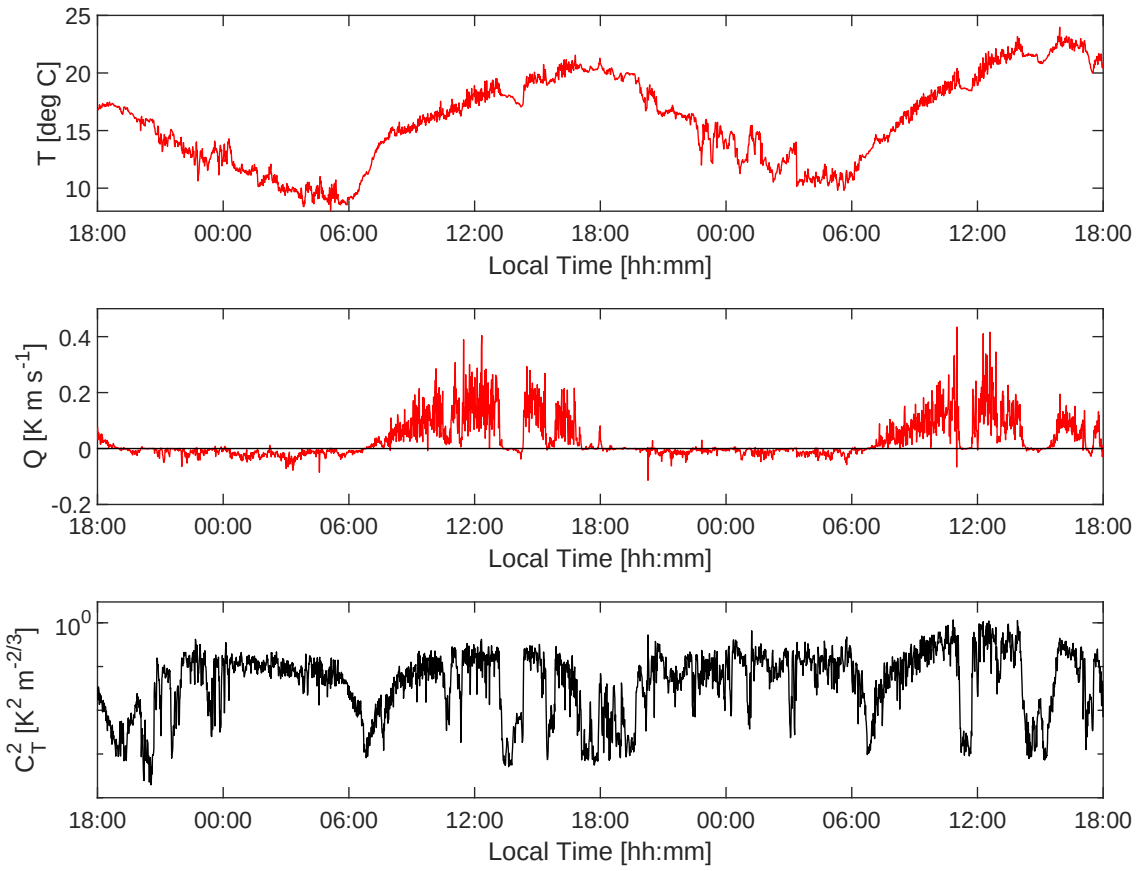

Figure 9: *Time series of (a) temperature T, (b) kinematic heat flux Q, and (c) temperature structure parameter C_T^2 observed at 3.31 m AGL during the 48-h period beginning at 1800 LT on 31 May 2019.*

Local Time (LT) on 31 May 2019 and are estimates from a raw dataset taken with an ultrasonic anemometer-thermometer ("sonic") mounted at 3.31 m above ground level (AGL). (Three more sonics were mounted on the same tower at different heights but those observations are not shown here.)

The data shown in Fig. 9 illustrate the typical behavior of the atmospheric surface layer (ASL) above prairie grass in Colorado in late spring: increasing temperature at daytime (between about 0600 LT and 1800 LT) and nocturnal cooling between about 1800 LT and 0600 LT; a positive (upward) heat flux at daytime and a negative (downward) heat flux at night; and C_T^2 varying between about $1 \times 10^{-3}\,\mathrm{K^2 m^{-2/3}}$ and $1\,\mathrm{K^2 m^{-2/3}}$, reaching maxima at daytime and minima during the morning and evening transitions characterized by sign reversals of Q.

Closer inspection reveals that in the mornings of 31 May and of 1 June, Q reversed its sign and C_T^2 reached its minimum at about the same time, typically 0645 LT, about 70 min after sunrise, at 0535 LT. The coincidence of a Q reversal and the occurrence of a C_T^2 minimum, which is predicted by the Monin-Obukhov theory of optical turbulence (Wyngaard et al., 1971), was observed throughout June and July, 2019. The evening transitions were less well defined than the morning transitions, which is a consequence of the less well defined sunset (because of the irregular ridgeline of the Rocky Mountains in the west) and the prevalence of afternoon thunderstorms.

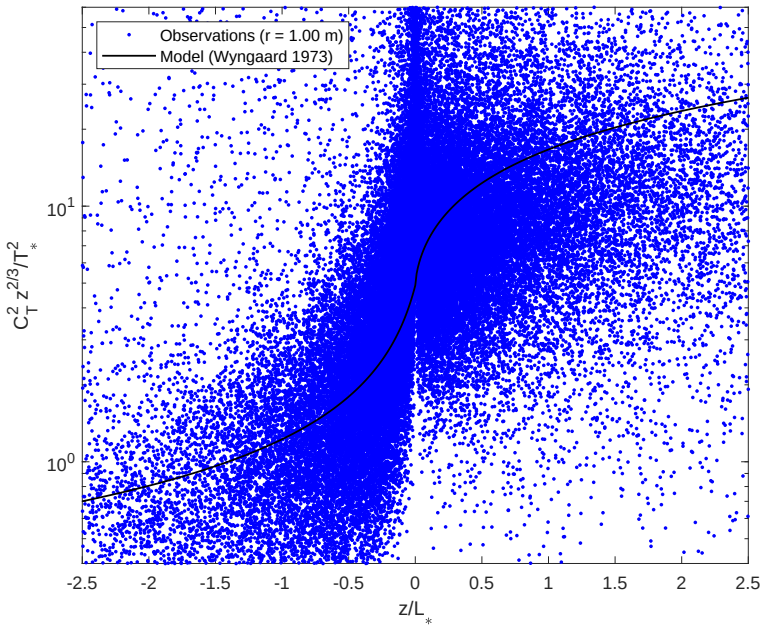

Figure 10: *Correlogram of 1-min estimates of C_T^2 versus 1-min estimates of z/L_*. Observations from 47 full-day (i.e., 24-h periods) are shown.*

Fig. 10 is a correlogram of 1-min estimates of the non-dimensionalized temperature structure parameter, $f_T = C_T^2 z^{2/3}/T_*^2$, versus the corresponding 1-min estimates of the stability parameter, z/L_* (blue dots). Data from 47 full days (i.e., 24-h periods) are aggregated in Fig. 10. The solid black line is the $f_T(z/L_*)$ model obtained by Wyngaard (1973, p. 128) based on the data collected in the 1968 Kansas Experiment (Businger et al., 1971). Obviously, the 1-min estimates of f_T scatter widely about the Wyngaard model, a phenomenon that is well known but not accounted for in the traditional Monin-Obukhov theory. (The Monin-Obukhov theory predicts only the mean value of f_T as function of z/L_* but not the variability of f_T.) Fig. 11 shows the conditional averages, $\langle f_T(z/L_*)|z/L_*\rangle$, of the data shown in Fig. 10, along with four model functions for $f_T(z/L_*)$. While our conditional averages seem to indicate a constant value around 10 in the stable regime (z/L_*), the deterministic models predict an increase of f_T with increasing z/L_*.

Fig. 12 is a histogram of f_T observed in the z/L_* interval $0.5 < z/L_* < 1.0$. Of course, this plot makes sense only if one treats f_T as a random function of z/L_*, as opposed to a deterministic function of z/L_*. This randomness is a defining characteristic of intermittent turbulence; see, e.g., Muschinski et al. (2004). As mentioned above, the traditional Monin-Obukhov theory makes no prediction regarding the variability of f_T for a given z/L_*. Fig. 12, however, seems to indicate that there is some interesting physics in the histogram of f_T: the probability density of f_T increases linearly with f_T for $f_T \ll 10$, and it decreases like f_T^{-4} for $f_T \gg 10$.

Once a model for the conditional probability density of f_T is established, such a model might open the path for predictions of the variability of other optical-turbulence characteristics, such as the Fried length and the scintillation index.

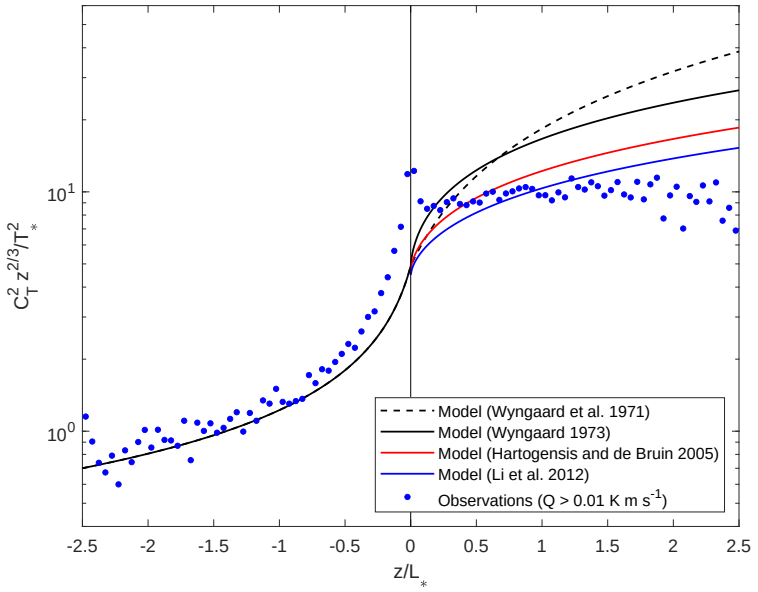

Figure 11: *Conditional averages* $\langle f_T(z/L_*)|z/L_*\rangle$ *of the 1-min estimates shown in Fig. 10.*

2.1.5 Non-Gaussianity of turbulent temperature increments

A widely used assumption in computational studies of optical wave propagation through the turbulent atmosphere is the assumption that phase screens, including spatial increments across phase screens, are Gaussian-distributed (e.g., Roddier, 1981; Martin and Flatté, 1988; Schmidt, 2010; Voelz et al., 2018). This assumption is usually justified on the basis of the central limit theorem, which states that the sum of a sufficiently large number of independent, identically distributed ("iid") random variables (R.V.'s) is approximately Gaussian distributed, regardless of the probability distribution of the indidual R.V.'s. This justification is questionable if "sufficiently large" is not quantified.

Optical phase fluctuations are proportional to the integral of the instantaneous temperature fluctuations along the propagation path. Spatial phase-screen increments are therefore proportional to the difference between two integrals along laterally spaced propagation paths. In other words, a spatial phase-screen increment is essentially an integral, along the propagation path, over path-transverse, spatial temperature increments. If the *local* (e.g., not path-integrated), transverse temperature increments are Gaussian-distributed, then also the line integral over these transverse temperature increments is Gaussian-distributed. If, however, the probability density of local temperature increments is strongly non-Gaussian, then it is not immediately clear to what extent the path integral over these temperature increments (and therefore the phase-screen increments) may be approximated as a Gaussian R.V.

Fig. 13 shows two histograms of instantaneous, vertical temperature increments, $\Delta T_{12} \equiv T(z_2) - T(z_1)$ and $\Delta T_{23} \equiv T(z_3) - T(z_2)$, observed during the 1-h long period beginning at 1700 UTC on 8 June, 2019. Here $T(z_1)$, $T(z_2)$ and $T(z_3)$ are the temperatures measured at the heights above ground level (AGL) $z_1 = 1.58$ m, $z_2 = 2.28$ m and $z_3 = 3.31$ m, respectively. Fig. 13 shows that the temperature increments ΔT_{12} and ΔT_{23} are not Gaussian-distributed. In the following, we suggest an asymmetric, two-sided, exponential probability density function as an alternative model.

Second-order statistics such as variances, covariances, and structure parameters of turbulent fluc-

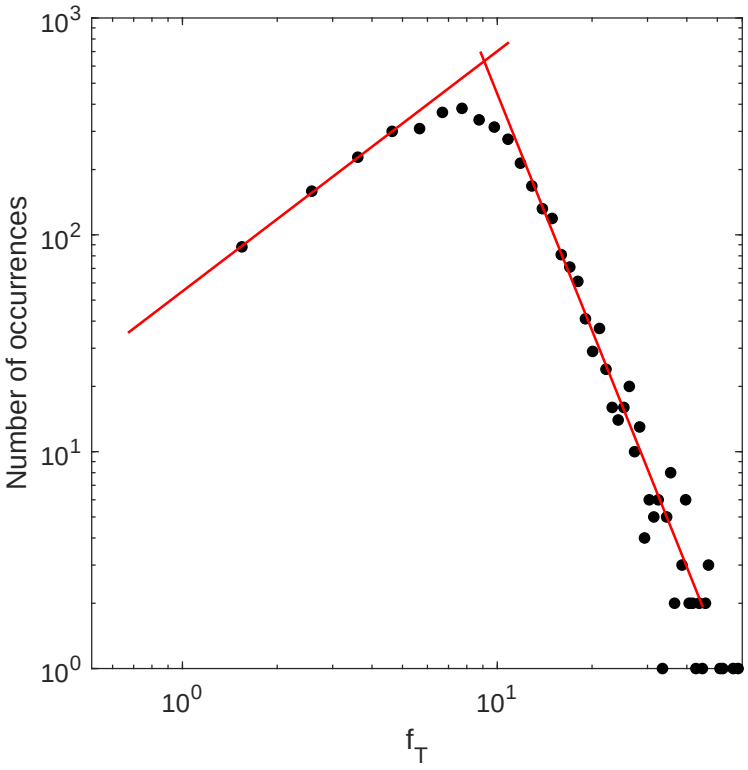

Figure 12: *Histogram of 1-min estimates of f_T within the z/L_* interval [0.5, 1.0]. The histogram was computed from 47 days of data shown in Fig. 10.*

tuations play a central role in turbulence physics, micrometeorology and boundary-layer meteorology. Of key interest in the physics of optical propagation through the turbulent atmosphere is the second-order refractive-index structure function,

$$D_{nn}(\mathbf{x},\mathbf{r}) \equiv \langle [\Delta_n(\mathbf{x},\mathbf{r})]^2 \rangle, \tag{6}$$

where $\mathbf{x}$ is the location in 3D space, $\mathbf{r}$ is the separation vector between the two locations $\mathbf{x}$ and $\mathbf{x}+\mathbf{r}$, $\langle\cdot\rangle$ is the ensemble average, and

$$\Delta_n(\mathbf{x},\mathbf{r}) \equiv n(\mathbf{x}+\mathbf{r}) - n(\mathbf{x}) \tag{7}$$

is referred to as the spatial *increment* of the refractive-index fluctuations.

If the turbulence is homogeneous, then $D_{nn}(\mathbf{x},\mathbf{r})$ is independent of $\mathbf{x}$, and if the turbulence is homogeneous and isotropic, then $D_{nn}(\mathbf{x},\mathbf{r})$ is a function only of $r \equiv |\mathbf{r}|$. According to the classical theory of scalar turbulence (Obukhov, 1949; Tatarskii, 1961), $D_{nn}(r)$ follows an $r^{2/3}$ power law in the convective-inertial subrange of fully developed turbulence:

$$D_{nn}(r) = C_n^2 r^{2/3}, \tag{8}$$

such that

$$C_n^2 = \frac{\langle [\Delta_n(\mathbf{x},\mathbf{r})]^2 \rangle}{r^{2/3}}, \tag{9}$$

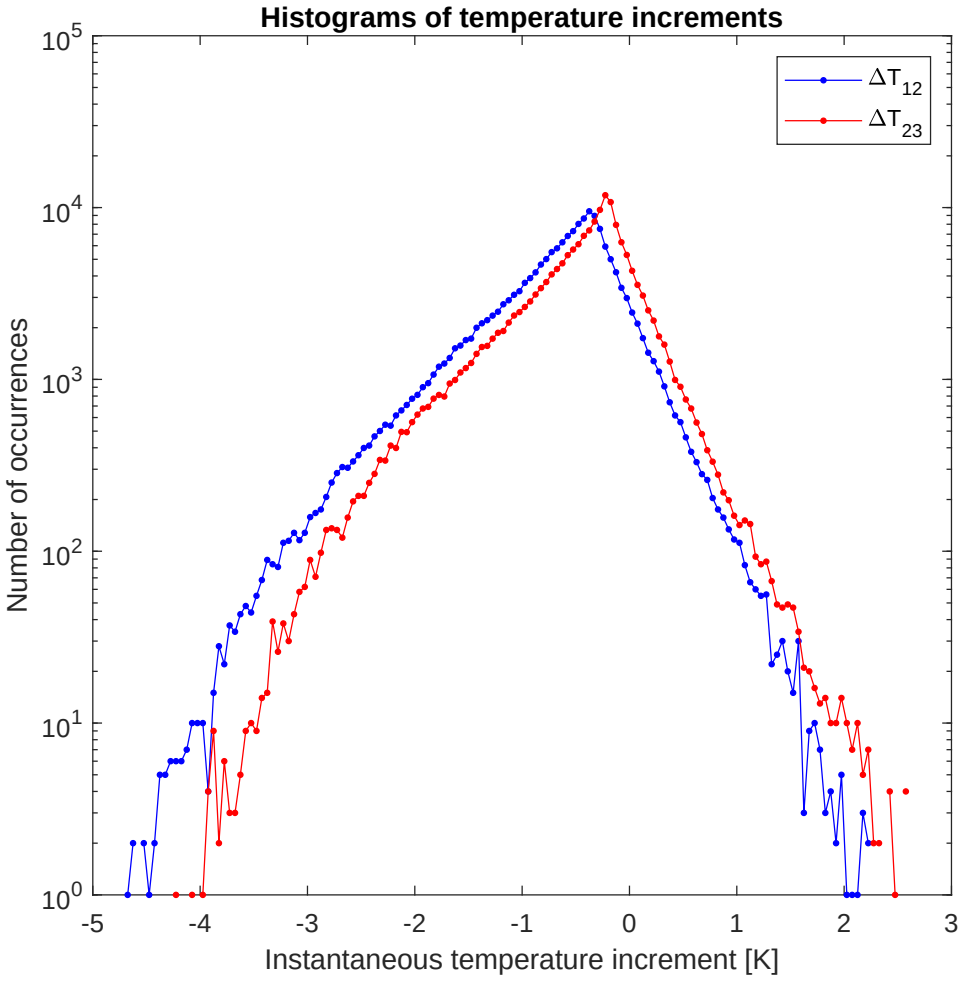

Figure 13: *Histograms of instantaneous, vertical temperature increments observed during the 1-h long period beginning at 1700 UTC on 8 June, 2019 at the Table Mountain Test Facility near Boulder, CO.*

provided that the turbulence is homogeneous, isotropic and fully developed, and that r is within the inertial-convective subrange.

Interestingly, the "two-thirds law" stated in Eq. (8) does not rely on any assumption about the p.d.f. of the refractive-index increments. On the other hand, for higher-order statistics, such as the fourth-order structure function

$$D_4(\mathbf{x}, \mathbf{r}) \equiv \langle [\Delta_n(\mathbf{x}, \mathbf{r})]^4 \rangle, \tag{10}$$

the p.d.f. of the refractive-index increments is expected to be important.

Let us consider an R.V. x with a two-sided, exponential p.d.f.,

$$f(x) = \begin{cases} Ae^{ax} & , \quad x \leq 0 \\ Be^{-bx} & , \quad x \geq 0 \end{cases} , \tag{11}$$

where A, B, a and b are real-valued, positive constants. Continuity of $f(x)$ at $x = 0$ requires

$$A = B. \tag{12}$$

The nth statistical moment of x is defined as the expected value of x^n:

$$M_n = \langle x^n \rangle, \tag{13}$$

and it can be determined from the p.d.f.:

$$M_n = \int_{-\infty}^{\infty} f(x) x^n \mathrm{d}x. \tag{14}$$

Combining (11) and (14) with the relationship

$$\int_0^{\infty} x^n e^{-\mu x} \mathrm{d}x = n! \mu^{-n-1} \tag{15}$$

(Gradshteyn and Ryzhik, 1980, p. 310, #3.3551-3) gives

$$M_n \equiv \langle x^n \rangle = A\, n! \left[(-1)^n a^{-n-1} + b^{-n-1} \right]. \tag{16}$$

This gives

$$M_0 = A \left(\frac{1}{a} + \frac{1}{b} \right), \tag{17}$$

and the general normalization requirement

$$M_0 = \int_{-\infty}^{\infty} f(x) x^n \mathrm{d}x = 1 \tag{18}$$

gives

$$A = \frac{1}{\frac{1}{a} + \frac{1}{b}} = \frac{ab}{a+b}. \tag{19}$$

Therefore,

$$M_n = \frac{ab}{a+b} n! \left[(-1)^n a^{-n-1} + b^{-n-1} \right]. \tag{20}$$

We expect this model to be useful for a deeper understanding of optical turbulence.

2.1.6 Development and field testing of fine-wire thermometers

The sampling volume size of an ultrasonic anemometer-thermometer is typically larger than 10 cm, such that the inner scale of turbulence, ℓ_0, which typically ranges between a few millimeters and a few centimeters, cannot be resolved. The fine-wire thermometer is the instrument of choice for the observation of temperature fluctuations down to length scales of 1 mm and down to time scales of less than 1 ms. We developed and field-tested a fine-wire thermometer system, as described in

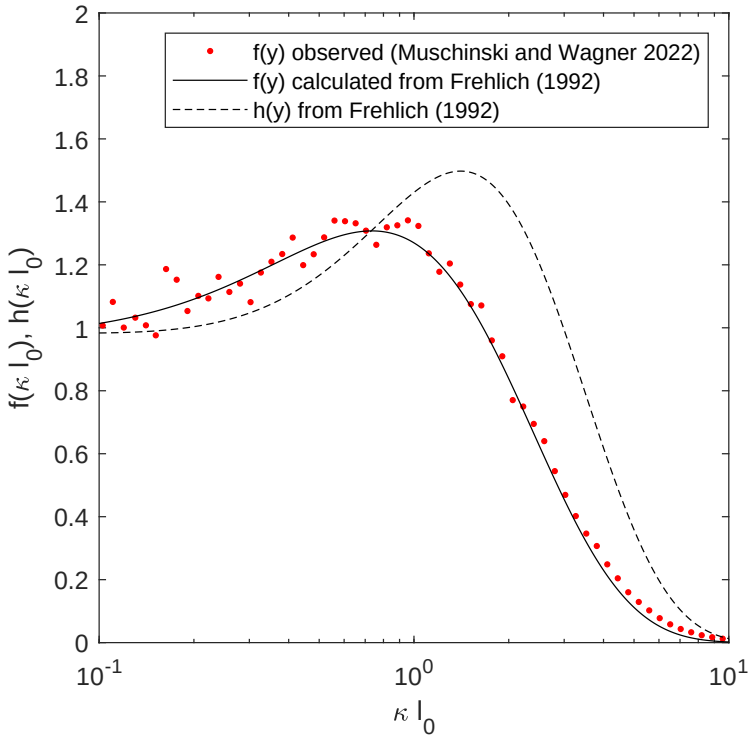

Figure 14: *Model and field measurements of the "Hill bump". Dashed line: 3D tail function* $h(\kappa\ell_0)$ *according to Frehlich (1992, Eqs. 23 and 24 on pp. 1496f.); solid line: 1D tail function* $f(\kappa\ell_0)$ *calculated from Frehlich's* $h(\kappa\ell_0)$; red dots: 1D tail function $f(\kappa\ell_0)$ retrieved from fine-wire temperature measurements described in Muschinski and Wagner (2023).

Muschinski and Wagner (2023), which is attached at the end of this report and which will appear in the upcoming "Special Issue in honour of V.I. Tatarskii (1929-2020)" of *Wave Propapation of Complex and Random Media*.

A controversial topic in recent decades has been how to correctly model the anomaly in the temperature spectrum at wavenumbers compared to $1/\ell_0$, that is, in the transition regime between the inertial-convective subrange and the viscous-diffusive subrange. This anomaly is known as the "Hill bump," named after Hill (1978) who developed a theoretical model that accounts for the bump. Various empirical models for the Hill bump have been suggested since about 1990 but, as shown by Muschinski (2015), all of them, with the exception of Frehlich's model (Frehlich, 1992, Eqs. 23 and 24 on pp. 1496f.), violate the scalar transport equation, a first principle of fluid mechanics. Frehlich's model is a closed-form approximation to a numerical solution of the differential equation that defines Hill's "Model 4" (Hill, 1978). Muschinski and de Bruyn Kops (2015) showed that Frehlich's model agrees very well with direct numerical simulations (DNS) of the Navier-Stokes equation in combination with the scalar transport equation.

Recently (Muschinski, 2022), we analyzed our fine-wire temperature measurements and found also very good agreement with Frehlich's model; see Fig. 14.

2.1.7 Measurement physics of fine-wire turbulence sensors

A fine-wire thermometer is a resistance thermometer. The resistor is a thin wire, typically of platinum, with a length L typically of order 1 mm and a diameter D typically of order 1 μm. The measurement physics of a fine-wire thermometer is closely related to that of a hot-wire anemometer, which was pioneered by King (1914) and others in the early 20th century. In general, the fine-wire resistance (the primary observable) is a function of both air temperature and air velocity. While the purpose of a hot-wire anemometer is to maximize the velocity sensitivity and to minimize the temperature sensitivity, a fine-wire thermometer is designed and operated such that the temperature sensitivity is maximized and the velocity sensitivity minimized. This is achieved by using extremely thin wires and by keeping the wire temperature only slightly above the ambient air temperature. Therefore, a fine-wire thermometer is often referred to as a "cold-wire thermometer".

The literature on fine-wire anemometry and thermometry spans more than a century (King, 1914; Corrsin, 1947, 1963; Wyngaard, 1971; LaRue et al., 1975; Comte-Bellot, 1976; Williams and Paulson, 1977; Mestayer and Chambaud, 1979; Bruun, 1995; Kit, 2013).

The purpose of the following is to present the measurement physics of the fine-wire thermometer on the basis of heat transfer theory (Nusselt, 1915; Holman, 2002; Lienhard IV and Lienhard V, 2019), the theory of linear, time-invariant systems (Ziemer et al., 1993; Lathi, 2005; Roberts, 2008), and the theory of stochastic processes and random fields (Yaglom, 1962; Monin and Yaglom, 1975).

A fine-wire thermometer is operated in the "cold-wire mode," in the sense that, ideally, the instantaneous wire temperature T_w is equal to the instantaneous ambient-air temperature T_a. Measuring T_w, however, requires measuring the wire's resistance, which requires a non-zero voltage drop across the wire and, therefore, a finite current, I. A finite current, however, heats the wire to a temperature $T_w > T_a$, and the wire transfers its thermal energy excess to the ambient air via conductive heat transfer (King, 1914; Nusselt, 1915). The choice of the current I is of central importance for optimizing the fine-wire thermometer's performance. Important performance characteristics, which we will analyze in the following, are the frequency response, the velocity sensitivity, and the signal-to-noise ratio.

We consider a fine wire that is electrically heated by a current I. Then the rate of thermal energy released into the wire by means of Joule heating is

$$P_e = R_w I^2, \tag{21}$$

where R_w is the wire's resistance. In general, both I and R_w are functions of time t.

In the general case, the instantaneous T_w varies along the wire, along its circumference, and within the wire as a function of the radial coordinate. Heat conduction along the wire, combined with the comparatively large heat capacity of the prongs, causes the wire temperature at the ends of the fine wire to be equal to the mean ambient air temperature. This phenomenon is known as the "end effect". The portion of the heated fine wire that is "cold" is referred to as the "cold length," ℓ_c, and the ratio ℓ_c/L decreases with increasing aspect ratio, L/D. Theoretical details of the cold length can be found in Bruun (1995, pp. 23-26 and pp. 563f.) and in Corrsin (1963). Moreover, as the wire is electrically heated and cooled by convective heat transfer to the ambient air, the interior of the wire is usually warmer than its surface.

In the following, we ignore temperature inhomogeneities within the wire and allow T_w to vary with time but not as a function of the location within the wire. Then, conservation of energy leads to

the energy budget equation

$$P_e = P_w + P_h, \tag{22}$$

where P_w is the portion of P_e that is "used" to heat the wire and P_h is the portion of P_e that heats the ambient air due to convective heat transfer. In general, there is a third term on the right-hand side of Eq. (22), namely, the loss of energy due to radiative heat transfer. It can be easily shown, however, that for fine-wire thermometers radiative heat transfer is negligible compared to convective heat transfer.

The first term in Eq. (22) is

$$P_e = R_w I^2, \tag{23}$$

where

$$R_w = R_0 \left[1 + \alpha_0 (T_w - T_0)\right] \tag{24}$$

is the wire's resistance, T_0 is a reference temperature, and α_0 is the temperature coefficient of the wire material at T_0. (Here we assume that α_0 is constant within the temperature range between T_0 and T_w.). R_0 is the wire resistance for $T_w = T_0$,

$$R_0 = \frac{L}{\pi (D/2)^2} \chi_0, \tag{25}$$

where χ_0 is the resistivity of the wire material at T_0, and L and D are the length and the diameter, respectively, of the wire.

The second term in Eq. (22) is

$$P_w = C_w \frac{\partial T_w}{\partial t}, \tag{26}$$

where

$$C_w = \pi \left(\frac{D}{2}\right)^2 L \rho_w c_w \tag{27}$$

is the wire's heat capacity. Here, $\pi(D/2)^2 L$ is the wire's volume, ρ_w its mass density, and c_w is the specific heat capacity (heat capacity per unit mass) of the wire material.

The third term in Eq. (22) has the form

$$P_h = \pi D L h \theta, \tag{28}$$

where πDL is the surface area of a long cylinder ($L \gg D$), h is the heat transfer coefficient (transferred energy per unit time, per unit surface area, and per unit temperature difference), and

$$\theta = T_w - T_a \tag{29}$$

is the "overheat," that is, the difference between wire temperature and ambient-air temperature.

The modern theory of heat transfer was pioneered by Nusselt (1915). He considered the general case of a solid body immersed in a fluid and showed, based on dimensional analysis of the underlying first principles (the conservation of momentum, the conservation of mass, and the conservation of

energy), that the heat transfer between the body and the fluid is characterized by a dimensionless parameter $\varphi = hl/k$, where h is the heat transfer coefficient averaged over the body's surface, l is a characteristic length scale, and k is the fluid's heat conductivity. Nusselt showed that for a given body shape and flow configuration, φ is a universal function of various dimensionless parameters, such as the Reynolds number, the Prandtl number, the Mach number, and the Grashof number (Nusselt, 1915, p. 495, Eq. 60). In the modern literature, the parameter φ is called the Nusselt number, Nu.

In the case of a long cylindrical body in cross-flow, the relevant length scale is D and not L, such that

$$h = \frac{k}{D}\mathrm{Nu}. \tag{30}$$

In their comprehensive meta-study on measurements of heat transfer in cross flow past cylinders, Churchill and Bernstein (1977, p. 302, Eq. 4) recommend for low Reynolds numbers ($\mathrm{Re} < 4000$) the following relationship for Nu as function of Re and Prandtl number Pr:

$$\mathrm{Nu} = 0.3 + 0.62\frac{\mathrm{Pr}^{1/3}}{[1 + (0.4/\mathrm{Pr})^{2/3}]^{1/4}}\mathrm{Re}^{1/2}; \tag{31}$$

see also Holman (2002) and Lienhard IV and Lienhard V (2019). With regard to the constant 0.3 in Eq. (31), Churchill and Bernstein (1977, p. 302) point out: "The theoretical solution of King King (1914) for potential flow actually yielded a value of $1/\pi = 0.381$ . . . but his choice of boundary conditions has been called improper by Hill and Sleicher, Jr. (1969)."

For a given value of Pr, Nu can be stated as

$$\mathrm{Nu} = A + B\sqrt{\mathrm{Re}}, \tag{32}$$

where the dimensionless coefficients A and B for a given fluid are constants. Eq. (32) is known as King's law, after King's pioneering study (King, 1914, p. 381, Eq. 3).

Some authors suggest a "generalized King's law" of the form

$$\mathrm{Nu} = A + B\mathrm{Re}^n, \tag{33}$$

where the value of the exponent n is allowed to differ from 0.50. For example, for low Reynolds numbers ($0.02 < \mathrm{Re} < 44$), Collis and Williams (1959, p. 370, Table 3) recommended $n = 0.45$, with $A = 0.24$ and $B = 0.56$, and Wyngaard (1971) used the Collis-Williams model to derive the velocity sensitivity of fine-wire thermometers.

Inserting the foregoing expressions for P_e, P_w, and P_h into Eq. (22) gives

$$R_0 I^2 \left[1 + \alpha_0(T_w - T_0)\right] = C_w\frac{\partial T_w}{\partial t} + \pi k L \mathrm{Nu}(T_w - T_a). \tag{34}$$

Now, we write T_w and T_a as sums of their respective mean values and zero-mean fluctuations,

$$T_w = \langle T_w \rangle + \theta_w \tag{35}$$

and

$$T_a = \langle T_a \rangle + \theta_a, \tag{36}$$

such that $\langle\theta_w\rangle = 0$ and $\langle\theta_a\rangle = 0$, and we denote the instanteneous temperature difference, or "overheat", as

$$\theta = T_w - T_a. \tag{37}$$

The mean overheat is

$$\langle\theta\rangle = \langle T_w\rangle - \langle T_a\rangle. \tag{38}$$

In general, both T_a and the true air speed U are random variables,

$$U = \langle U\rangle + u, \tag{39}$$

where u is the zero-mean fluctuation of U. Then, the Reynolds number,

$$\mathrm{Re} = \frac{UD}{\nu} \tag{40}$$

(where ν is the kinematic viscosity of air) is also a random variable.

In order to discuss Eq. (34) in detail, we first evaluate Nu. Assuming that the generalized King's law, Eq. (33), is valid, and assuming that the velocity fluctuations are small ($|u| \ll U$), a first-order Taylor expansion gives

$$\mathrm{Nu} = A + B\langle\mathrm{Re}\rangle^n + B\langle\mathrm{Re}\rangle^n n\frac{u}{\langle U\rangle}, \tag{41}$$

where

$$\langle\mathrm{Re}\rangle = \frac{\langle U\rangle D}{\nu} \tag{42}$$

is the expected value of the Reynolds number.

Equating the expected values and the fluctuations, respectively, on both sides of Eq. (34) gives, after setting $T_0 = \langle T_w\rangle$ as the reference temperature and after elementary manipulations,

$$\theta_w + a\frac{\partial\theta_w}{\partial t} = b\theta_a + cu, \tag{43}$$

where

$$a = \frac{C_w}{(1-\alpha_0\langle\theta\rangle)\pi Lk\,(A + B\langle\mathrm{Re}\rangle^n)}, \tag{44}$$

$$b = \frac{1}{1-\alpha_0\langle\theta\rangle}, \tag{45}$$

and

$$c = -\frac{B\langle\mathrm{Re}\rangle^n n\langle\theta\rangle}{(1-\alpha_0\langle\theta\rangle)(A + B\langle\mathrm{Re}\rangle^n)\langle U\rangle} \tag{46}$$

are constant system parameters. The constant a in (44) is the time constant of the fine-wire sensor.

Let us assume that $T_w(t)$ is a statistically stationary random process, such that $\langle \partial T_w/\partial t\rangle = 0$. Then, again choosing $T_0 = \langle T_w\rangle$ as the reference temperature, equating the expected values of both sides of Eq. (34) gives

$$\langle\theta\rangle = \frac{R_0 I^2}{\pi k L \langle \mathrm{Nu}\rangle}, \tag{47}$$

or, by means of Eq. (25),

$$\langle\theta\rangle = \frac{4\chi_0}{\pi^2 k\langle \mathrm{Nu}\rangle}\left(\frac{I}{D}\right)^2. \tag{48}$$

Here,

$$\langle \mathrm{Nu}\rangle = A + B\langle \mathrm{Re}\rangle^n \tag{49}$$

is the expected value of the Nusselt number.

Now, let us consider the case that $T_a(t)$ is a stationary random process with expected value $\langle T_a\rangle$ and zero-mean fluctuation $\theta_a(t)$, such that

$$T_a(t) = \langle T_a\rangle + \theta_a(t), \tag{50}$$

where $\theta_a(t)$ can be written as a stochastic Fourier-Stieltjes integral,

$$\theta_a(t) = \int_{-\infty}^{\infty} \exp(i\omega t)\mathrm{d}Z_a(\omega); \tag{51}$$

see, e.g., Yaglom (1962, Eq. 2.37 on p. 37 and Eq. 2.40 on p. 38) and Monin and Yaglom (1975, Eq. 11.52 on p. 19). Here, the increments $\mathrm{d}Z_a(\omega)$ are statistically orthogonal in the sense

$$\langle \mathrm{d}Z_a^*(\omega)\mathrm{d}Z_a(\omega')\rangle = \delta(\omega-\omega')\phi_a(\omega)\mathrm{d}\omega\mathrm{d}\omega' \tag{52}$$

(Monin and Yaglom, 1975, Eq. (11.53) on p. 19), where $\phi_a(\omega)$ is the (two-sided) spectral density of $T_a(t)$.

Correspondingly, the wire temperature is also a stationary random process,

$$T_w(t) = \langle T_w\rangle + \theta_w(t), \tag{53}$$

where the zero-mean fluctuations can also be written as a Fourier-Stieltjes integral,

$$\theta_w(t) = \int_{-\infty}^{\infty} \exp(i\omega t)\mathrm{d}Z_w(\omega) \tag{54}$$

Its time derivative is also a zero-mean stationary random process,

$$\frac{\partial\theta_w(t)}{\partial t} = \int_{-\infty}^{\infty} i\omega\exp(i\omega t)\mathrm{d}Z_w(\omega). \tag{55}$$

The Fourier-Stieltjes representation of the zero-mean true-air-speed flucutation $u(t)$ is

$$u(t) = \int_{-\infty}^{\infty} \exp(i\omega t) \mathrm{d}Z_u(\omega). \tag{56}$$

Inserting the Fourier-Stieltjes representations of θ_w, θ_a, and u into the system equation (43) gives, after equating the integrands on both sides of the resulting equation,

$$\mathrm{d}Z_w(\omega) = H_a(\omega)\mathrm{d}Z_a(\omega) + H_u(\omega)\mathrm{d}Z_u(\omega), \tag{57}$$

where

$$H_a(\omega) = \frac{b}{1 + ia\omega} \tag{58}$$

and

$$H_u(\omega) = \frac{c}{1 + ia\omega} \tag{59}$$

are the transfer functions for θ_a and u, respectively.

The (normalized) frequency responses for θ_a and u are equal to each other,

$$\frac{|H_a(\omega)|^2}{|H_a(0)|^2} = \frac{|H_u(\omega)|^2}{|H_u(0)|^2} = \frac{1}{1 + (f/f_c)^2}, \tag{60}$$

where $f = \omega/2\pi$ and

$$f_c = \frac{1}{2\pi a} \tag{61}$$

is the corner frequency, or 3-dB frequency, of the fine-wire sensor.

2.1.8 Theoretical study of turbulent phase screens

One objective of this project was to evaluate the relative advantages and disadvantages of various methods and models to describe, predict, and analyze optical propagation through a random (turbulent or non-turbulent) refractive-index field in the stably stratified atmosphere. Three of the most widely used methods are, respectively, the geometrical-optics method, the Rytov method, and the LSI systems method. (Here, "LSI" stands for "linear, shift-invariant". LSI systems are the 2D spatial counterparts of linear, time-invariant, or LTI, systems.) The concept of random phase screens is central to the LSI systems approach of analyzing and predicting optical wave propagation through the turbulent atmosphere. In Muschinski (2021), we analyzed second-order statistics (autocovariance functions, structure functions, and power spectra) of the phase factor of phase screens characterized by a power-law phase structure function and by a phase-increment probability density function. We analyzed four specific kinds of phase screens. Each of these phase screens is specified by a power-law exponent (5/3 or 2) of the phase structure function and by a phase-increment probability density function (Gaussian or Laplacian). We find that at high wavenumbers (representing length scales small compared to the Fried length), the phase-factor spectra of turbulent (power-law exponent 5/3) phase screens converge to the phase spectra predicted by Tatarskii, regardless of whether the phase increments are Gaussian- or Laplacian-distributed. At length scales comparable to the Fried length, however, the second-order statistics of the phase factor are different for

Gaussian versus Laplacian phase increments. A second important finding is that the phase-factor spectra show "bumps" at wavenumbers comparable to the Fried wavenumber.

The classical theory of wave propagation through turbulent media (Tatarskii, 1961) solves the scalar Helmholtz equation based on the geometrical-optics approximation ("ray tracing") or the Rytov approximation. A major flaw of the geometrical-optics method is that diffraction effects are not accounted for, while a major disadvantage of the Rytov method is that it leads to incorrect, or at least questionable, results if the irradiance fluctuations are not small to the mean irradiance.

The LSI systems method (Goodman, 1968, 2017, 2020; Roggemann and Welsh, 1996; Schmidt, 2010; Voelz, 2011), however, is free from both problems: it accounts for both refraction and diffraction effects, and its applicability is not restricted to weak-scattering scenarios.

The results of Muschinski (2021) are as follows:

1. The phase-*factor* statistics $B_\psi(r)$, $D_\psi(r)$, and $F_\psi(\kappa)$ are all "well-behaved". (Here, $\psi = \exp[i\phi]$ is the phase *factor*, ϕ is the phase, and $B_\psi(r)$, $D_\psi(r)$, and $F_\psi(\kappa)$ are the covariance, the structure function, and the spectrum, respecively, of ψ.) In particular, in contrast to their phase counterparts $B_\phi(r)$, $D_\phi(r)$, and $F_\phi(\kappa)$, the ψ statistics show no singularities at $r = 0$, $r \to \infty$, $\kappa = 0$, and $\kappa \to \infty$ if the underlying phase structure function $D_\phi(r)$ follows the power laws $r^{5/3}$ or r^2.

2. We have defined a phase coherence length, r_c, by requiring $D_\phi(r_c) = 1\,\mathrm{rad}^2$. For $\gamma = 5/3$, our r_c is physically equivalent to Fried's coherence length r_0, except for the numerical factor $r_0/r_c = 6.88^{3/5} = 3.18$. We show that both r_c and r_0 are pure phase-screen statistics based on optical path-length ("eikonal") fluctuations. Both r_c and r_0 are unaffected by any assumptions or approximations regarding the propagation after passing through the phase screen.

3. We have formulated the second-order phase-factor structure function $D_\psi(r)$ as an infinite sum of second- and higher-order (of even order) phase structure functions, $D_\phi^{(2n)}(r)$. For $r \ll r_c$, we find $D_\psi(r) \approx D_\phi(r)$. For $r \gg r_c$, however, $D_\psi(r)$ saturates to the universal value 2 while $D_\phi(r)$ increases without bound.

4. For turbulent ($\gamma = 5/3$) phase screens, at high wavenumbers ($\kappa \gg r_c^{-1}$) the dimensionless phase-spectra $f_\psi(K)$ (where $K = \kappa r_c$ is a dimensionless wavenumber) for Gaussian and Laplacian phase increments converge to the same power law, $f_\psi(K) = 0.45\,K^{-11/3}$. The only parameter that affects this result is $\gamma = 5/3$.

5. Independently, we have retrieved the $K \gg 1$ asymptote of $f_\psi(K)$ from Tatarskii's (Tatarskii, 1961) relationships $F_\psi(\kappa) = 2\pi k^2 L \times 0.033 C_n^2 \kappa^{-11/3}$ and $D_\phi(r) = 2.91 k^2 L C_n^2 r^{5/3}$, and we find the same power law and the same coefficient, $f_\psi(K) = 0.45\,K^{-11/3}$.

6. For phase screens with quadratic ($\gamma = 2$) phase structure functions, $f_\psi(K)$ drops exponentially for $K \gg 1$, more rapidly for Gaussian than for Laplacian phase increments.

7. At low wavenumbers ($\kappa \ll r_c^{-1}, K \ll 1$), all four ψ spectra become flat, which is consistent with the fact that ψ becomes uncorrelated for $r \gg r_c$.

8. At intermediate wavenumbers ($\kappa \sim r_c^{-1}, K \sim 1$), each of the four $f_\psi(K)$ shows a "bump," in the case $\gamma = 5/3$ exceeding the high-wavenumber asymptote, $f_\psi(K) = 0.45\,K^{-11/3}$, by a factor of up to 2.8 for Gaussian phase increments and a factor of up to 2.2 for Laplacian phase increments.

2.1.9 Long-range propagation along a 84-km path across White Sands Missile Range

During the first week of October, 2022, we carried out a long-range optical propagation experiment involving five nearly horizontal propagation paths of length 84 km, which ran several hundred meters above ground level across the southern part of White Sands Missile Range.

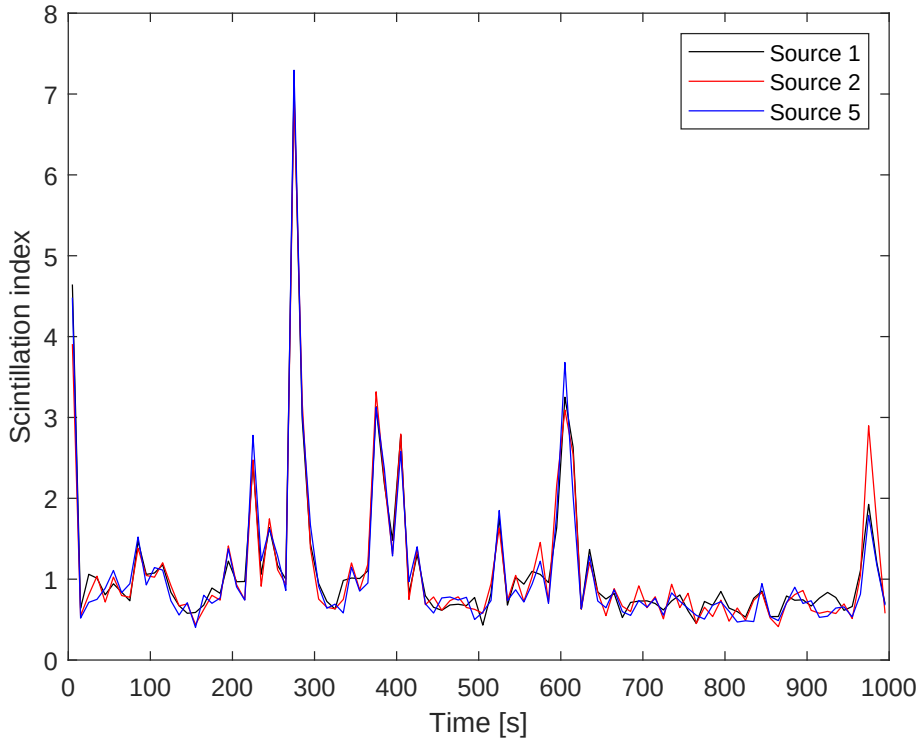

Figure 15: *Time series of 10-s estimates of the scintillation indices observed with three different test lights. The data were collected in October, 2022 at White Sands Missile Range, NM. The propagation path was 84 km long.*

An array of five test lights was deployed at the site of the Sunspot Observatory, NM, and we imaged these lights at nighttime with two telescopes, each equipped with a digital camera. The telescopes were located at the Aguirre Spring Campground on the east side of the Organ Mountains near Las Cruces, NM. The telescopes' aperture diameters were 14 cm and 8 cm. Each of the five "sources" consisted of a red, a green, and a blue high-power (3 W each), light-emitting diode (LED) system.

Fig. 15 shows some preliminary results from Run 8210, which consisted of a sequence of 60,554 images collected during a 17-min period in the evening of October 2, 2022, starting at 2215 MDT. The images were collected with a Canon EOS 5D Mark III digital color camera attached to the 14-inch telescope. The camera was run in a video mode at 60 frames per second. The exposure time was 1 ms. The test lights were distributed laterally, such that the spacing between Source 1 and Source 5 was 61 m, which corresponds to 61/84,000 rad, or 0.7 milliradians. Sources 1, 2, and 5 could be easily separated in each of the frames but the images of Sources 3 and 4 (spaced by only 5 m, corresponding to 60 μrad) overlapped. In the initial phase of the post-processing, we decomposed each color frame into a red, a green, and a blue frame, and we retrieved the brightnesses for each individual source (except for sources 3 and 4, which we could not separate) and each color channel.

Fig. 15 shows the time series of 10-s estimates of the scintillation indices for sources 1, 2, and 5 observed through the green color channel. The scintillation indices for the three sources track each other well. Most of the time, the scintillation index ranged between 0.5 and 1.5, which is much larger than what one would expect from classical theory in the case of a Fried length much smaller than the aperture diameter (compare Section 2.1.3). Fig. 15 shows that the scintillation index occasionally increases to values much larger than 1.5 (up to about 7 at $t = 275$ s). It is interesting that these maxima in the scintillation index occur simultaneously (at the estimation time scale of 10 s) in all three time series.

We are still in the initial phase of our data analysis. At this point, we cannot provide a comprehensive explanation of our observations.

Bibliography

Andreas, E. L., (Ed.) , 1990: *Turbulence in a refractive medium*, SPIE Milestone Series, Vol. MS 25. SPIE Optical Engineering Press, Bellingham, Washington, USA, 693 pp.

Andrews, L. C. and R. L. Phillips, 2005: *Laser beam propagation through random media*. 2d ed., SPIE Press, Bellingham, Washington, 783 pp.

Bean, B. R. and E. J. Dutton, 1966: *Radio Meteorology*. U. S. Government Printing Office, Washington, D. C., 435 pp.

Beland, R. R., 1993: Propagation through atmospheric optical turbulence. *The infrared and electro-optical systems handbook, Vol. 2 (Atmospheric propagation of radiation)*, F. G. Smith, Ed., SPIE Optical Engineering Press, Bellingham, Washington, USA, 157–232.

Bruun, H. H., 1995: *Hot-wire anemometry*. Oxford University Press, Oxford, United Kingdom, 507 pp.

Businger, J. A., J. C. Wyngaard, Y. Izumi, and E. F. Bradley, 1971: Flux-profile relationships in the atmospheric surface layer. *J. Atmos. Sci.*, **28**, 181–189.

Caldwell, E. D., et al., 2020: Optical timing jitter due to atmospheric turbulence: comparison of frequency comb measurements to predictions from micrometeorological sensors. *Opt. Exp.*, **28**, 26,661–26,675.

Cheon, Y., V. Hohreiter, M. Behn, and A. Muschinski, 2007: Angle-of-arrival anemometry by means of a large-aperture Schmidt-Cassegrain telescope equipped with a CCD camera. *J. Opt. Soc. Am. A*, **24**, 3478–3492.

Churchill, S. W. and M. Bernstein, 1977: A correlating equation for forced convection from gases and liquids to a circular cylinder in crossflow. *J. Heat Transfer*, **99**, 300–306.

Clifford, S. F., 1978: The classical theory of wave propagation in a turbulent medium. *Laser beam propagation in the atmosphere*, J. W. Strohbehn, Ed., Springer, Berlin, 9–43.

Collis, D. C. and M. J. Williams, 1959: Two-dimensional convection from heated wires at low Reynolds numbers. *J. Fluid Mech.*, **6**, 357–384.

Comte-Bellot, G., 1976: Hot-wire anemometry. *Annu. Rev. Fluid Mech.*, **8**, 209–231.

Corrsin, S., 1947: Extended applications of the hot-wire anemometer. *Rev. Sci. Instrum.*, **18**, 469–471.

Corrsin, S., 1951: On the spectrum of isotropic temperature fluctuations in an isotropic turbulence. *J. Appl. Phys.*, **22**, 469–473.

Corrsin, S., 1963: Turbulence: experimental methods. *Handbuch der Physik, Bd. VIII/2, Strömungsmechanik II*, S. Flügge, Ed., Springer-Verlag, Boston, 524–590.

Frehlich, R. G., 1992: Laser scintillation measurements of the temperature spectrum in the atmospheric surface layer. *J. Atmos. Sci.*, **49**, 1494–1509.

Goodman, J. W., 1968: *Introduction to Fourier optics*. 1st ed., McGraw-Hill, Boston, Massachusetts, 287 pp.

Goodman, J. W., 2015: *Statistical optics*. 2d ed., John Wiley & Sons, Hoboken, New Jersey, 516 pp.

Goodman, J. W., 2017: *Introduction to Fourier optics*. 4th ed., W. H. Freeman and Company, New York, New York, 546 pp.

Goodman, J. W., 2020: *Speckle phenomena in optics*. 2d ed., SPIE Press, Bellingham, Washington, United States, 452 pp.

Gradshteyn, I. S. and I. M. Ryzhik, 1980: *Table of integrals, series, and products*. 4th ed., Academic Press, New York, 1160 pp.

Heisenberg, W., 1948: Zur statistischen Theorie der Turbulenz. *Z. Phys.*, **124**, 628–657.

Helmholtz, H., 1859: Theorie der Luftschwingungen in Röhren with offenen Enden (Theory of air oscillations in pipes with open ends). *J. f. reine u. angew. Math.*, **57**, 1–72.

Hill, J. C. and C. A. Sleicher, Jr., 1969: Convective heat transfer from small cylinders to mercury. *Int. J. Heat Mass Transfer*, **12**, 1595–1604.

Hill, R. J., 1978: Models of the scalar spectrum for turbulent advection. *J. Fluid Mech.*, **88**, 541–562.

Holman, J. P., 2002: *Heat transfer*. 9th ed., McGraw-Hill, New York, 665 pp.

Ishimaru, A., 1978: *Wave propagation and scattering in random media, Vol. 2, Scattering in random media*. Academic Press, Boston, Massachusetts, 251-572 pp.

King, L. V., 1914: On the convection of heat from small cylinders in a stream of fluid: Determination of the convection constants of small platinum wires with applications to hot-wire anemometry. *Phil. Trans. Roy. Soc. Lond. A*, **214**, 373–432.

Kit, E., 2013: Hot-wire anemometry in turbulence research. *Handbook of environmental fluid dynamics, Vol. 2*, H. J. S. Fernando, Ed., CRC Press, Boca Raton, FL, 467–479.

Korotkova, O., 2014: *Random light beams: theory and applications*. CRC Press, Boca Raton, 361 pp.

Korotkova, O., 2022: *Theoretical statistical optics*. World Scientific Publishing, Hackensack, New Jersey, 319 pp.

LaRue, J. C., T. Deaton, and C. H. Gibson, 1975: Measurement of high-frequency turbulent temperature. *Rev. Sci. Instrum.*, **46**, 757–764.

Lathi, B. P., 2005: *Linear systems and signals*. 2d ed., Oxford University Press, Oxford, United Kingdom, 975 pp.

Lienhard IV, J. H. and J. H. Lienhard V, 2019: *A heat transfer textbook*. 5th ed., Phlogiston Press, Cambridge, Massachusetts, 771 pp.

Martin, J. M. and S. M. Flatté, 1988: Intensity images and statistics from numerical simulation of wave propagation in 3-D random media. *Appl. Opt.*, **27**, 2111–2126.

Mestayer, P. and P. Chambaud, 1979: Some limitations to measurements of turbulence microstructure with hot and cold wires. *Boundary-Layer Meteorol.*, **16**, 311–329.

Monin, A. S. and A. M. Yaglom, 1975: *Statistical fluid mechanics — Volume 2*. The MIT Press, Cambridge, Massachusetts, 874 pp.

Muschinski, A., 2015: Temperature variance dissipation equation and its relevance for optical turbulence modeling. *J. Opt. Soc. Am. A*, **32**, 2195–2200.

Muschinski, A., 2021: Phase-factor spectra of turbulent phase screens. *J. Opt. Soc. Am. A*, **38**, 1339–1348.

Muschinski, A., 2022: Non-classical models of optical turbulence. *Unconventional Imaging and Adaptive Optics 2022*, SPIE, Vol. 12239, 1223902.

Muschinski, A. and S. M. de Bruyn Kops, 2015: Investigation of Hill's optical turbulence model by means of direct numerical simulation. *J. Opt. Soc. Am. A*, **32**, 2423–2430.

Muschinski, A., R. Frehlich, M. Jensen, R. Hugo, A. Hoff, F. Eaton, and B. Balsley, 2001: Fine-scale measurements of turbulence in the lower troposphere: an intercomparison between a kite- and balloon-borne, and a helicopter-borne measurement system. *Boundary-Layer Meteorol.*, **98**, 219–250.

Muschinski, A., R. G. Frehlich, and B. B. Balsley, 2004: Small-scale and large-scale intermittency in the nocturnal boundary layer and the residual layer. *J. Fluid Mech.*, **515**, 319–351.

Muschinski, A. and D. G. Voelz, 2019: Probability densities of atmospheric optical scintillation observed with large apertures. *Propagation Through and Characterization of Atmospheric and Oceanic Phenomena*, Optical Society of America, PTh3C–3.

Muschinski, A. and E. L. Wagner, 2023: First field measurements of optical turbulence near the ground with a newly developed fine-wire thermometer. *Waves Rand. Comp. Med.*, **33**, in press.

Newman, J. F., P. M. Klein, S. Wharton, A. Sathe, T. A. Bonin, P. B. Chilson, and A. Muschinski, 2016: Evaluation of three lidar scanning strategies for turbulence measurements. *Atmos. Meas. Tech.*, **9**, 1993–2013.

Nusselt, W., 1915: Das Grundgesetz des Wärmeüberganges. *Gesundheits-Ing.*, **38**, 477–482, 490–496.

Obukhov, A. M., 1949: The structure of the temperature field in a turbulent flow. *Izv. Akad Nauk SSSR, Ser. Geogr. i Geofiz.*, **13**, 58–69.

Roberts, M. J., 2008: *Fundamentals of signals and systems*. McGraw-Hill, Boston, Massachusetts, 759 pp.

Roddier, F., 1981: The effects of atmospheric turbulence in optical astronomy. *Prog. Opt.*, **19**, 281–376.

Roddier, F., (Ed.) , 1999: *Adaptive optics in astronomy*. Cambridge University Press, Cambridge, United Kingdom, 411 pp.

Roggemann, M. C. and B. M. Welsh, 1996: *Imaging through turbulence*. CRC Press, Boca Raton, Florida, 320 pp.

Sasiela, R. J., 2007: *Electromagnetic wave propagation in turbulence*. 2d ed., SPIE Press, Bellingham, Washington, USA, 367 pp.

Schmidt, J. D., 2010: *Numerical simulation of optical wave propagation*. SPIE Press, Bellingham, Washington, 196 pp.

Strohbehn, J. W., 1968: Line-of-sight wave propagation through the turbulent atmosphere. *Proc. IEEE*, **56**, 1301–1318.

Strohbehn, J. W., (Ed.) , 1978: *Laser beam propagation in the atmosphere*, Topics in Applied Physics, Vol. 25. Springer, Berlin, 325 pp.

Tatarskii, V. I., 1961: *Wave propagation in a turbulent medium*. McGraw-Hill, New York, 285 pp.

Tatarskii, V. I., 1971: *The effects of the turbulent atmosphere on wave propagation*. Israel Program for Scientific Translation, Jerusalem, Israel, 472 pp.

Tichkule, S. and A. Muschinski, 2012: Optical anemometry based on the temporal cross-correlation of angle-of-arrival fluctuations obtained from spatially separated light sources. *Appl. Opt.*, **51**, 5272–5282.

Tichkule, S. and A. Muschinski, 2014: Effects of wind-driven telescope vibrations on measurements of turbulent angle-of-arrival fluctuations. *Appl. Opt.*, **53**, 4651–4660.

Uscinski, B. J., 1977: *The elements of wave propagation in random media*. McGraw-Hill, New York, 153 pp.

Uscinski, B. U., (Ed.) , 1986: *Wave propagation and scattering*. Clarendon Press, Oxford, United Kingdom, 381 pp.

Voelz, D. G., 2011: *Computational Fourier optics*. SPIE Press, Bellingham, Washington, 232 pp.

Voelz, D. G., E. Wijerathna, A. Muschinski, and X. Xiao, 2018: Computer simulations of optical turbulence in the weak- and strong-scattering regime: angle-of-arrival fluctuations obtained from ray optics and wave optics. *Opt. Eng.*, **57**, 104 102.

Welch, P. D., 1967: The use of Fast Fourier Transform for the estimation of power spectra: A method based on time averaging over short modified periodograms. *IEEE Trans. Audio and Electroacoustics*, **AU-15**, 70–73.

Wheelon, A. D., 2001: *Electromagnetic scintillation — I. Geometrical optics*. Cambridge University Press, Cambridge, United Kingdom, 455 pp.

Wheelon, A. D., 2003: *Electromagnetic scintillation — II. Weak scattering*. Cambridge University Press, Cambridge, United Kingdom, 440 pp.

Williams, R. M. and C. A. Paulson, 1977: Microscale temperature and velocity spectra in the atmospheric boundary layer. *J. Fluid Mech.*, **83**, 547–567.

Wyngaard, J. C., 1971: The effect of velocity sensitivity on temperature derivative statistics in isotropic turbulence. *J. Fluid Mech.*, **48**, 763–769.

Wyngaard, J. C., 1973: On surface layer turbulence. *Workshop on micrometeorology*, D. A. Haugen, Ed., Amer. Meteor. Soc., Boston, 101–149.

Wyngaard, J. C., Y. Izumi, and S. A. Collins, 1971: Refractive-index structure parameter near the ground. *J. Opt. Soc. Am.*, **61**, 1646–1650.

Yaglom, A. M., 1952: Introduction to the theory of stationary random functions. *Uspekhi Mat. Nauk*, **7**, 3–168.

Yaglom, A. M., 1962: *An introduction to the theory of stationary random functions*. Prentice-Hall, Englewood Cliffs, New Jersey, 235 pp.

Ziemer, R. E., W. H. Tranter, and D. R. Fannin, 1993: *Signals and systems: continuous and discrete*. 3d ed., Macmillan Publishing Company, New York, New York, 624 pp.

2.2 Computer simulations

2.2.1 Overview of computer simulations

The primary tool we utilized for the computer simulations is the split-step wave optics method. In this approach the propagation path is divided into segments where a phase screen that models the effect of turbulence is placed in each segment. Propagation of light between the screens is typically based on a numerical implementation of scalar diffraction theory. Light sources can be simple waves like plane or spherical waves, or more complex objects like resolution targets or image scenes. The receiving side can be modeled as a simple plane for mapping the incident intensity or some type of collection system such as a lens or telescope and focal (image) plane. Statistical values (e.g., mean, variance) of the received intensity can be estimated by repeating the numerical propagations many times (e.g., 10^4 times) through random turbulence realizations.

We applied the split-step method in various numerical simulations to investigate six topic areas. The first topic is an exploration of the applicability of ray modeling for different aspects of optical propagation and imaging. Ray modeling and analysis can significantly simplify theoretical and computational studies, but the geometrical (ray) assumption has limitations. In a second study, we investigated the applicability of the theoretical expression for the Fried parameter in strong turbulence conditions. The Fried parameter is universally applied in the design of optical systems that operate through turbulence. A third study was performed to investigate discrepancies between simulation results and theoretical models for scintillation owing to turbulence. Scintillation refers to a random fluctuation of intensity which is a problematic for many optical applications. Wavefront tilt modeling is the topic of our fourth effort and here we analyzed a simple method for correcting a low spatial frequency issue with the phase screens that are used in the split step method. This work is useful for other researchers using the split step approach. The fifth effort is the development of a new simulation approach based on the split step method for simulating the light propagating through turbulence from targets of large angular subtense. This is a particularly difficult problem for a split-step wave optics simulation. Finally, other specific numerical simulations were conducted to support various experimental and theoretical efforts within the program.

2.2.2 Geometrical (ray) and wave optics modeling and applications

It is known that geometrical-optics predictions often agree well with optical turbulence field observations even though theoretical constraints for ignoring wave diffraction may be violated. Geometrical optics assumptions can simplify analyses and ray optics can significantly reduce simulation computation time. In fact, considerable theoretical effort has been devoted to establishing criteria for the negligibility of diffraction effects (Tatarskii, 1961; Wheelon, 2001; Fried, 1966a). We conducted simulation studies to explore the applicability of ray and wave optics modeling for different aspects of optical propagation and imaging.

A novel investigation of angle-of-arrival (AOA) fluctuations was completed involving wave and ray optic simulations of a plane wave propagating through a turbulent refractive-index field (Voelz et al. 2018). We found (Fig. A) that simulated and Rytov-based theory results for the variances of aperture-filtered AOA fluctuations $\langle \bar{\theta}^2 \rangle$ generally agree well for weak turbulent scattering (Rytov variance, $\sigma_R^2 \lesssim 0.2$) but for stronger turbulent scattering conditions (e.g., Rytov variance, $\sigma_R^2 \geq 2.67$) the simulation results exhibit lower AOA variance values than predicted by the theory. This over-prediction of the AOA fluctuations by the Rytov theory is likely a result of the failure of the Rytov approximation in the strong-scattering regime. We also found that the ray and wave results agree well for larger normalized apertures ($q > 10$). For smaller apertures, the wave simulation variances are smaller than those produced by the ray simulations, and we attribute this to a "Fresnel filtering" effect associated with diffraction. The results of this study provide new insights on the applicability of ray optics and Rytov-based theory for analysis of wavefront characteristics.

The split-step wave optics simulation approach has been used extensively to study scintillation, beam size, wavefront discontinuities and other properties of optical beams propagating through atmospheric turbulence, see for example Lachinova and Vorontsov (2016) and Xiao and Voelz, (2009). New simulation work completed under this project (Voelz et. al, 2018) was motivated by the questions: 1) What is the behavior of the wave optics simulation approach when applied to incoherent imaging in turbulence for the focus (peak scintillation) regime and the strong (saturation) scintillation regime, and 2) Can ray tracing combined with split-step phase

screens be used for simulating incoherent imaging in these regimes? Fig. B shows wave optics and ray optics image simulation results for C_n^2=10^{-16} to 10^{-13}, corresponding to values of the Rytov variance ranging from 0.027 and 0.27 (weak regime), to 2.7 (focus regime) and 27 (saturation regime). We find that the ray tracing results provide a recognizable approximation to the wave optics results even in the saturation regime, although with some loss of high spatial frequency content. Further analysis completed for this project indicates that a more accurate accounting of the mutual coherence function related to the receiver aperture provides a better match between the wave and ray results.

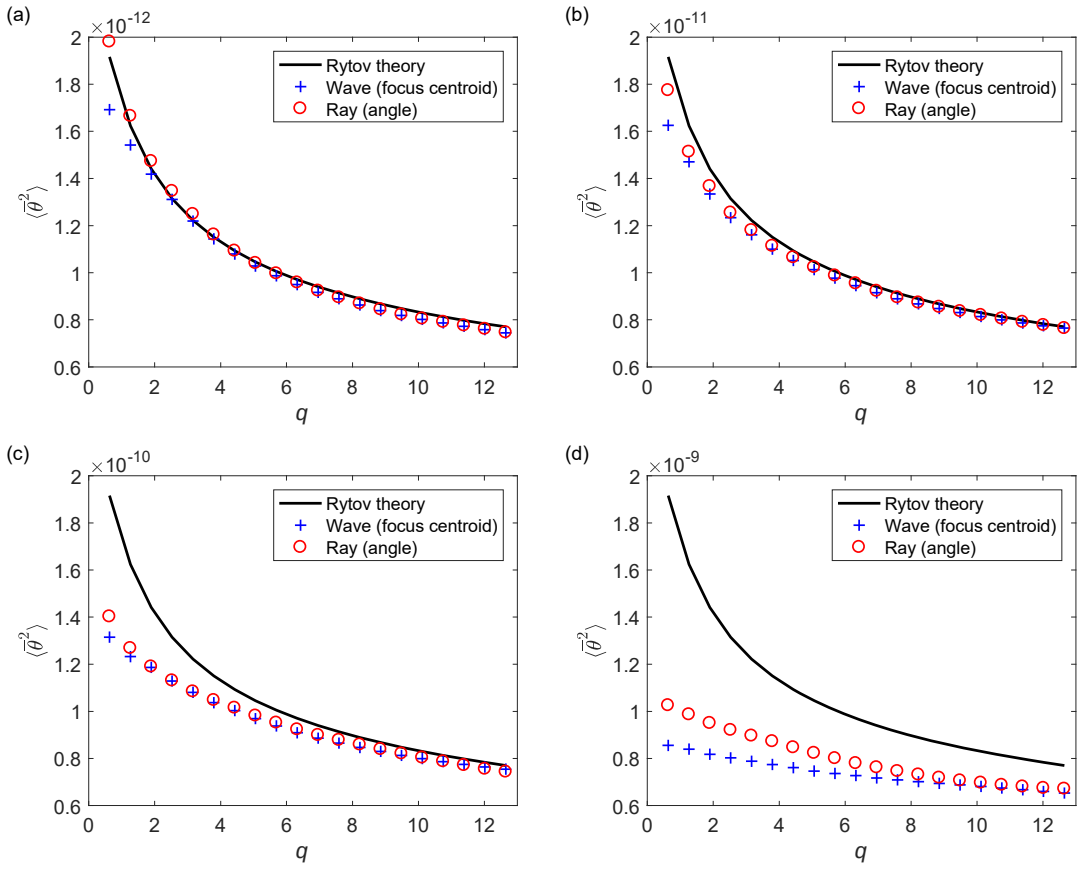

Figure A: *Aperture-averaged AOA simulation results and Rytov-based theory as a function of normalized aperture size q: (a)* $\sigma_R^2 = 0.0267$, $C_n^2 = 10^{-16}$ *m*$^{-2/3}$, *(b)* $\sigma_R^2 = 0.267$, $C_n^2 = 10^{-15}$ *m*$^{-2/3}$, *(c)* $\sigma_R^2 = 2.67$, $C_n^2 = 10^{-14}$ *m*$^{-2/3}$, *(d)* $\sigma_R^2 = 26.7$, $C_n^2 = 10^{-13}$ *m*$^{-2/3}$.

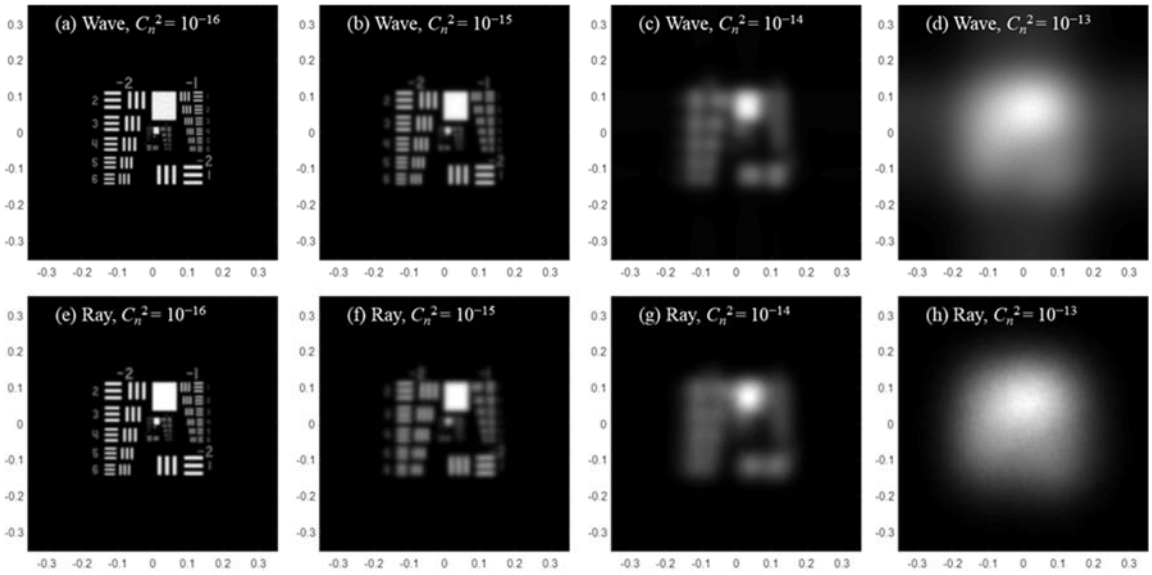

Figure B: *Results of long-exposure incoherent imaging of an extended object using wave (top row) and ray (bottom row) optics simulations, for $\lambda = 0.5$ μm, L = 2 km and receiver aperture diameter 0.35 m.*

2.2.3 Fried parameter analyses

The Fried parameter (r_0) is a fundamental coherence length measure that characterizes the spatial resolution effects of atmospheric turbulence on imaging and beam propagation. It is universally applied in the design of optical imaging and beam projection systems that operate through turbulence. The analytic expression for r_0 was originally derived with a geometrical optics approximation that neglects diffraction effects and assumes no significant bending of the rays (Fried, 1966a; Fried 1966b; Fried 1967). This suggests the Fried parameter formulation would only be strictly valid in the weak turbulent scattering regime, however, the actual range of validity has remained controversial. Several simulation studies were accomplished during this project that explored the accuracy of the Fried parameter in strong turbulent fluctuation conditions and the form of r_0 for a non-Kolmogorov spectral model for turbulence.

In a study of the long-exposure r_0, we applied a split-step wave optics simulation to answer the question "Is the formulation of r_0 accurate in the strong turbulent scattering regime?" (Zhan et al., 2020; Zhan et al., 2019). Results were generated assuming both plane wave and spherical wave sources for different receiving aperture diameters and Kolmogorov turbulence. The results presented in Figure C show that the classical expressions for r_0, for both spherical and plane waves in Kolmogorov turbulence, are valid throughout the weak ($\sigma_r < 1$) to strong ($\sigma_r \gtrsim 3$) scattering regimes. This work advances our understanding of the combined effects of phase and amplitude variations caused by turbulence and supports the use of r_0 as an optical system design parameter even in strong turbulent scattering conditions.

In a related study, we developed a simulation to study r_0 when the turbulence spectrum is described by the von-Kármán-Tatarski spectral model, which is a more realistic model that includes a finite outer scale (L_0) and a non-zero inner scale (l_0). Note for the Kolmogorov model, $l_0 \to 0$ and $L_0 \to \infty$. Along with the simulation work, we developed a theoretical expression for r_0 as a function of l_0 and L_0. Figure D show r_0 results as a function of σ_r for several parameter sets and plane and spherical waves. The simulation results agree well with the corresponding theory values in all cases. Our conclusion from this work is that neglecting the inner and outer scales when calculating r_0 can result in 10% to 30% discrepancies for strong turbulent scattering and a relatively small outer scale (e.g., $L_0 = 5$ m results in Fig. D).

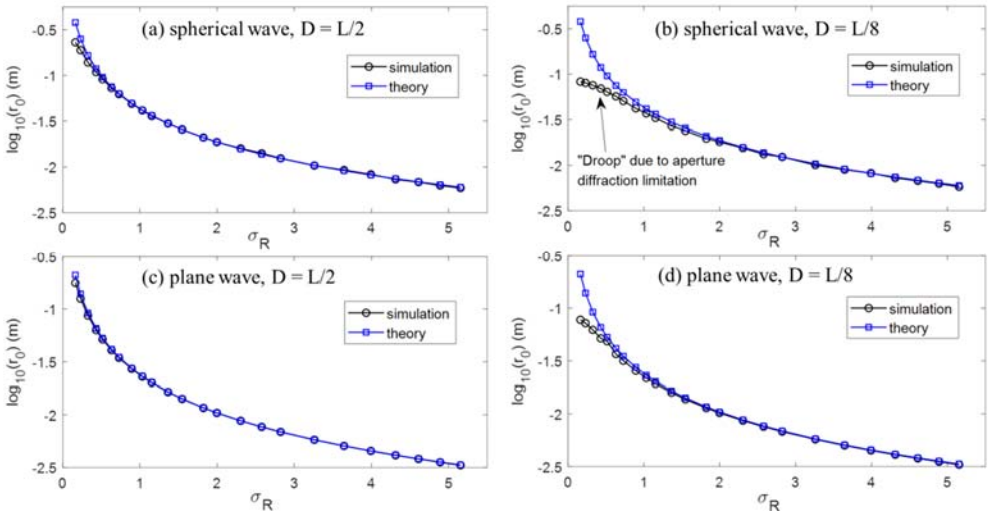

Figure C: *Simulation and theory results for the Fried parameter r_0 as a function of the Rytov standard deviation assuming the Kolmogorov spectral model. D is the aperture diameter, L = 0.707 m is the grid width and propagation distance is 2 km.*

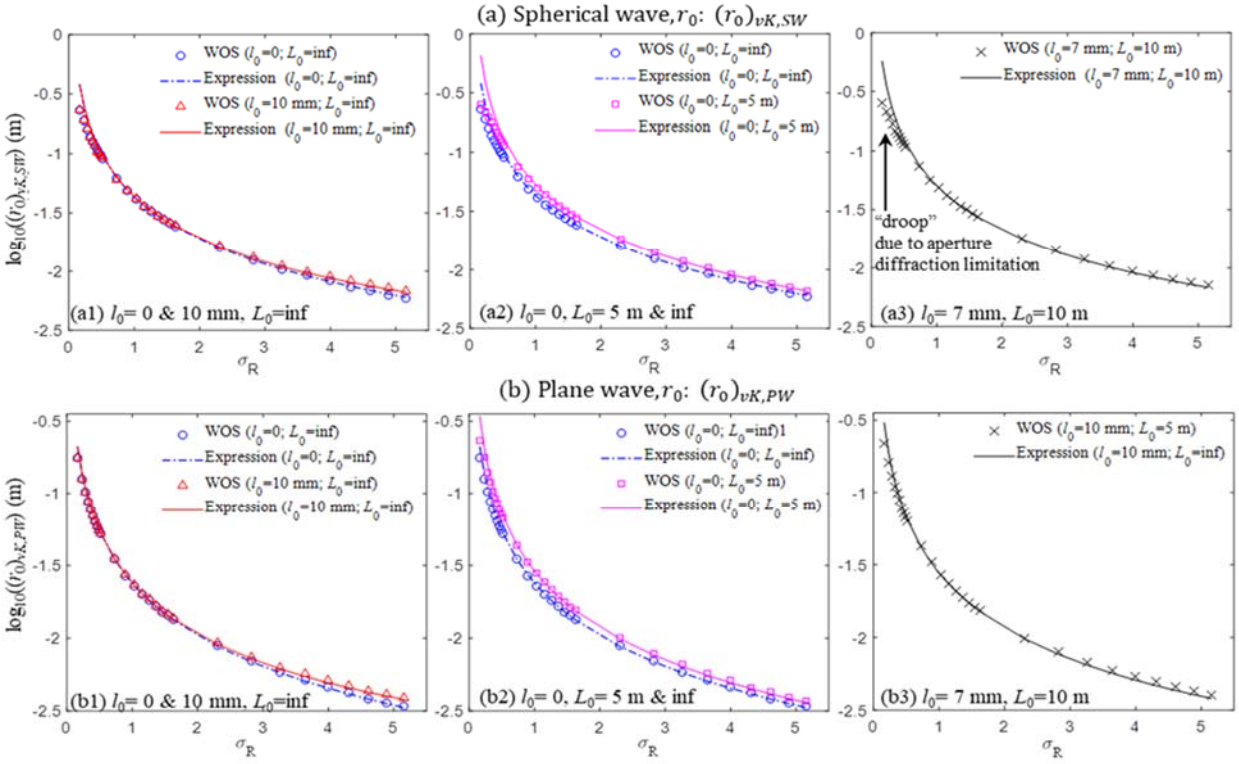

Figure D: *Simulation (WOS) and theory (Expression) results for the Fried parameter r_0 as a function of the Rytov standard deviation. Simulation results assume the von Kármán-Tatarski spectral model.*

2.2.4 Scintillation studies

The scintillation index (σ_I^2) is the normalized variance of irradiance (intensity) fluctuations and is an important metric for optical system performance in the presence of atmospheric turbulence. The phenomenon of scintillation (Hill and Clifford, 1981; Andrews and Phillips, 2005; Lachinova and Vorontsov, 2016) poses considerable problems for optical applications such as free space communication and directed energy beam projection. Over the last 50 years, considerable effort has been focused on the development of analytical models that describe σ_I^2 for a range of optical beams or waves and turbulence conditions. However, several recent

publications (e.g., Lachinova and Vorontsov, 2016) show that σ_I^2 results generated from wave optics simulations can differ appreciably from the predictions of existing analytic models in the moderate to strong turbulence fluctuation regimes where the Rytov variance $\sigma_R^2 > 1$.

For this project we developed a split-step wave optics simulation to study scintillation as a function of turbulence scattering strength parameterized here by the square root of the Rytov variance (Wijerathna, 2021; Wijerathna et al., 2018; Wijerathna et al., 2019). The Kolmogorov, von Kármán-Tatarski (finite inner and outer scales) and Hill spectra for turbulence were modeled. We assumed a point measurement (no aperture averaging) and compared our scintillation results with those for several influential works from the literature (Table 1).

Table 1. Experimental, simulation and theoretical scintillation for comparison.

Year	Authors	Approach	Quantity	Wave	Spectrum	Scales
1981	Hill and Clifford	Theory and Experiment	σ_χ^2	Spherical	Any	l_0
1993	Flatté *et. al.*	Simulation	σ_I^2	Plane wave, Spherical wave	Hill	l_0
2005	Andrews and Phillips	Theory	σ_I^2	Plane wave, Spherical wave, Gaussian beam	Effective atmospheric spectra	l_0, L_0

As an example, Figure E shows two comparisons. Note that in Fig. E(b), the scintillation index is described by the variance of the log amplitude of the intensity, which is a measure that was used in early scintillation studies. The discrepancies apparent in Fig. E are significant, particularly for stronger turbulence fluctuation conditions.

Brief conclusions of this work are that significant discrepancies were found between our simulation results and the theoretical models of Hill & Clifford and Andrews & Phillips for most of the propagation scenarios we examined. The sources of the discrepancies are not clear because applying our simulation to scenarios published by Flatté produced good consistency between the two simulation results. It is hoped that this study can shed light on issues in experimental and theoretical studies of atmospheric scintillation in strong fluctuation conditions and lead to improved developments in the future.

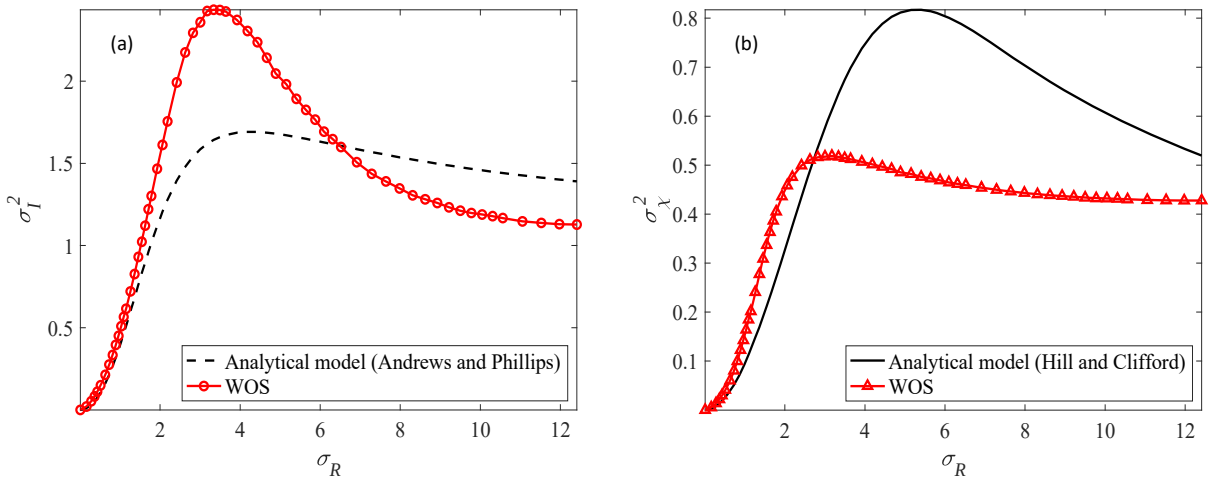

Figure E: *In the absence of an inner scale ($l_0 = 0$) and infinite outer scale ($L_0 = \infty$) (a) Scintillation index (σ_I^2) and (b) variance of the log amplitude index (σ_χ^2), as a function of scattering strength represented by the Rytov standard deviation (σ_R).*

2.2.5 Wavefront tilt modeling developments

An optical wavefront propagating through atmospheric turbulence may be affected by associated low spatial frequency components that can redirect the energy. The makeup of these low frequencies is a function of the outer scale L_0, described in section 2.2.3. The energy redirection (tip-tilt) effect can manifest as "image wander" for an imaging system or "beam wander" for a laser beam projection system and often represents a significant portion of the wavefront distortion that is created by turbulence. Therefore, it is important to accurately model the low wavenumber components in propagation simulations. In this project we examined several aspects of modeling tilt in wave optics simulation and evaluated the effects of tilt for different applications.

The FFT-based filtering method we use for turbulence phase screen generation in our wave optics simulations is a popular technique; however, these screens inherently underrepresent the spectral density at low wavenumbers. One of our efforts was to explore a "Z-tilt" approach to augment or compensate the spectral density at low wavenumbers by adding a random phase tilt to FFT-based screens (Wijerathna et al. 2022). The Z-tilt random phase screen is derived from the turbulence wavefront phase statistics with a Zernike polynomial basis. Our technical contributions include a derivation of the Z-tilt screen coefficients for the von-Kármán spectrum with finite outer scale, an examination of the structure functions of the phase screens derived with the Z-tilt approach, and a comparison of the results with a common subharmonic compensation method.

Figure F shows an example of the normalized mean square error of the phase structure function for the various screens as a function of outer scale L_0. The screen represents a physical size of $L \times L$, where $L = 3$ m. Other details of the simulation can be found in Wijerathna et al. 2022. The screen with Z-tilt compensation ϕ_{FZ} shows the lowest structure function error for large L_0 (right side of Fig. F). The uncompensated screen ϕ_F slows the most error for large L_0. As the outer scale becomes shorter, there is a reversal near $L_0 \approx 3$ m where an alternative form of the Z-tilt screen $\phi_{F'Z}$ and the subharmonic screen ϕ_{FSH} give the lowest error. For $L_0 \approx L$, all the methods give similar performance except ϕ_{FZ}, due to the excess compensation. The uncompensated FFT screen demonstrates the least error when $L_0 < L$.

This study showed that the additive Z-tilt method is a simple, efficient, and accurate approach to compensate FFT-based turbulence phase screens for outer scales larger than about 3 times the physical width represented by the screen. In addition, the elapsed time to compute a Z-tilt screens is typically two orders of magnitude shorter than computing a subharmonic screen.

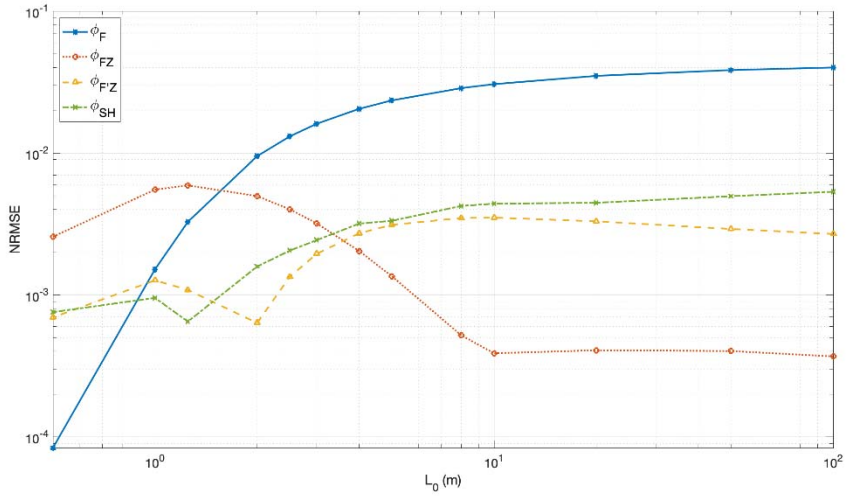

Figure F: *Normalized Root Mean Square Error (NRMSE) of the radially averaged structure function for four types of phase screens as a function of* L_0.

A second study involves two tilt definitions that show up when describing short-exposure imaging through turbulence (Zhan et al., 2021). In the mid-1960s, Fried published a series of papers on a theoretical foundation

for the effect of atmospheric turbulence on the average optical resolution of long-exposure (LE) and short-exposure (SE) images (Fried, 1965; Fried, 1966a). The SE theoretical development differs from the LE in that the instantaneous phase tilt over the system aperture is removed. However, two phase tilt definitions have been applied in the literature for this purpose: Z-tilt and G-tilt. The Z-tilt is the normal to a least-square fit to the Zernike polynomial tip-tilt terms whereas G-tilt is the direction normal to the average of all the local gradients of the wavefront over the pupil. It is commonly assumed that G-tilt is consistent with image centroid displacement in the focal plane. For the study we developed a split-step wave optics simulation to simulate the propagation of the field from a point source through atmospheric turbulence and examined the width of the resulting instantaneous point spread function. Our conclusion from this study is that the Z-tilt definition provides results that are consistent with Fried's short-exposure theory. However, applying the G-tilt definition produces narrower point spread functions that can deviate significantly from Fried's far-field theory.

2.2.6 Simulation technique for targets of large angular subtense

A particularly difficult problem for a split-step wave optics simulation is to model the propagation of light from a target that subtends more than several milliradians. The issue is two-fold in that the number of samples across the screens or target can become unmanageable and violating geometrical constraints for the numerical propagators results in artifacts (Voelz, 2011; Schmidt, 2010). We developed a new split-step simulation approach that works well for certain situations with targets of large angular subtense. We demonstrated the method in modeling the phenomena of "shadow bands" which are thin, wavy ribbons of light that are seen moving and undulating on the ground just preceding and following the occurrence of a total solar eclipse (Codona, 1986). These intensity patterns are a result of the light propagating through atmospheric turbulence as the solar crescent thins to a narrow filament.

Figure G illustrates the concept of the simulation approach as applied to the shadow bands problem. Consider vectors from the point radiators at the source (solar crescent) to the center of the observation area on the ground. The vectors intersect the highest turbulence screen (Fig. G, screen 6) within an area that is a de-magnified version of the crescent source shape. The placement of the highest screen at 3 km altitude was based on conclusions from Codona. We consider an even distribution of these vectors that are relatively closely spaced and place a small plane wave at each intersection that is centered on and normal to the corresponding vector. Thus, a mosaic of small, overlapping plane wave components is created in the de-magnified form of the crescent shape at the highest screen. The size of the crescent at the highest screen is found by projecting the angular size of the crescent as seen from the ground to the screen. Each plane wave component is then numerically propagated to the observation area on the ground. Because the sun essentially emits incoherent light, we can sum the resulting intensity patterns for each plane wave component to get the total pattern on the ground. An example result from the simulation is shown on the right side of Fig. G.

We were able to model results for different wavelengths and implement wind effects by translating the screens, which provides an emulation of the temporal behavior of the bands. Quantitative values extracted from the simulation results were found to be consistent with actual measurements during an eclipse and the theory provided by Codona. Beyond the shadow band application, the general concept of the simulation approach is easily adaptable and can be applied to scintillation and imaging problems involving other incoherent objects or sources that subtend relatively large angles and are observed through atmospheric turbulence.

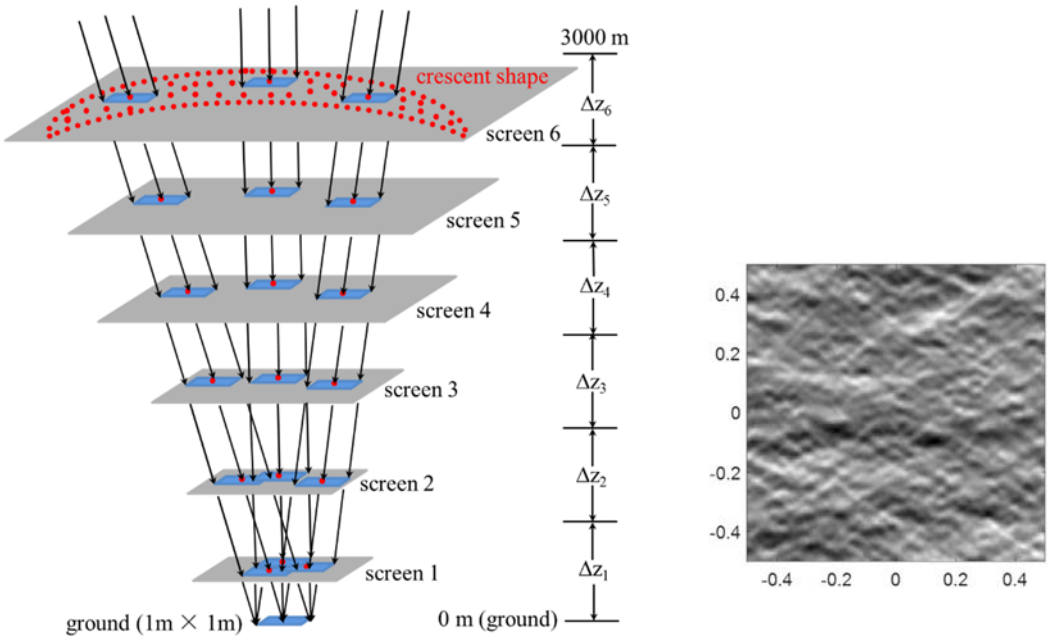

Figure G: *Left side: arrangement of source and turbulence screens for the wave optics simulation. The red dots indicate centers of individual wave components shown in blue. Right side: example of shadow bands intensity pattern produced by the simulation. The contrast for the pattern is only about 1.2% and has been enhanced for display.*

2.2.7 Experiment and theory support

Numerical simulations were also conducted to support other experiment and theoretical activities within this program. A few examples of these efforts are described in this section. To support measurements of the intensity fluctuations of starlight conducted in Boulder CO (Section 2.1.3), we simulated the images expected for a Meade telescope with a 14-inch (36 cm) aperture diameter and equipped with an astronomical digital camera. For this work, we propagated plane waves (equivalent of starlight approaching the Earth's atmosphere) through a single turbulence screen that corresponds to an atmospheric turbulence layer of a selected thickness and refractive index structure parameter C_n^2 as suggested by the actual experimental images. The simulated light collected by the telescope aperture was then numerically propagated to the focal plane. We examined focused and defocused images for different scenarios by varying the turbulence parameters and turbulence screen position. Figure H presents example results. The simulation data provided confidence in the actual measurements and helped our understanding of the character of this type of data.

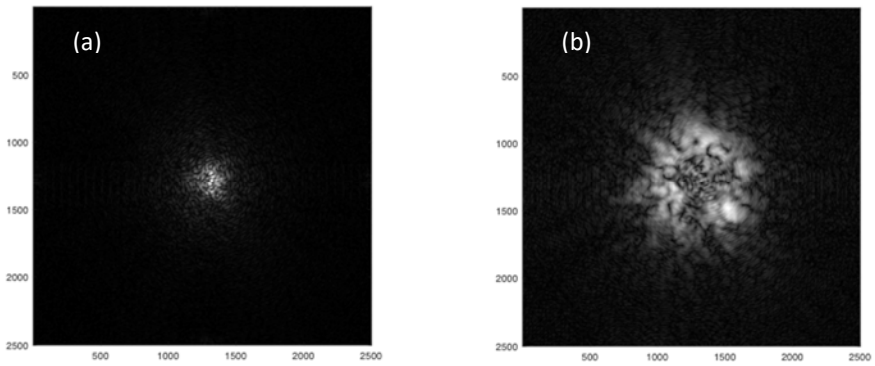

Figure H: *(a) focused and (b) defocused (by 0.05m) images at the focal plane of the telescope for starlight (λ=0.5 μm) propagated through 5km of atmosphere.*

A novel simulation was developed to support an investigation of the underlying statistics of random phase due to turbulence. The phase screens modeling turbulence in our wave optics simulations are created using an FFT method where a grid of random Gaussian distributed numbers (zero mean and unit variance) is filtered in the Fourier domain to be consistent with the required turbulence power spectral density. This means the point statistics and increment statistics (differences between the phase at separated points) of the resulting phase screens are Gaussian. However, there is evidence from in-situ observations (see Section 2.1.5) that the statistics of the refractive index increments are not Gaussian and have a PDF that appears like a double-sided exponential, similar to the Laplace distribution.

To explore the consequences of non-Gaussian underlying statistics, we developed a methodology for creating a phase screen where the underlying random distribution is such that the increments are Laplace distributed (double-sided exponential). A Gaussian-product approach was used to create the Laplace distributed random value draws. The initial array is filled with random numbers from the Laplace distribution and the array is filtered in the Fourier domain to conform to the turbulence spectrum. We examined the PDFs (histograms) of the phase increments of these screens and compared with screens created with Gaussian random numbers (Fig. I). For small separations *r* along the screen, there is a strong indication of the Laplace (double sided exponential) distribution in the wings of the PDF but the significance of this feature is reduced for larger increments.

Although the underlying statistics of the refractive index increments may be non-Gaussian, we presume that because the phase screen is created through an averaging process where the central limit theorem comes into play, the phase increments statistics move toward a Gaussian distribution for larger increments. It seems apparent that the translation of the non-Gaussianity of the underlying statistics to the non-Gaussianity of the phase increments depends on the number of dominant turbulent eddies that exist along the propagation path.

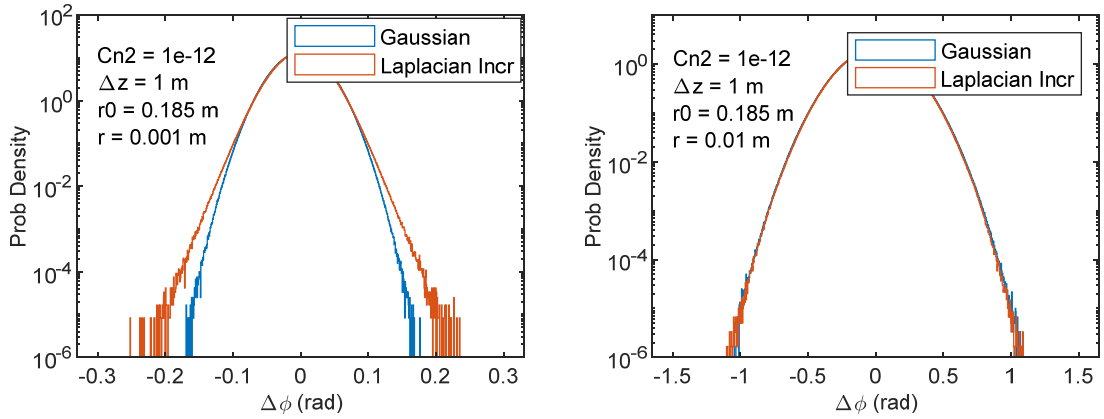

Figure I: *Phase increment PDFs (histograms) for Gaussian and Non-Gaussian (Laplacian increments) phase screens. Left – small increment (r = 0.001); right – larger increment (r = 0.01).*

Bibliography

Andrews, L. C., and R. L. Phillips, Laser Beam Propagation through Random Media, 2nd ed. (SPIE Press, 2005).

Codona, C., "The scintillation theory of eclipse shadow bands," Astronomy and Astrophysics 164, 415–427 (1986).

Fried, D. L., "Statistics of a Geometric Representation of Wavefront Distortion," J. Opt. Soc. Am. 55(11), 1427–1435 (1965).

Fried, D. L., "Optical resolution through a randomly inhomogeneous medium for very long and very short exposures," J. Opt. Soc. Am., 56, 1372–1379 (1966a).

Fried, D. L., "Propagation of an infinite Plane Wave in a Randomly Inhomogeneous Medium," J. Opt. Soc. Am. 56(12), 1667–1676 (1966b).

Fried, D. L., "Propagation of a Spherical Wave in a Turbulent Medium," J. Opt. Soc. Am. 57(2), 175–180 (1967).

Hill, R. J., and S. F. Clifford, "Theory of saturation of optical scintillation by strong turbulence for arbitrary refractive-index spectra," J. Opt. Soc. Am. 71, 675–686 (1981).

Lachinova, S. L., M. A. Vorontsov, "Giant irradiance spikes in laser beam propagation in volume turbulence : analysis and impact," J. Opt. 18, 25608 (2016).

Schmidt, J. D., Numerical Simulation of Optical Wave Propagation, pp.149-182, SPIE Press, Bellingham, Washington (2010).

Tatarskii, V. I., Wave Propagation in a Turbulent Medium, pp. 285, McGraw-Hill, New York (1961).

Voelz, D., Computational Fourier Optics: A MATLAB Tutorial, SPIE Tutorial Text TT89, SPIE Press, Bellingham, Washington (2011).

Voelz, D., H. Zhan, and E. Wijerathna, "Wave and Ray Optics Simulations of Short Exposure Incoherent Imaging in Atmospheric Turbulence," in Imaging and Applied Optics 2018 (3D, AO, AIO, COSI, DH, IS, LACSEA, LS&C, MATH, pcAOP), OSA Technical Digest (Optica Publishing Group), paper PTu2I.2 (2018)

Wheelon, A. D., Electromagnetic Scintillation I- Geometric Optics, pp. 455, Cambridge University Press, Cambridge, United Kingdom (2001).

Wijerathna, E., D. Voelz, and H. Zhan, "Discrepancies between Simulation and Theory Results for Plane Wave Scintillation in Atmospheric Turbulence," in Imaging and Applied Optics 2018 (3D, AO, AIO, COSI, DH, IS, LACSEA, LS&C, MATH, pcAOP), OSA Technical Digest (Optica Publishing Group, 2018), paper PTu2I.4.

Wijerathna, E., D. Voelz, A. Muschinski, and H. Zhan, "Spherical Wave Scintillation in Atmospheric Turbulence: A Comparison of Analytical Models and Simulation Results," in Imaging and Applied Optics 2019 (COSI, IS, MATH, pcAOP), OSA Technical Digest (Optica Publishing Group), paper PM1C.4. (2019)

Wijerathna, E. A., Numerical Wave Optics Simulations through Atmospheric Turbulence: Simulation Method Improvements and a Comparative Study of Optical Scintillation, PhD dissertation, New Mexico State University, Elec. and Comp. Engr., ProQuest Dissertations Publishing, 2021.

Wijerathna, E., H. Zhan, D. Voelz and A. Muschinski, "Low-wavenumber compensation with Zernike tilt for non-Kolmogorov turbulence phase screens," accepted for publication in Appl. Opt., December 2022.

Xiao, X., D. Voelz, "On-axis probability density function and fade behavior of partially coherent beams propagating through turbulence," Appl. Opt. 48, 167-175 (2009).

Zhan, H., E. Wijerathna, and D. Voelz, "Wave Optics Simulation Studies of the Fried Parameter for Weak to Strong Atmospheric Turbulent Fluctuations," in Imaging and Applied Optics 2019 (COSI, IS, MATH, pcAOP), OSA Technical Digest (Optica Publishing Group), paper PM1C.3, (2019).

Zhan, H., E. Wijerathna, and D. Voelz, "Is the formulation of the Fried parameter accurate in the strong turbulent scattering regime?," OSA Continuum 3, 2653-2659 (2020)

Zhan, H., E. Wijerathna, D. Voelz, and A. Muschinski, "Short-exposure image resolution: Tilt definition study," in OSA Imaging and Applied Optics Congress 2021 (3D, COSI, DH, ISA, pcAOP), (Optica Publishing Group), paper PTu4C.3 (2021)

Zhan, H., and D. G. Voelz, "Modeling solar eclipse shadow bands using wave optics simulation through distributed turbulence," Appl. Opt. 60, 8426-8434 (2021)

3 Impacts

3.1 Impact on the principal disciplines of the project

We have investigated various characteristics of wave propagation through the turbulent atmosphere by means of observations (using optical sensors and in-situ sensors such as ultrasonic anemometer-thermometers, fine-wire thermometers, and microbarometers), theoretical analysis, and computer simulations.

Our in-situ measurements show no compelling evidence of the existence of "non-Kolmogorov turbulence" in the atmospheric surface layer. With "non-Kolmogorov turbulence," we denote turbulent temperature fluctuations characterized by an inertial-convective range 3D temperature spectrum that follows a power law that differs from the classical $\kappa^{-11/3}$ power law predicted by the Obukhov-Corrsin theory (Obukhov, 1949; Corrsin, 1951; Tatarskii, 1961). Even in the stably stratified atmospheric surface layer close to the ground, both ultrasonic anemometers and fine-wire thermometers reveal robust, fully developed "Kolmogorov turbulence".

While our in-situ observations do not support the popular belief that atmospheric turbulence is often "non-Kolmogorov," they do provide incontrovertible evidence that turbulent temperature increments are strongly non-Gaussian, typically two-sided exponential. To what extent the central limit theorem "converts" the non-Gaussian temperature increments to Gaussian phase increments (a standard assumption in the physics of optical turbulence) depends on the number of statistically independent phase screens along the propagation path. This number is generally large for propagation over long horizonal paths but it may be very small (on the order of 1) for vertical or slanted propagation paths if the turbulence is concentrated within a single turbulent layer.

"Deep turbulence", which refers to conditions of strong turbulent fluctuations, has recently been a priority research topic for directed energy applications. System analysis for these conditions is hampered because the applicability of the available theory is either invalid or unknown. Our simulation results demonstrate that the Fried parameter is a robust characterization of the spatial correlation of the optical wavefront even under strong fluctuation conditions whereas available analytical models for scintillation assuming point receivers show significant deviations from the simulation results.

We introduced several novel developments related to computational wave optics simulations that should be of considerable utility for other researchers investigating atmospheric turbulence and free space optical systems. Along with other advancements, we incorporated rays within the wave simulation to investigate the applicability of geometrical approximations, we validated a simple and effective method for accurately portraying low wavenumbers in turbulent phase screens, and we developed a method to model targets of large angular extent.

3.2 Impact on other disciplines

The physics of optical turbulence plays an important role for various science and engineering disciplines in the civilian and military arenas, such as optical remote sensing, free-space optical communication, optical imaging of terrestrial and extraterrestrial objects and adaptive optics, as well as target-acquisition, beam-control and directed-energy technologies. The concepts, theoretical models, model assumptions, and the observational and computational tools and techniques that were applied and investigated in this project are of critical importance for the design and operation of a wide variety of systems used by researchers and engineers working in these disciplines.

3.3 Impact on the development of human resources

This project provided financial and intellectual support for various graduate and undergraduate students, some of which have found employment in aerospace engineering and related fields.

During the lifetime of this project, four undergraduate students earned their Batchelor degrees at the University of Colorado Boulder: Ryan Schaetzle in physics, Carter Mak and Nathan Kuczun in aerospace engineering, and Maxwell Anderson in mechanical engineering. Now, Ryan Schaetzle works in quality control at Ball Aerospace, Boulder, CO; Carter Mak develops software for satellite simulations at the NASA Jet Propulsion Laboratory, Pasadena, CA; Nathan Kuczun is a systems engineer at Freefly Systems, Woodinville, WA; and Maxwell Anderson has entered CU's Mechanical Engineering graduate program.

Erandi Wijerathna received her PhD in Electrical Engineering at NMSU, Las Cruces, NM partway through this project. She continued supporting the final year of the project as a postdoctoral scholar and is now a postdoctoral researcher for a project sponsored by the Intelligence Advanced Research Projects Activity (IARPA) involving imaging through turbulence. Andrea Baca was recruited for this project and entered the Master's program in Electrical Engineering at NMSU. She is now in her second year of the program.

3.4 Impact on teaching and educational experiences

Specific concepts and tools developed in this project were introduced into several graduate classes at NMSU. These classes included "Fourier Methods in Electro-Optics" where some of the wave optics simulations developments were presented, "Statistical Optics" where new understanding related to turbulence theory was discussed, and "Optical System Design" where, for example, the optical design for the light sources used in the long-range optical propagation experiment at White Sands Missile Range was assigned as a final project.

Weekly meetings of the optics research group led by Dr. Voelz at NMSU allowed students working on other activities to learn about this project. For example, the project provided an opportunity for undergraduate students in the group to observe the work and assist on occasion. For example, several students learned how to configure the light sources and operate camera systems for the long-range optical propagation experiment. The undergraduate students were also helpful in running some of the simulation codes and organizing data.

3.5 Impact on physical, institutional, and information resources that form infrastructure

During the lifetime of this project, the NWRA team integrated and refined optical and in-situ sensors and sensing techniques. A unique fine-wire turbulence measurement system was developed in-house *ab initio*. All these sensors are portable and will be available for future field experiments, even in remote locations "off the grid".

Computer simulation codes and computational tools developed for this project are applicable in many other problems involving laser propagation and imaging through turbulence. The introduction of the new long-range optical propagation test area across White Sands Missile Range near NMSU provides a unique capability for optical propagation and atmospheric testing in the future.

4 Attachment

1. Proof of Muschinski and Wagner (2023), which is in press, to appear in *Waves in Complex and Random Media as part* of the upcoming *Special Issue in honour of V.I. Tatarskii (1929-2020)*.

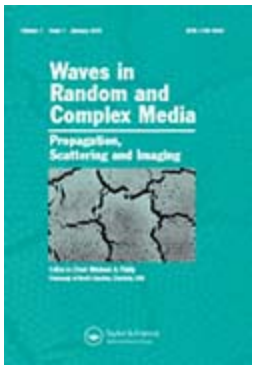

First field measurements of optical turbulence near the ground with a newly developed fine-wire thermometer

Journal:	*Waves in Random and Complex Media*
Manuscript ID	TWRM-2021-1445.R1
Manuscript Type:	Special Issue Paper
Keywords:	Optical turbulence, Fine-wire thermometry, Wave propagation, Viscous-diffusive subrange, Hill bump

SPECIAL ISSUE PAPER

First field measurements of optical turbulence near the ground with a newly developed fine-wire thermometer

Andreas Muschinski[a,b] and Eric L. Wagner[a]

[a]NorthWest Research Associates, Inc., 3380 Mitchell Lane, Boulder, Colorado 80301, USA; [b]Ann and H. J. Smead Aerospace Engineering Sciences, University of Colorado Boulder, 3775 Discovery Drive, Boulder, Colorado 80303, USA

ARTICLE HISTORY
Compiled April 11, 2022

ABSTRACT
First results of optical turbulence field measurements collected with a newly developed fine-wire temperature sensing system are presented and discussed. The centerpiece of the sensing system is an array of fine-wire platinum resistance thermometers. The active fine wire in each sensor element has a diameter of 0.64 μm and a length between 0.5 mm and 1 mm. The sampling rate is 44.1 kHz, and the noise level is 1 mK for a bandwidth of 10 kHz. Data were recorded while the car onto which the sensors were mounted was travelling at a speed of about 40 mph, or 18 $\mathrm{m\,s^{-1}}$. Estimates of the temperature structure function $D_{\theta\theta}(r)$ are compared against the classical Obukhov-Corrsin theory, which predicts r^{α} power-law asymptotes with $\alpha = 2$ in the viscous-diffusive range and $\alpha = 2/3$ in the inertial-convective range. For the pair of separations $r_1 = 5$ cm and $r_2 = 10$ cm, we observed $\alpha = 0.63 \pm 0.06$. The frequency spectrum $S_{\theta\theta}(f)$ follows the theoretically predicted $f^{-5/3}$ power law in the inertial-convective subrange. The "Hill bump" in the transition regime between the inertial-convective and viscous-diffusive subranges is visible.

KEYWORDS
Optical turbulence; fine-wire thermometry; wave propagation; viscous-diffusive subrange; Hill bump.

1. Introduction

The modern physics of wave propagation through the turbulent atmosphere was pioneered by Obukhov, Yaglom, Tatarskii and coworkers in the former Soviet Union in the 1950s and 1960s, as is documented in Tatarskii's two seminal monographs [1,2]. Tatarskii's main achievement was the integration of Obukhov's theory of scalar turbulence [3], Yaglom's mathematical theory of stochastic processes and random fields [4,5], and Maxwell's electromagnetic field theory into a comprehensive theory of wave propagation through turbulent media. As pointed out by Monin and Yaglom [6, p. 496], however, Tatarskii also conducted ground-breaking observational research: "The most detailed measurements of the spatial structure function $D_{\theta\theta}(r)$ in the surface layer of the atmosphere (at heights of 1.5, 16, and 22 m, and r varying between 3 and 100 cm) were carried out by Tatarskii (1956) using two resistance thermometers and a special squaring device which automatically gives the mean square of the temperature

CONTACT Andreas Muschinski. Email: andreas@nwra.com

difference at two points. Using the approximation $D_{\theta\theta}(r) \sim r^{\alpha}$, Tatarskii found a mean value of 0.81 for α (with relatively large spread of the individual values) which is close to the theoretical result $\alpha = 2/3 \approx 0.67$."

During the last 70 years since the publication of Obukhov's [3] and Corrsin's [7] theoretical papers on the spatial statistics of temperature fluctuations in fully developed turbulence, steady and significant progress has been made on this topic with respect to theoretical analysis [6,8–10], sensor development [11,12], field measurement [9,11,13], and computer simulation [14,15].

The purpose of the present paper is twofold: first, to demonstrate the usefulness of a newly developed fine-wire thermometer system for high-resolution turbulence measurements in the open atmosphere; second, to compare the measurements against theoretical predictions.

The paper is organized as follows. Section 2 summarizes the main results of the Obukhov-Corrsin theory. Section 3 gives a brief description of our newly developed fine-wire thermometer system. Section 4 outlines a field experiment that we conducted in the evening of 15 September 2020 in the Colorado Front Range near Longmont, CO. First results of the field observations are presented in Section 5, and summary and conclusions are given in Section 6.

2. Theory

The Obukhov-Corrsin theory [3,7] is the classical theory of fully developed, locally homogeneous and isotropic turbulence of a passive scalar θ. Obukhov [3] found universal similarity relationships for the second-order structure function,

$$D_{\theta\theta}(\mathbf{r}) = \langle [\theta(\mathbf{x}+\mathbf{r}) - \theta(\mathbf{x})]^2 \rangle. \tag{1}$$

Independently of Obukhov's work, Corrsin [7] found the $-5/3$ power law for the wavenumber spectrum in the inertial-convective subrange and, by analogy with Heisenberg's [16] theory of fully developed turbulence in the velocity field, derived a -7 power law for the temperature spectrum in the viscous-diffusive range.

Obukhov predicted the existence of two different ranges for r: the inertial-convective subrange, where r is sufficiently large such that the molecular kinematic viscosity, ν, and the molecular diffusivity of heat, κ, have no effect on the spatial statistics of θ. This range is referred to as the inertial-convective subrange, within which $D_{\theta\theta}(\mathbf{r})$ must be a universal function of the separation $r = |\mathbf{r}|$, the scalar variance dissipation rate χ, and the dissipation rate ε of the turbulent kinetic energy. Obukhov used dimensional analysis to derive $D_{\theta\theta}(r)$ for the inertial-convective subrange:

$$D_{\theta\theta}(r) = \beta \varepsilon^{-1/3} \chi r^{2/3}, \tag{2}$$

where β is a universal, dimensionless constant known as the Obukhov constant, or Obukhov-Corrsin constant. It is often useful to restate Eq. (2) as

$$D_{\theta\theta}(r) = C_{\theta}^2 r^{2/3} \tag{3}$$

[1, p. 46, Eq. 3.18], where

$$C_{\theta}^2 = \beta \varepsilon^{-1/3} \chi \tag{4}$$

[1, p. 47, Eq. 3.19] is referred to as the temperature structure parameter.

At very small scales, $D_{\theta\theta}(r)$ is predicted to depend only on χ, α, and r, and direct analysis, based on the scalar transport equation, leads to [3, Eq. 19]

$$D_{\theta\theta}(r) = \frac{1}{6}\frac{\chi}{\kappa}r^2. \tag{5}$$

The value of r at which the viscous-diffusive and inertial-convective asymptotes intersect is referred to as the inner scale,

$$\ell_0 = (6\beta\kappa)^{3/4}\varepsilon^{-1/4}. \tag{6}$$

The inner scale plays an important role for modelling the transition of the 3D wavenumber spectrum, $\Phi_{\theta\theta}(\kappa)$, from the inertial-convective subrange into the viscous-diffusive range [1,17,18].

3. A new fine-wire thermometer system

Here we give a brief description of our newly developed fine-wire thermometer system.

Each platinum resistance temperature detector (PRTD) was constructed using Wollaston wire (manufactured by Sigmund Cohn Corp.), comprised of silver-clad 0.64 μm platinum fine wire. A short length of the wire was affixed to a pair of pins, spaced 0.1 inches, and etched using a dilute nitric acid solution to expose a short (less than 1 mm) length of fine platinum wire.

The recording system ultimately provides accurate samples of PRTD resistance, as it varies in time. A circuit was built to provide a small excitation current to the sensors through comparatively-large-valued excitation resistors, via a battery supply, and to provide a differential signal interface to the recorder for digitization. 4-wire and 2-wire resistance temperature detector topologies were explored, and accuracies are comparable for the wire lengths involved, where calibration accounts for losses due to cable resistance and recorder input load resistance. High-quality shielded twisted pair wire was used to connect each fine wire sensor to the excitation circuit, which was in turn connected to the microphone inputs of a commercial multi-channel digital audio recorder, Tascam DR-680 (with 24-bit quantization and various sampling rates starting at 44.1 kHz). Recorder sensitivity was determined by splitting a 1 kHz sine wave of known voltage amplitude across the input channels, and referencing that to the corresponding unitless data values of the recorded signal, for each channel, at the gain settings used in the experiments. This measured sensitivity is included in the calibration to convert voltage samples to the corresponding PRTD resistance values.

4. Field measurements

In the evening of 15 September 2020, we collected temperature measurements by means of an array of three fine-wire sensors (labeled FW5, FW7, and FW8), which we attached to a microphone stand. The stand was mounted in a car and extended through the sunroof 1.0 m above the roof line, angled forward somewhat, while the sensor mounting was adjusted to be horizontal, with sensors FW7 and FW8 spaced 5 cm above and below the mount, respectively, in front, facing into the wind. Sensor

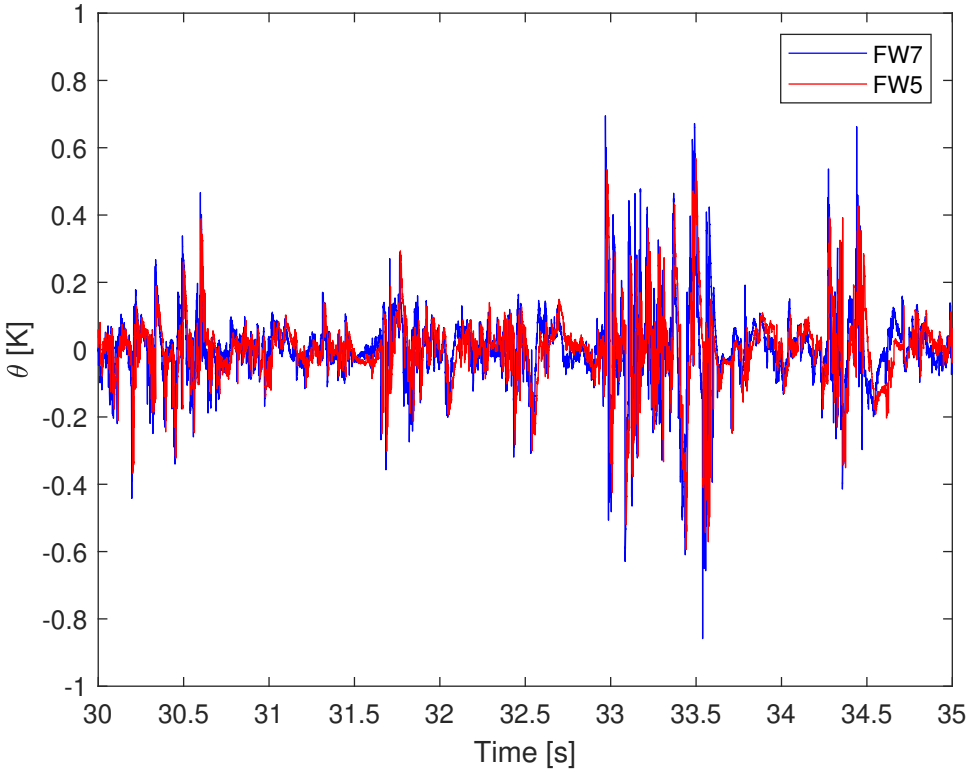

Figure 1. *A 5-s-long segment of the temperature signals measured with the fine-wire sensors FW7 (blue) and FW5 (red) during Run 411. The measurements were made out of a car travelling at 40* mph *(18* $\mathrm{m\,s^{-1}}$*), such that 5 s correspond to a path length 90* m.

FW5 was placed at the same height as FW7, 10 cm directly behind FW7. The car's roof line was 1.5 m above the ground, such that the sensors were approximately 2.5 m above ground level (AGL).

Recording began at 2238 MDT (Mountain Daylight Time) and lasted less than 1 h. We divided the data into 13 "runs", referred to Run 408 through Run 420. In this paper, we present and analyze data only from Run 411. Run 411 began at 2247 MDT and lasted 3 min 12 s. During Run 411, the car was travelling southward on North 75th Street between Hygiene, CO and Niwot, CO. During the first minute of Run 411, the car travelled at a nominal speed of 40 mph (17.9 $\mathrm{m\,s^{-1}}$), and later it was accelerated to 45 mph (20.1 $\mathrm{m\,s^{-1}}$).

5. Results

5.1. Time series of temperature fluctuations

Fig. 1 shows, as a representative example, 5-s long temperature signals measured with sensors FW5 and FW7. At a speed of 18 $\mathrm{m\,s^{-1}}$, a 5-s interval corresponds to a path length of 90 m. The two signals track each other well, as expected. Closer inspection shows that the FW5 signal slightly lags behind the FW7 signal.

The delay of the FW5 signal with respect to the FW7 signal can be seen in Fig. 2, which depicts a 0.2-s long subsection of Fig. 1. The time interval of 0.2 s corresponds to a path length of 3.6 m. If the true air speed (the speed of the air relative to the

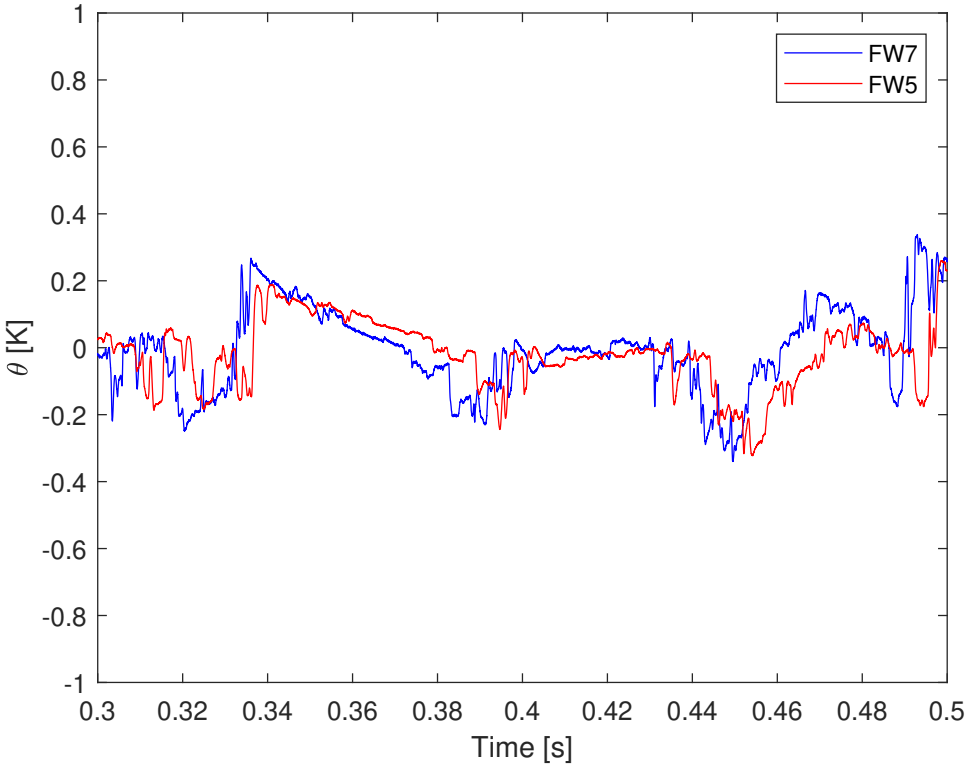

Figure 2. *A 0.2-s long segment of the signals shown in Fig. 1, corresponding to a path segment of 3.6 m. It can be clearly seen that the FW5 signal lags the FW7 signal by about 5 ms, consistent with the 10-cm spacing between the two sensors.*

sensors) were 18 $\mathrm{m\,s^{-1}}$, that is, if the wind speed relative to the ground were small compared to the speed of the car, then one would expect a delay of $0.1\,\mathrm{m}/(18\,\mathrm{m\,s^{-1}})$ = 5.6 ms, which is in qualitative agreement with the delay that can be seen in Fig. 2.

Fig. 3 shows the cross-covariance function,

$$B_{12}(\tau) = \langle \theta_1(t+\tau)\theta_2(t) \rangle, \tag{7}$$

estimated from the two 5-s long time series measured with FW5 and FW7, respectively. The maximum of $B_{12}(\tau)$ is at $\tau_m = 5.3$ ms, which for the sensor spacing $d = 10$ cm gives a true air speed

$$V = \frac{d}{\tau_m} \tag{8}$$

of 18.8 $\mathrm{m\,s^{-1}}$, or 42 mph. That is, the wind speed relative to the ground was small compared to the nominal speed of the car. (We did not measure the wind speed relative to the ground directly.)

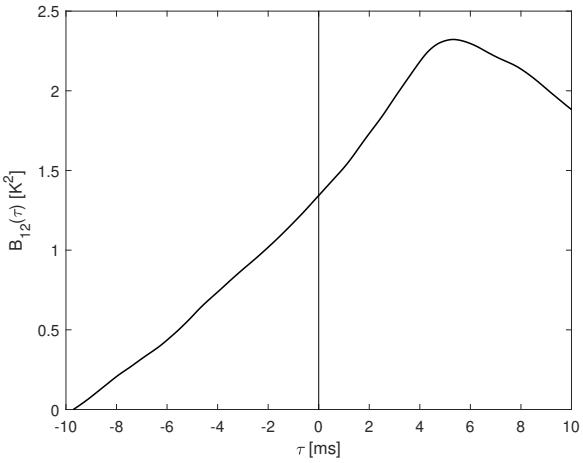

Figure 3. *Cross-covariance function $B_{12}(\tau)$ estimated from the 5-s-long FW5 and FW7 signals shown in Fig. 1.* The peak of $B_{12}(\tau)$ occurs at $\tau = 5.3$ ms, corresponding to a true air speed of 18.8 m s^{-1}.

5.2. Temperature structure function

Fig. 4 shows the structure function $D_{\theta\theta}(r)$ estimated from the 5-s long FW7 signal in Fig. 1. The separation r was obtained from

$$r = V\tau, \tag{9}$$

where τ is the time lag and V is the true air speed obtained from Eq. (8).

Fig. 4 demonstrates that the observed $D_{\theta\theta}(r)$ follows an r^2 law for small r and an $r^{2/3}$ law for intermediate r, as predicted in Eqs. (5) and (3) for the viscous-diffusive subrange and inertial-convective subrange, respectively. Using Eq. (3), we can calculate C_θ^2 from the $r^{2/3}$ asymptote and find $C_\theta^2 = 0.058\,\mathrm{K}^2\,\mathrm{m}^{-2/3}$. The inner scale ℓ_0 is the value of r at which the two asymptotes intersect, and we find $\ell_0 = 8.6$ mm.

Moreover, Fig. 4 shows that for r comparable to and larger than about 1 m, $D_{\theta\theta}(r)$ becomes flat. This is due to the fact that the recording system has a built-in high-pass filter with a cut-off frequency of order 10 Hz, which corresponds to a temporal lag τ of order 0.1 s and a spatial separation $r = V\tau$ of order 2 m. In addition to, and independently of, the high-pass filter effect, a flattening of $D_{\theta\theta}(r)$ occurs also due to the fact that in the lower part of the atmospheric surface layer, the outer scale of turbulence is comparable to the measurement height above ground level, which in our case is 2.5 m. In the current study, we make no attempt to disentangle the two effects from each other.

5.3. Time series of true air speed, temperature structure parameter, inner scale, and power-law exponent

The analysis that we have shown above exemplarily for a single 5-s long interval we have performed for each 5-s interval within the 192-s long dataset collected during Run 411. Fig. 5 shows the time series of the true air speed, V, which varies between 17 m s^{-1} and 21.5 m s^{-1}. Our records indicate that the nominal driving speed was 40 mph (17.9 m s^{-1}) during the first minute of Run 411, and later the car was accelerated to 45 mph (20.1 m s^{-1}). The retrieved V values fluctuate around the nominal car

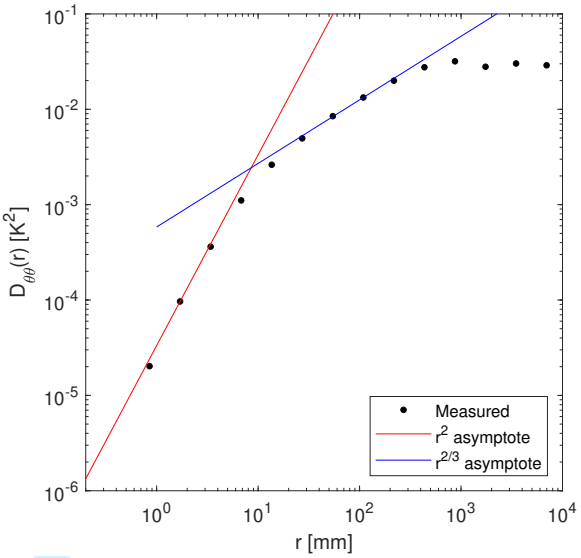

Figure 4. *Temperature structure function $D_{\theta\theta}(r)$ estimated from the 5-s long FW7 time series shown in Fig. 1. The measured structure function follows an r^2 power for small r and an $r^{2/3}$ power law at intermediate scales, as theoretically predicted by the Obukhov-Corrsin theory; see Eqs. (5) and (2), respectively.*

speed by 2 m s^{-1} at most. Due to a lack of more accurate data of the car's speed, it is impossible to ascertain to what extent these fluctuations represent car-speed fluctuations, wind-speed fluctuations, or a combination of both. The magnitude of the fluctuations, however, is consistent with the wind speed of 2 m s^{-1} reported for 2248 MDT by the Boulder Municipal Airport.

We used the V estimates shown in Fig. 5 to estimate C_θ^2 and l_0 for each of these 5-s intervals, as shown in Fig. 6. C_θ^2 varies between 0.011 K^2 m$^{-2/3}$ and 0.087 K^2 m$^{-2/3}$, and l_0 varies between 5 mm and 13 mm. Closer inspection reveals that C_θ^2 and l_0 are practically uncorrelated.

Of particular interest is the question about the robustness of the $r^{2/3}$ power law predicted for the inertial-convective range. In Fig. 4 we have seen that the observed $D_{\theta\theta}(r)$ follows the $r^{2/3}$ power law most closely for r comparable to 10 cm, which is large compared to l_0 and small compared to $h = 2.5$ m, the height above ground level. In fact, 10 cm is comparable to $\sqrt{l_0 h}$, the geometrical mean of l_0 and h. If we take 10 mm as the typical value of l_0, then $\sqrt{l_0 h} = 16$ cm.

We analyzed $D_{\theta\theta}(r)$ for a set of r values that varied by a factor of 2, that is, $r = 2^n V T_s$, where $n = 0...15$ and $T_s = 1/44{,}100$ s $= 23$ μs is the sampling period of our recording system. In order to estimate the power-law exponent α, we chose the pair of lags $\tau_1 = 128\ T_s$ and $\tau_2 = 256\ T_s$, which corresponds to the pair of separations $r_1 = 128\, V T_s$ and $r_2 = 256\, V T_s$. For $V = 18$ m s^{-1}, this gives $r_1 = 5.2$ cm and $r_2 = 10.4$ cm. Assuming a power law, $D_{\theta\theta}(r) \propto r^\alpha$, we have

$$\frac{D_{\theta\theta}(r_2)}{D_{\theta\theta}(r_1)} = 2^\alpha, \tag{10}$$

such that

$$\alpha = \frac{\ln[D_{\theta\theta}(r_2)/D_{\theta\theta}(r_1)]}{\ln 2}. \tag{11}$$

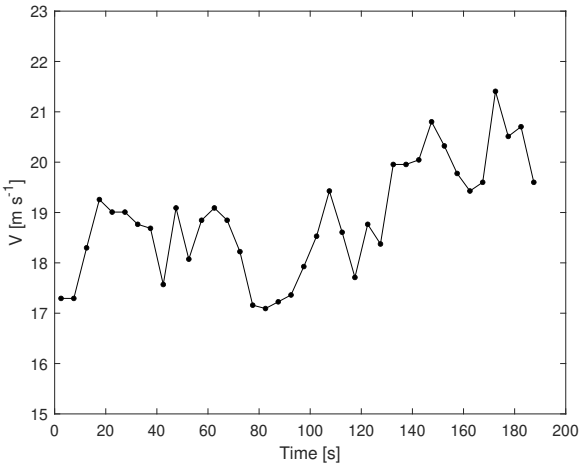

Figure 5. *True air speed V determined for each 5-s interval for the entire 192-s long Run 411.*

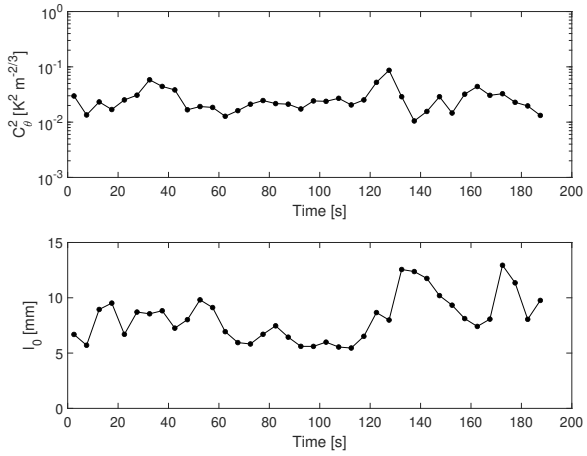

Figure 6. *Temperature structure parameter C_θ^2 (upper panel) and inner scale ℓ_0 (lower panel) determined for each 5-s interval for the entire 192-s long Run 411.*

Fig. 7 shows the estimates of the power-law exponent α for each of the 5-s intervals during Run 411. The 38 α estimates have a mean value of 0.63, which is slightly smaller than the theoretically predicted value $2/3 \approx 0.67$. The standard deviation of the α estimates is 0.06, such that $2/3$ lies well within the interval 0.63 ± 0.06.

5.4. Refractive-index structure parameter

If humidity effects are negligible, which is the case here (the relative humidity reported for 2248 MDT by the Boulder Municipal Airport was only 18%), the optical refractive index n of air is a function of the wavelength λ, the (absolute) temperature $T + \theta$ and the pressure p,

$$n = 1 + a\left(1 + \frac{b}{\lambda^2}\right)\frac{p}{T+\theta}, \tag{12}$$

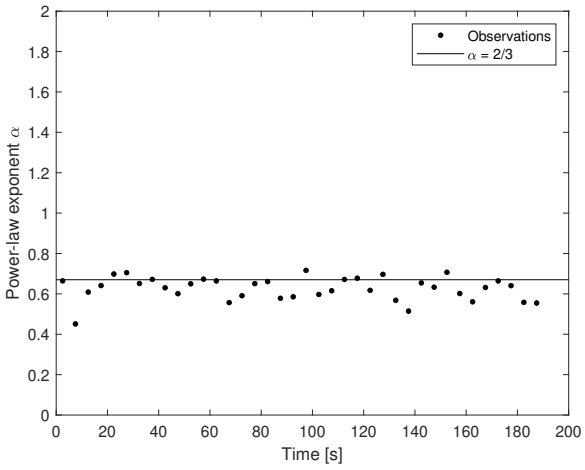

Figure 7. *Power-law exponent in the inertial-convective range determined for each 5-s interval for the entire 192-s long Run 411.*

where T is the (absolute) mean temperature, θ is the turbulent temperature fluctuation, and $a = 7.76 \times 10^{-7}\,\mathrm{K\,Pa^{-1}}$ and $b = 7.52 \times 10^{-15}\,\mathrm{m^2}$ are constants [19, p. 10]. Turbulent pressure fluctuations are negligible if the Mach number is low, which is the case here, and we obtain the following relationship between the refractive-index structure parameter, C_n^2, and the temperature structure parameter, C_θ^2:

$$C_n^2 = a^2 \left(1 + \frac{b}{\lambda^2}\right)^2 \frac{p^2}{T^4} C_\theta^2. \tag{13}$$

We did not measure T and p as part of our fine-wire experiment, but we can use the observations reported by the Boulder Municipal Airport for 2248 MDT on 15 Sep 2020 ($T = 293$ K, $p = 842$ hPa) in order to estimate the constant of proportionality between C_n^2 and C_θ^2 as stated in Eq. (13). For $\lambda = 500$ nm (green light), we obtain $C_n^2/C_\theta^2 = 6.2 \times 10^{-13}\,\mathrm{K^{-2}}$. That is, $C_n^2 = 6.2 \times 10^{-13}\,\mathrm{m^{-2/3}}$ if $C_\theta^2 = 1\,\mathrm{K^2\,m^{-2/3}}$.

Fig. 8 shows the C_n^2 time series computed from the C_θ^2 time series shown in Fig. 6. The C_n^2 values range from $6 \times 10^{-15}\,\mathrm{m^{-2/3}}$ to $5 \times 10^{-14}\,\mathrm{m^{-2/3}}$, and the median of C_n^2 is $1.4 \times 10^{-14}\,\mathrm{m^{-2/3}}$. Nighttime C_n^2 values of order $1 \times 10^{-14}\,\mathrm{m^{-2/3}}$ in the atmospheric surface layer over land are consistent with earlier reports [20,21].

5.5. Temperature spectrum

Fig. 9 shows the one-sided frequency power spectrum $S_{\theta\theta}(f)$ estimated from the entire 192-s long temperature time series recorded during Run 411. We estimated the spectrum by means of Welch's method [22] of the "modified periodogram". We used an overlap of 50% between subsequent "Welch segments" and applied a Blackman window to each segment. The length of each Welch segment was 1 s, which gives $192 \times 2 - 1 = 383$ Welch segments, each of which was spectrally analyzed prior to incoherent averaging. Subsequently, we applied frequency-domain averaging to the averaged modified periodogram, such that the final spectrum contains 30 spectral estimates per decade in the frequency range from 22.05 Hz to the Nyquist frequency of 22.05 kHz.

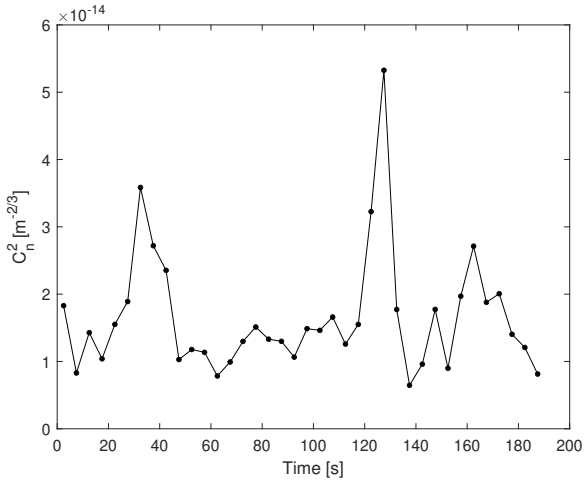

Figure 8. *Time series of C_n^2, computed from the C_θ^2 time series shown in Fig. 6.*

The spectrum follows the theoretically predicted $f^{-5/3}$ law at frequencies between about 10 Hz and several hundred Hz. We estimated the spectral level of the $f^{-5/3}$ asymptote, shown as the black line in Fig. 9, from the observed $S_{\theta\theta}(f)$ in the interval from 20 Hz to 100 Hz. The observed spectral density slightly exceeds the $f^{-5/3}$ asymptote in the frequency range from 100 Hz to 600 Hz. This phenomenon is known as the "Hill bump" [23,24]. Above 600 Hz, the observed $S_{\theta\theta}(f)$ drops rapidly, marking the transition into the viscous-diffusive range.

At very low and very high frequencies, the observed spectrum shows artifacts. The roll-off of $S_{\theta\theta}(f)$ to below the $f^{-5/3}$ asymptote at frequencies below about 10 Hz is caused by the recording system's built-in high-pass filter. The flattening of the spectrum above about 4 kHz indicates noise. The noise spectral density is about $1 \times 10^{-10}\,\mathrm{K^2Hz^{-1}}$. If we consider 10 kHz as the useful bandwidth for turbulence measurements, $1 \times 10^{-10}\,\mathrm{K^2Hz^{-1}}$ corresponds to a noise r.m.s. value of 1 mK.

5.6. Collocated fine-wire and sonic measurements

The calibration of fine-wire thermometers relies on assumptions about the relationship between the fluctuation of the wire resistance, which is the primary measureable, and the air-temperature fluctuation θ, which is the observable that we are interested in. The centerpiece of this relationship is an empirical model for the heat transfer between a heated cylindrical body (the electrically heated fine wire in our case) immersed in the cross-flow of a fluid (in our case the ambient air). We have reviewed the classical literature [12,25–30] and have developed a calibration procedure based on Churchill and Bernstein's model [30, p. 302] for the Nusselt number, Nu, as a function of the molecular Prandtl number, Pr, and the Reynolds number:

$$\mathrm{Nu} = 0.3 + 0.62 \frac{\mathrm{Pr}^{1/3}}{[1 + (0.4/\mathrm{Pr})^{2/3}]^{1/4}} \mathrm{Re}^{1/2}. \qquad (14)$$

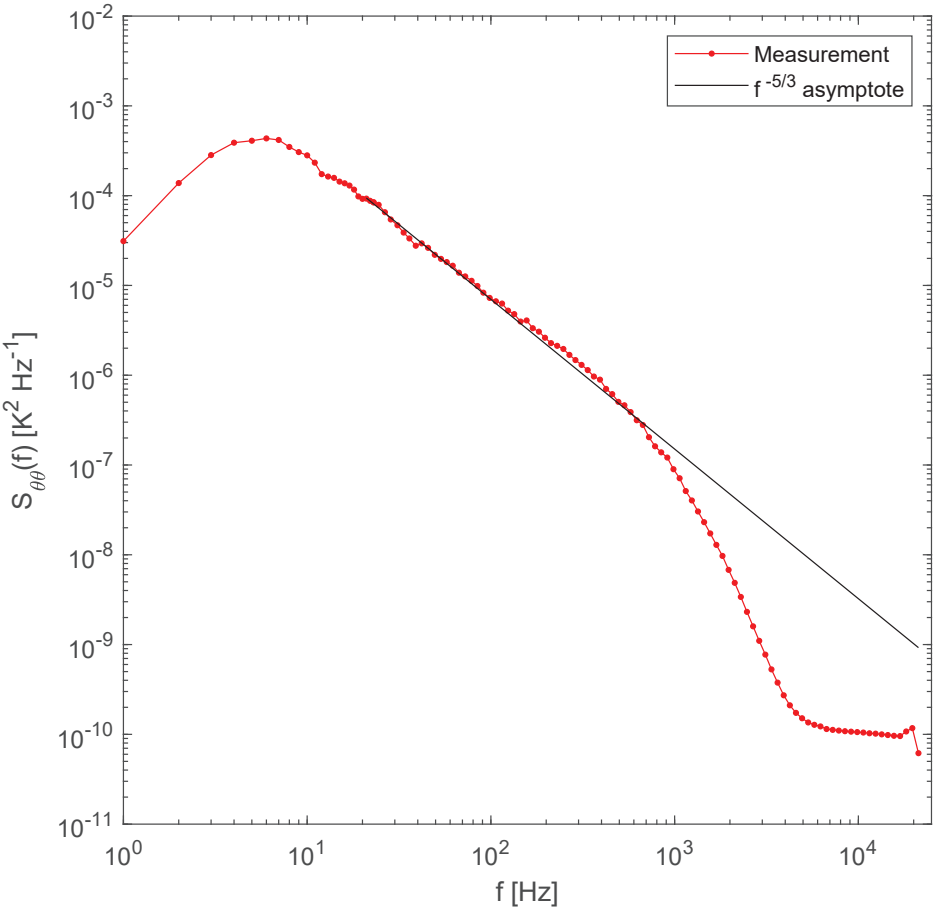

Figure 9. *Temperature spectrum estimated from the entire FW7 temperature signal recorded during the 192-s long Run 411.*

For air, Pr can be treated as a constant, which leads to

$$\mathrm{Nu} = A + B\,\mathrm{Re}^{1/2}, \tag{15}$$

a relationship known as "King's law". A more detailed account of our calibration procedure will be given elsewhere.

As an empirical test of the integrity of our calibration procedure, we measured turbulent air-temperature fluctuations in the atmospheric surface layer with our fine-wire thermometer system and with a collocated ultrasonic anemometer-thermometer ("sonic"). The experiment was conducted on 5 Oct 2021 in a residential area in the Rocky Mountain foothills several miles west of Boulder, CO. The sonic (Model 81000, manufactured by R. M. Young Company, of Traverse City, MI) was mounted on a portable tower at 1.6 m AGL, and the fine-wire was attached to a microphone stand at the same height.

Fig. 10 shows the temperature spectra estimated from the temperature fluctuations measured with fine-wire sensor FW8 and the sonic, respectively, during the 10-min period beginning at 1136 MDT. The mean wind speed was $U = 1.2\,\mathrm{m\,s^{-1}}$ during this 10-min period. In the inertial-convective subrange, the observed spectra follow the

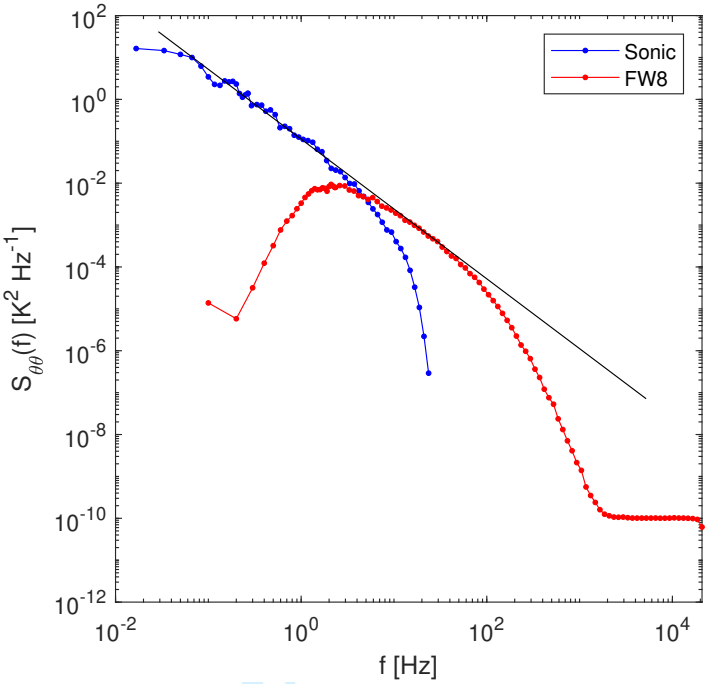

Figure 10. *Temperature spectra estimated from 10-min long temperature time series simultaneously measured with two collocated sensors: an ultrasonic anemometer-thermometer (blue) and a fine-wire thermometer (red). The black line indicates an $f^{-5/3}$ power law.*

same $f^{-5/3}$ power law, except where the fine-wire measurements are affected by the built-in highpass filter (at frequencies below about 10 Hz) and the sonic measurements are affected by lowpass filtering caused by the finite size of the sonic's observation volume. The sonic spectrum begins to drop significantly between the $f^{-5/3}$ asymptote at a frequency of a few hertz, which for $U = 1.2\,\mathrm{m\,s^{-1}}$ corresponds to a length scale $l = U/f$ of a few decimeters. The roll-off of the fine-wire spectrum from the inertial-convective range into the viscous-diffusive range occurs at about 100 Hz, indicating an inner scale ℓ_0 of order 1 cm.

6. Summary and conclusions

We have shown that our fine-wire thermometer system is capable of collecting high-quality measurements of turbulent temperature fluctuations in the open atmosphere. Even though the 0.64-μm-diameter platinum fine wires are extremely delicate, our three sensors did not break when exposed to a true air speed of about 20 $\mathrm{m\,s^{-1}}$ over the course of several tens of minutes.

The active length of the wires is less than 1 mm, which is small compared to 5 mm, the smallest value of the inner scale ℓ_0 observed during Run 411. Therefore, the measured temperature fluctuations are not affected by spatial filtering due to the finite size of the sensors. The wires' response time is so short that temporal filtering plays no role either. The noise level of the entire system is so low that the spectrum can be measured well into the viscous-diffusive range.

We have shown that the delay between signals measured with a pair of longitudinally spaced sensors (we used a spacing of 10 cm) can be used for reliably measuring the true air speed (the speed of the air relative to the sensor) if the platform moves fast compared to the wind speed relative to the ground.

The temperature structure function $D_{\theta\theta}(r)$ and the frequency spectrum $S_{\theta\theta}(f)$ estimated from the measured temperature fluctuations are consistent with the predictions of the classical Obukhov-Corrsin theory. We determined the power-law exponent α of $D_{\theta\theta}(r)$ from observed values of the ratio $D_{\theta\theta}(r_2)/D_{\theta\theta}(r_1)$, where we chose $r_1 = 5$ cm and $r_2 = 10$ cm, and we found $\alpha = 0.63 \pm 0.06$, which is consistent with the theoretically predicted value $2/3 \approx 0.67$.

In the future, we intend to deploy our fine-wire sensing system on portable meteorological towers as well as on moving platforms such as cars, boats, balloons, and unmanned arial systems (UAVs). Arrays of fine-wire thermometers continue to be valuable tools for in-depth investigations of various aspects of optical turbulence, including intermittency [31], anisotropy and temperature "sheets" [32–34], and the possible relevance of turbulent phase screens with non-Gaussian increments [35].

References

[1] Tatarskii VI. Wave propagation in a turbulent medium. New York: McGraw-Hill; 1961.
[2] Tatarskii VI. The effects of the turbulent atmosphere on wave propagation. Jerusalem, Israel: Israel Program for Scientific Translation; 1971.
[3] Obukhov AM. The structure of the temperature field in a turbulent flow. Izv Akad Nauk SSSR, Ser Geogr i Geofiz. 1949;13:58–69.
[4] Yaglom AM. Introduction to the theory of stationary random functions. Uspekhi Mat Nauk. 1952;7:3–168.
[5] Yaglom AM. An introduction to the theory of stationary random functions. Englewood Cliffs, New Jersey: Prentice-Hall; 1962.
[6] Monin AS, Yaglom AM. Statistical fluid mechanics — Volume 2. Cambridge, Massachusetts: The MIT Press; 1975.
[7] Corrsin S. On the spectrum of isotropic temperature fluctuations in an isotropic turbulence. J Appl Phys. 1951;22:469–473.
[8] Monin AS, Yaglom AM. Statistical fluid mechanics — Volume 1. Cambridge, Massachusetts: The MIT Press; 1971.
[9] Haugen DA, editor. Workshop on micrometeorology. Boston: American Meteorological Society; 1973.
[10] Frisch U. Turbulence: the legacy of A. N Kolmogorov. Cambridge: Cambridge University Press; 1995.
[11] Kaimal JC, Finnegan JJ. Atmospheric boundary layer flows: Their structure and measurement. Oxford, United Kingdom: Oxford University Press; 1994.
[12] Bruun HH. Hot-wire anemometry. Oxford, United Kingdom: Oxford University Press; 1995.
[13] Foken T. Micrometeorology. 2nd ed. Berlin, Germany: Springer; 2017.
[14] Pope SB. Turbulent flows. Cambridge, United Kingdom: Cambridge University Press; 2000.
[15] Sagaut P. Large eddy simulation for incompressible flow. 3rd ed. Berlin, Germany: Springer-Verlag; 2006.
[16] Heisenberg W. Zur statistischen Theorie der Turbulenz. Z Phys. 1948;124:628–657.
[17] Hill RJ, Clifford SF. Modified spectrum of atmospheric temperature fluctuations and its application to optical propagation. J Opt Soc Am. 1978;68:892–899.
[18] Muschinski A. Temperature variance dissipation equation and its relevance for optical

turbulence modeling. J Opt Soc Am A. 2015;32:2195–2200.
[19] Clifford SF. The classical theory of wave propagation in a turbulent medium. In: Strohbehn JW, editor. Laser beam propagation in the atmosphere. Berlin: Springer; 1978. p. 9–43.
[20] Lawrence RS, Ochs GR, Clifford SF. Measurements of atmospheric turbulence relevant to optical propagation. J Opt Soc Am. 1970;60:826–830.
[21] Weseley ML, Alcaraz EC. Diurnal cycles of the refractive index structure coefficients. J Geophys Res. 1973;78:6224–6232.
[22] Welch PD. The use of Fast Fourier Transform for the estimation of power spectra: A method based on time averaging over short modified periodograms. IEEE Trans Audio and Electroacoustics. 1967;AU-15:70–73.
[23] Hill RJ. Models of the scalar spectrum for turbulent advection. J Fluid Mech. 1978; 88:541–562.
[24] Muschinski A, de Bruyn Kops SM. Investigation of Hill's optical turbulence model by means of direct numerical simulation. J Opt Soc Am A. 2015;32:2423–2430.
[25] King LV. On the convection of heat from small cylinders in a stream of fluid: Determination of the convection constants of small platinum wires with applications to hot-wire anemometry. Phil Trans Roy Soc Lond A. 1914;214:373–432.
[26] Nusselt W. Das Grundgesetz des Wärmeüberganges. Gesundheits-Ing. 1915;38:477–482, 490–496.
[27] Collis DC, Williams MJ. Two-dimensional convection from heated wires at low Reynolds numbers. J Fluid Mech. 1959;6:357–384.
[28] Wyngaard JC. The effect of velocity sensitivity on temperature derivative statistics in isotropic turbulence. J Fluid Mech. 1971;48:763–769.
[29] Williams RM, Paulson CA. Microscale temperature and velocity spectra in the atmospheric boundary layer. J Fluid Mech. 1977;83:547–567.
[30] Churchill SW, Bernstein M. A correlating equation for forced convection from gases and liquids to a circular cylinder in crossflow. J Heat Transfer. 1977;99:300–306.
[31] Muschinski A, Frehlich RG, Balsley BB. Small-scale and large-scale intermittency in the nocturnal boundary layer and the residual layer. J Fluid Mech. 2004;515:319–351.
[32] Muschinski A, Wode C. First in situ evidence for coexisting submeter temperature and humidity sheets in the lower free troposphere. J Atmos Sci. 1998;55:2893–2906.
[33] Balsley BB, Jensen ML, Frehlich RG, et al. Extreme gradients in the nocturnal boundary layer: structure, evolution, and potential causes. J Atmos Sci. 2003;60:2496–2508.
[34] Muschinski A. Optical propagation through non-overturning, undulating temperature sheets in the atmosphere. J Opt Soc Am A. 2016;33:793–800.
[35] Muschinski A. Phase-factor spectra of turbulent phase screens. J Opt Soc Am A. 2021; 38:1339–1348.